Residual Stress Measurement in Railroad Car Wheels

by

Jinmyun Jo

Dissertation submitted to the Faculty of the

Virginia Polytechnic Institute and State University

in partial fulfillment of the requirements for the degree of

Doctor of Philosophy

in

Materials Engineering Science

APPROVED:

Robert W. Hendricks, Chairman

Norman E. Dowling

Diana Farkas

Thangavelu Kuppusamy

Robert E. Swanson

September 1989

Blacksburg, Virginia

Residual Stress Measurement in Railroad Car Wheels

by

Jinmyun Jo

Robert W. Hendricks, Chairman

Materials Engineering Science

(ABSTRACT)

A new failure criterion for discriminating good and bad (overheated) railroad car wheels is proposed. This criterion can replace the conventional "four inch" discoloration rule. The procedure for the new discrimination criterion is based on the fluctuations of the azimuthal residual stress in the tread of the wheel. This criterion is based on a maximum likelihood statistical analysis of data obtained from six different wheels as determined by x-ray diffraction. Of these locations, the analysis showed the tread, and perhaps a critical point on the top of the flange, to be the most sensitive to residual stress. The variance analysis showed that fluctuations in stress at the most sensitive location in the tread appeared to be related to the service history. The residual stresses showed an oscillatory pattern in the hoop direction around the wheels.

Extension of the measurement technology to the use of magnetoelastic stress measurement is proposed. To evaluate the inaccuracy in stress data possible from a large sample with curved surface, corrections for a deliberate tilt of the plane of the x-ray diffractometer from the normal to the sample surface have been developed. Analysis of different misalignments are discussed. To validate our x-ray residual stress data, residual stresses were also measured by hole drilling. Excellent agreement between two techniques was found. Finally, stress variation with depth below surface was determined by the hole drilling technique.

Acknowledgements

The author would like to acknowledge the understanding, support, and guidance of his major professor, Professor Robert W. Hendricks during the course of this research. Thanks are also extended to his committee, Professors Norman E. Dowling, Diana Farkas, Thangavelu Kuppusamy, and Robert E. Swanson, for their guidance and helpful comments during the course of this research. Finally, this work would have never been completed without the encouragement of the author's wife, Oksik Jo and that of his family.

The author would also like to express his gratitude for financial assistance from the Departments of Materials Engineering (Prof. C. W. Spencer) and Engineering Science and Mechanics (Prof. D. Frederick), and the Materials Engineering Science Program (Prof. K. Riefsneider), at Virginia Polytechnic Institute and State University. I am also indebted to the CSX Transportation Co. and the Institute for Materials Science and Engineering of the Center for Innovative Technology for their financial and technical support.

I would also like to thank the following: Prof. V. Foutz and Dr. F. Koon of the Statistics Department for suggesting the likelihood ratio tests for the analysis of the data and for their assistance in interpreting the results; Dr. R. Benecke of Caterpillar Tractor Company for providing the formulas for the rust removal solutions used in the wheel work; of the

Norfolk Southern Corp. for providing the technical information concerning metallurgical microstructures of railroad wheel steels.

The successful completion of a Ph.D. dissertation involves many people who provided expertise and/or encouragement in many areas. I especially wish to acknowledge the technical help of Prof. W. Reynolds in evaluation of micrographs; Mr. W. Halley, Dr. M. Laurant, and Ms. K. Rohr for editorial help and academic discussion in preparing this dissertation; Marc Tricard for sincere experiment help; , , , ,

, , , , , , ,

, , , , and , for various help of this work.

I especially wish to thank , , , ,

, , , , , , ,

, , , , ,

, , , , ,

, , , , ,

, and all who have made a significant contribution for which I am deeply grateful.

I sincerely thank my former professors, at University of Nevada-Reno, Deans and and Professor at Dankook University, and Professor at Kyungbook University, who have encouraged me during my graduate study.

Table of Contents

List of Illustrations

List of Tables

1.0 EXECUTIVE SUMMARY

Train derailments result in large financial losses to the railroad industry and sometimes even involve loss of human life. One of the major causes of train derailments is wheel failure. In order to reduce the probability of an accident due to wheel failure, the industry uses the "four inch" discoloration rule to remove suspected wheels. However, it is widely believed that the "four inch" rule does not perform satisfactorily in discriminating between good and bad wheels. One estimate suggests that eighty percent of the removed wheels, especially those of the new curved plate design, are in fact good wheels. This results in an estimated $80 million annual loss.

The causes of the wheel failure have been investigated by many scientists in order to find a technique with better discrimination than the "four inch" rule. Previous research has shown that wheels fail by fracture. The initiation and propagation of cracks has been shown to be related to residual stresses which are believed to be caused by thermal braking cycles. Thus, determination of residual stresses in railroad car wheels has been a significant research topic for many years.

The residual stresses in wheels have been studied using Barkhausen noise, saw cutting, hole drilling, and other analyses. However, x-ray diffraction, one of the major tools for the investigation of residual stress, has not been attempted previously for residual stress measurements in uncut railroad wheels because until recently it was slow, not portable, and thus inappropriate for use in the field, on large samples such as a railroad wheel.

The purpose of this research was to use high speed, portable x-ray residual stress technology to characterize railroad wheels subjected to different histories, to use statistical analyses to find the critical locations on the wheels where measurements should be made which maximize the discrimination between good and bad wheels, and to evaluate whether a nondestructive technique utilizing x-ray residual stress analysis or some other calibrated nondestructive evaluation method has potential for use in place of the current "four inch" rule.

Six wheels (two new, two normal wear, and two heat-discolored wheels) were through characterized by x-ray diffraction to construct the data base for the statistical analysis. Each normal wear wheel had been used to some extent, but had no grooves on the tread and no discoloration on the plate. Each heat-discolored wheel had approximately four inches of discoloration on the plate and grooves on the tread.

For the x-ray stress measurements, a wheel carrier was constructed to allow convenient and safe experiments. The x-ray residual stresses were determined by measuring the change of the lattice spacing as a function of the orientation of the grains in the metal. The strain was then calculated from the lattice spacing change, and Hooke's law was used to determine the stress from the strain. In all, residual stresses were determined at over one thousand locations on the wheels. Rust in certain regions of the wheel resulted in a poor signal to noise ratio so that accurate diffraction peak positions were difficult to resolve. In order to improve the quality of x-ray diffraction, a cleaning solution was used. A large tilt of the diffractometer in a plane perpendicular to the plane of the diffraction was needed because of the complicated geometry of the wheels. An equation was derived to correct for this tilt. In addition, the effects of the misalignment errors on the x-ray stress measurements were considered.

In an auxiliary experiment, hole drilling was used to measure the depth profile of residual stresses and to provide a comparison with the x-ray results. A special fixture was designed to adapt and align the hole drilling device to the wheel. The agreement of the residual stresses determined by the x-ray diffraction and hole drilling was excellent.

Since the technology is to be applied in an industrial setting, the stress which characterizes an overheated wheel must be measured as rapidly and inexpensively as possible. Therefore, it was

essential to measure the state of stress at many locations on a wheel in order to determine if certain locations showed more sensitivity to changes in residual stress with service history. Stress measurements were made at a large number of locations over the entire face of each wheel. Maximum likelihood statistics test were used to select the most sensitive location which would characterize the wheel. It was found, surprisingly, that it was not the mean stress at the key (most sensitive) locations that characterized the service history. Rather, it is the fluctuation of the stresses around the wheel which seems to be the discrimination factor. Thus, the mean RMS fluctuation of the residual stress measured in the key location on the tread is proposed as a potential indicator for the discrimination of good versus bad wheels. Magnetoelastic measurements are proposed a possible high speed implementation of this observation.

In the following chapters, the history of residual stress measurements in railroad wheels is discussed as well as other relevant work in the area of wheel failure. Then a brief review of the general principles of residual stress measurement by x-ray diffraction and hole drilling is presented. Chapter 4 describes the experimental results of over 1000 stress measurements on the six wheels and the correlation of these data with the hole drilling data. In Chapter 5, maximum likelihood analysis is applied to these data to determine the locations on the wheels at which the residual stress is most sensitive to service history. An analysis of the fluctuation of the residual stress as a function of service history is also carried out. The key results of the statistical analyses and this interpretation are given in the discussion of Chapter 6. The essence of the dissertation is summarized in the conclusion and recommendation of Chapters 7 and 8. Appendix A describes diffractometer misalignment errors in x-ray residual stress measurenets.

2.0 HISTORICAL REVIEW OF RESIDUAL STRESSES, FRACTURE, AND FAILURE IN RAILROAD WHEELS

Safe operation and maintenance of wheels on railroad freight cars is a problem of major significance to the American and international railroad industry. Fracture of wheels or failure of axle bearings can, and unfortunately sometimes does, result in derailments with loss of human life and serious impact on the environment. More often, derailments are not so sensational but yet involve significant expense in terms of repairs to cars and roadbed and in loss of revenue due to delays and reroutings. As important, there is a negative public perception of the safety-consciousness of the industry.

Industry concern with this problem, in the absence of definitive analytical technology and knowledge of the physical metallurgy of the mechanisms of wheel fracture and failure, led to a consensus of expert thinking that many of these failures were probably correlated with wheel overheating due to drag braking. It was also estimated that the degree of wheel overheating might be related to the discoloration of the oxide on the wheel near the rim. As a result, the "four inch" criterion evolved, in which it was estimated that if the rust discoloration extended radially four

inches from the rim towards the axle, the wheel may have suffered potentially damaging overheating. Unfortunately, this ad hoc industry attempt to manage a difficult and serious problem in the absence of definitive engineering evidence was incorporated into the "four inch rule" by the Fedral Railroad Administration (FRA). Thus, what originally had been intended to be an industry guideline instead had become a Federal administrative law subject to enforcement and which carried severe penalties for failure to comply[1].

The cost of the four inch rule to the industry, currently estimated at over $100 million annually, is very high[2]. Experience now indicates that there is little or no correlation between wheel discoloration and potential for failure[2-5] especially with the newer design curved-plate wheels[6]. In fact, it is estimated that in excess of 80% of the wheels removed under the requirements of the four inch rule are, in fact, good wheels[2,4,5]. This implies a needless loss to the industry of over $80 million annually with no resulting improvement in the safety of the railroad system!

From the foregoing, it is apparent that it is of critical importance to the industry to: (i) develop technology that will unequivocally relate some physically measurable parameter of a wheel to its propensity for failure, (ii) assure that this technology can be applied in the field by the railroads within their existing wheel inspection procedures, and (iii) keep the cost of such inspections to an amortized value of under $7 per wheel[4].

For approximately the past decade there has been a major effort to understand the nature of railroad wheel failures, both from a theoretical and an experimental point of view. Under the sponsorship of the Association of American Railroads (AAR), significant progress has been made in developing finite element analysis computer codes which predict the heating of, and resultant residual stresses in, wheels subjected to a variety of braking conditions[7-12]. As these calculations have evolved, the elasto-plastic behavior of the wheels and various types of thermal loads have been included in the calculations. The temperature gradients predicted by the calculations, as well as other properties such as braking forces and coefficients of friction, have been examined experimentally[13,14] and these results have been incorporated into improved computational analyses. A representative result for a single wheel is shown in Figure 1. This result will be of importance in Section 4 when the X-ray residual stress results are discussed. A primary result of these calcu-

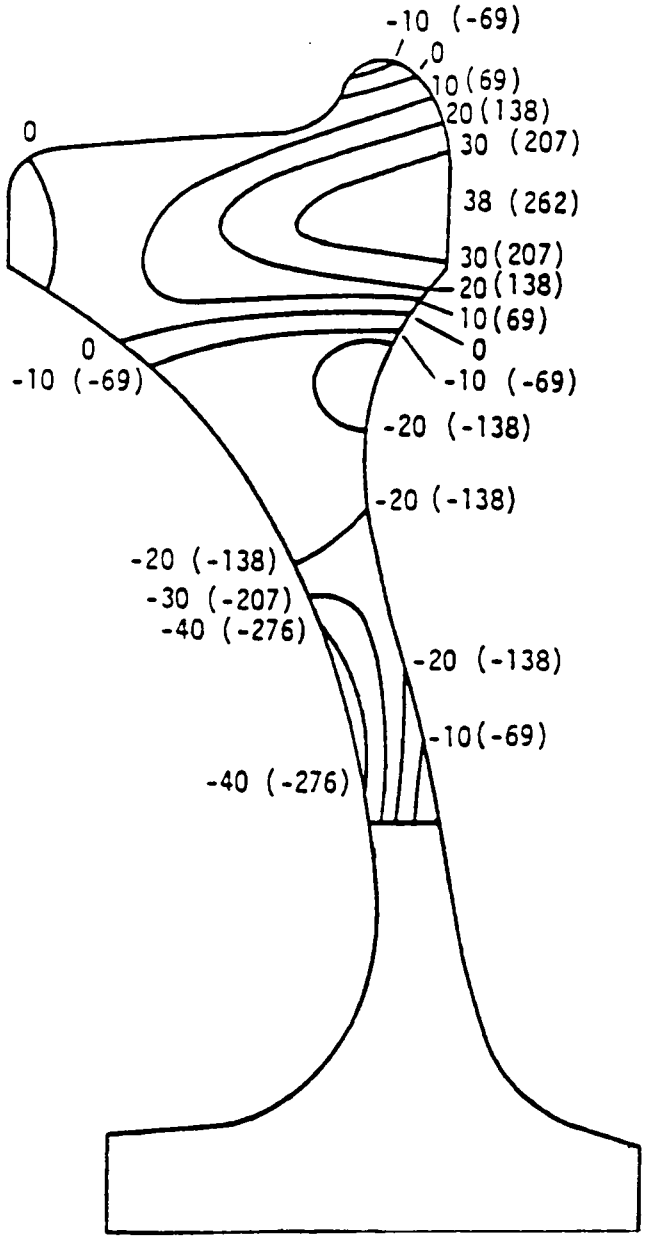

Figure 1. Calculated residual stress contours in a curved plate railroad wheel[11].

lations is that it has been shown that residual stresses developed during the heating / cooling cycle of extended braking are clearly large enough to create conditions under which crack growth and ultimate wheel failure would be expected to occur. This result also shows no steep stress variation in depth near the surface of wheel. It is to be noted that these calculations assume cylindrical symmetry. As will be seen later, this assumption may be questionable.

In recent experimental saw cutting work[15], it has been observed that in approximately 10% of the wheels studied there can be significant deviations of the residual stresses from azimuthal (cylindrical) symmetry about the wheel axle. This effect is attributed to hot zones which appear to be some 200°F hotter than the rest of wheel, and seem to extend over 90 to 120° angular range. The effect is often so severe that, even though the circumferential residual stresses outside this zone may be compressive, they can be tensile within the zone. It is important to note that this effect was discovered only after the present research was proposed and the experiments were begun.

In conjunction with these computational studies, there has been considerable effort expended to experimentally verify the state of residual stress predicted by the computational models. The topic has been the subject of a major Department of Transportation (DOT) conference[16], and include such technologies as saw cutting[17,18], Barkhausen noise analysis (BNA)[3,19], and hole drilling[20,21]. More recently, the AAR and National Aeronautics and Space Administration (NASA) - Langley have jointly developed technology based on the magneto-acoustic effect[22-27] . This instrument is currently under evaluation at the AAR and a recent conversation with Namkung indicates that much work remains to be done before the technique can be considered as a production tool for the characterization of stresses in real-world samples[28]. Because, as will be discussed below, the metallurgy of steel rails and railcar wheels is expected to be quite similar, the review of residual stress measurement in rails by Cheesewright[29] should be of significance to the present work. It is important to note that, with the exception of notes in passing by Barton et al[3] and Cheesewright[29] residual stress measurement by x-ray diffraction has not been considered for application to the railroad wheel problem even though it is an old and well-established technique[30-33] . This is because, prior to the development of PARS[32] (Portable Apparatus for Residual Stress) by James and Cohen in 1976, it was not possible to make measurements on entire wheels without sectioning. It

has only been in the last four years that PARS has evolved from a university prototype into a viable commercial product that it has warranted consideration. It is to be noted that the Technology for Energy Corporation (TEC) Model 1600 X-Ray Stress Analysis System used on this research was developed by Professor Hendricks, while he was with TEC, applying the original James and Cohen patent.

Although the effect of microstructure on the mechanical behavior of railroad wheels has not been extensively studied, there have been fracture mechanics studies[34,35]. Furthermore, there have been several fundamental studies on rail steels, which are essentially the same alloys as those used in wheels. Thus, these rail studies should provide guidance in the present study. Pearlite interlamellar spacing has been shown to have the greatest effect on the fatigue crack initiation endurance limit[36] although it has only a minor effect on fatigue crack propagation[37]. Prior austenite grain size, pearlite colony size, and colony orientation also tend to control fatigue crack propagation[37], with roughness-induced crack closure being cited as a controlling mechanism[38]. These variables must be examined in any comprehensive study of fatigue crack control in railroad wheels.

At a meeting among CSX Transportation, AAR, VPI&SU, and CIT personnel held in March 1987, it was concluded that of all of these various residual stress measurement technologies, X-ray diffraction showed the greatest promise to give possibility for discriminating good and bad wheels because of its speed, accuracy, and small sampling size, and because it is the only NDE technique which can provide all components of the stress tensor required for a complete analysis of the complex state of stress in railroad wheels. However, it was also recognized that its speed is not sufficient to meet the criteria of a $7 per wheel cost, and thus it must be supplemented with a less expensive, faster technique. Of the possible fast, portable technologies, the magnetoelastic method appears very attractive. This technique measures residual stresses with the Barkausen noise generated by a external magnetic field applied to the sample[39,-40].

3.0 PRINCIPLES OF RESIDUAL STRESS MEASUREMENTS BY X-RAY DIFFRACTION AND HOLE-DRILLING

This section briefly reviews the elementary theory of stress analysis by x-ray diffraction and hole drilling. Further details can be found in the literature.[30-33, 41-44] As will be seen in Section 4.2.1, the data from railroad car wheels cannot be interpreted in terms of the simple classical theory of biaxial stresses developed in Section 3.1.1. On the contrary, it is essential to consider the role of shear stresses, the theory for which is reviewed in Section 3.1.2. Finally, because of the curved surfaces found in most locations of interest on wheels, it is essential to consider the errors introduced by inadvertent or unavoidable tilts of the diffratometer with respect to the component surface. A brief summary of the results, whose mathematical derivation is described in Appendix A, is given in Section 3.1.3. In addition, the hole drilling technique is described in Section 3.2.1 The hole drilling technique is used for confirmation of x-ray stress data and for evaluation of the stress variation with depth.

3.1 X-RAY DIFFRACTION

3.1.1 Basic Theory

The basis for the determination of residual stresses by x-ray diffraction is Bragg's Law for diffraction. Essentially monochromatic x-rays, produced in the x-ray tube when energetic electrons (50 keV) impinge on a pure metallic target (usually copper or chromium), are scattered by the atoms comprising the material under investigation. In a crystal in which the atoms have a known periodic arrangement (Figure 2), the constructive and destructive interferences among the scattered waves result in scattered radiation in sharp, well-defined locations given by the famous Bragg equation

$$n\lambda = 2d_{hkl} \sin \theta \qquad (3-1)$$

where

λ = X-ray wavelength,

d_{hkl} = atomic spacing of the (hkl) plane, and

θ = scattering angle of the diffracted peak.

From this, it is seen that an accurate determination of the scattering angle, θ, with a known wavelength radiation, λ, allows the determination of the d-spacing of the (hkl) plane.

In a polycrystalline material in which the grains take on random orientations, the (hkl) planes have a uniform distribution of their normals in space. However, at any given time, only those planes whose normals bisect the angle between the incident and diffracted beams will actually diffract. Thus, by changing the orientations of the components under investigation with respect to the diffractometer, it is possible to determine, with a high degree of accuracy, the changes in the d-spacings with orientation. In a stress-free material, all of these d-spacings should be equal (to

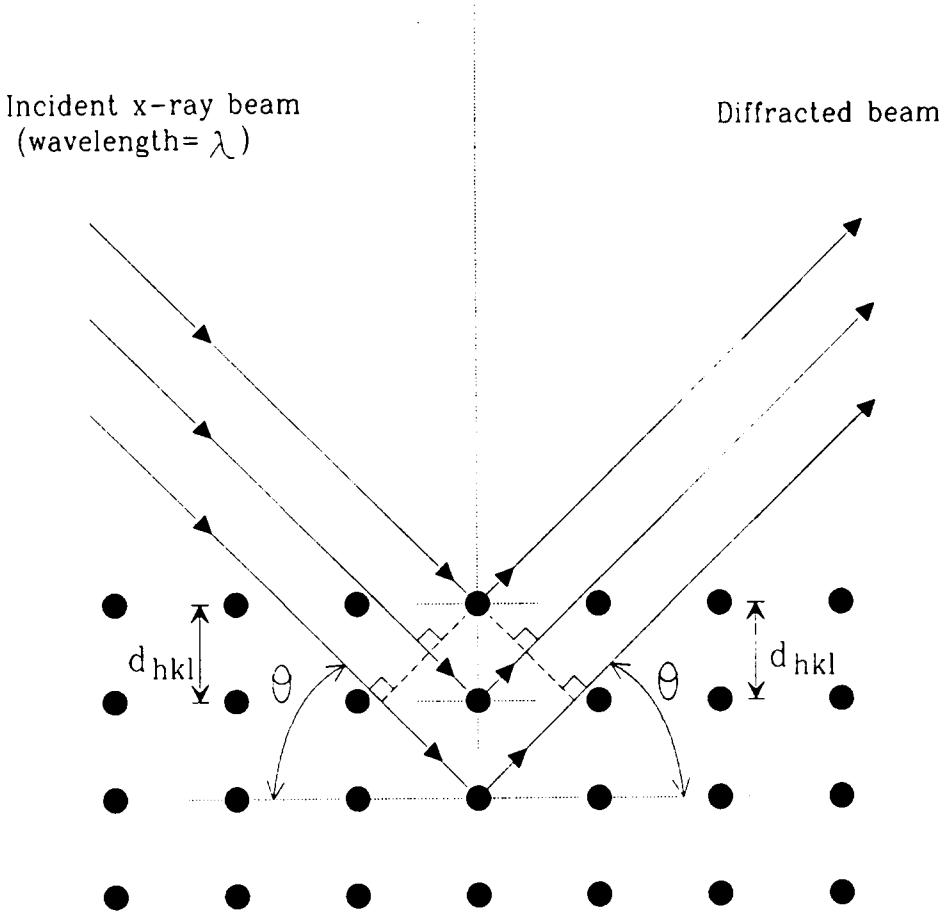

$$n\lambda = 2\,d\,\sin\vartheta$$

Figure 2. Bragg's Law from x-ray beam diffraction in the crystal structure.

about 1μÅ). However, if a stress is applied to the sample, there can be significant changes in the d-spacings. This concept is the basis of the technology used in this research program.

The relationship between the changes in the d-spacing of a given crystallographic plane and an applied triaxial stress field can be obtained with a Cartesian coordinate system transformation law, Hooke's law, and the strain-deformation relationship.[31,33] That is

$$\frac{d_{\phi,\psi} - d_0}{d_0} = \varepsilon_{\phi,\psi} = \frac{1}{2} S_2(\sigma_{11}\cos^2\phi + \sigma_{12}\sin^2\phi + \sigma_{22}\sin^2\phi - \sigma_{33})\sin^2\psi$$

$$+ \frac{1}{2} S_2\sigma_{33} - S_1(\sigma_{11} + \sigma_{22} + \sigma_{33})$$

$$+ \frac{1}{2} S_2(\sigma_{13}\cos\phi + \sigma_{23}\sin\phi)\sin 2\psi \quad . \qquad (3-2)$$

The term d_0 is the d-spacing of the (hkl) plane in the unstressed material, while $d_{\phi,\psi}$ is the d-spacing of that plane whose normal has an orientation (ϕ,ψ) with respect to the sample coordinate system (see Figure 3). S_1(hkl) and S_2(hkl) are x-ray elastic constants for the material, and the σ_{ij} are the components of the applied or residual stress tensor. A more detailed analysis, described in Section 3.13 and presented in full Appendix A, gives the general relationship for $d_{\psi,\Delta\psi,\chi,\Delta\chi,\phi}$ where (ϕ, ψ, χ) are these orinentation angles and ($\Delta\psi$, $\Delta\chi$) are misalignment errors. For an isotropic medium,

$$S_1(hkl) = -\frac{\nu}{E}$$

and

$$\frac{1}{2} S_2(hkl) = \frac{1+\nu}{E}$$

where E is Young's modulus and ν is Poisson's ratio. It is important to note that S_1 and S_2 are functions of the x-ray wavelength used and the Miller indices (hkl) of the diffracting planes. If the

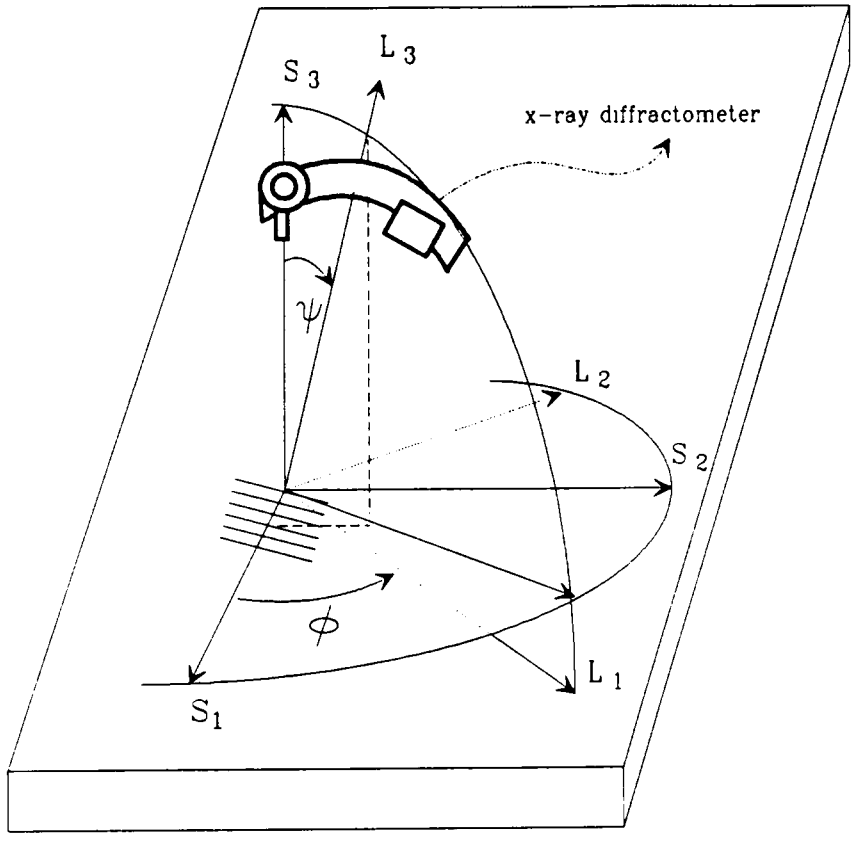

Figure 3. Orientation of crystal planes with respect to sample coordinate system.: Rotation ϕ about S_3 and ψ about L_2 (Notation follows Reference 31).

applied or residual stress field is biaxial, then $\sigma_{ij} = 0$ for i,j = 3. Under these conditions, Equation (3-2) reduces to

$$\frac{d_{\phi,\psi} - d_0}{d_0} = \frac{1}{2} S_2(hkl)[\sigma_{11}\cos^2\phi + \sigma_{12}\sin 2\phi + \sigma_{22}\sin^2\phi]\sin^2\psi \ . \qquad (3-3)$$

Calling the terms in the first bracket σ_ϕ, the stress in the ϕ direction, and realizing that at $\psi = 0$

$$\frac{d_{\phi,0} - d_0}{d_0} = S_1(hkl)[\sigma_{11} + \sigma_{22}]$$

Equation (3-3) can be reduced to

$$\frac{d_{\phi,\psi} - d_{\phi,0}}{d_0} = \frac{1}{2} S_2(hkl)\sigma_\phi \sin^2\psi \ . \qquad (3-4)$$

This result suggests that if the stress field is biaxial, a graph of $d_{\phi,\psi}$ versus $\sin^2\psi$ should be a straight line of slope $\frac{1}{2} S_2(hkl)\sigma_\phi$, and if the x-ray elastic constant S_2 is known, σ_ϕ can be obtained. It will be shown that in several cases this is a valid approximation. However, it will also be seen that this is often not the case and that, at a minimum, shear stresses must be taken into account.

3.1.2 Effect of Shear Stresses

It is clear from Equation 3-2 that if the shear stresses σ_{12}, σ_{13}, or σ_{23} are non-zero, the simple result given by Equation 3-4 is no longer valid. As will be seen from the data presented in Sections 4.2, this is often the case in the wheels.

Consider the case in which the coordinate system defining ϕ (see Figure 2) is defined along a known, simple symmetry direction of the component. For example, for measurements on the tread

of a wheel, define $\phi = 0$ to be in the circumferential or hoop direction. Substitution of $\phi = 0$ into Equation (3-2) yields

$$\frac{d_{0,\psi} - d_0}{d_0} = \frac{1}{2} S_2\sigma_{11}\sin^2\psi + \frac{1}{2} S_2\sigma_{33}\cos^2\psi + S_1(\sigma_{11} + \sigma_{22} + \sigma_{33}) + \frac{1}{2} S_2\sigma_{13}\sin 2\psi \qquad (3-5a)$$

and

$$\frac{d_{0,0} - d_0}{d_0} = \frac{1}{2} S_2\sigma_{33} + S_1(\sigma_{11} + \sigma_{22} + \sigma_{33}) \ . \qquad (3-5b)$$

Subtracting Equation (3-5b) from Equation (3-5a) gives

$$\frac{d_{0,\psi} - d_{0,0}}{d_0} = \frac{1}{2} S_2(\sigma_{11} - \sigma_{33})\sin^2\psi + \frac{1}{2} S_2\sigma_{13}\sin 2\psi \ . \qquad (3-6)$$

This result indicates that if the shear stress in the plane of rotation of the diffractometer is non-zero, the plot of $d_{0,\psi}$ versus $\sin^2\psi$ will be nonlinear and will be split for $\psi \neq 0$. Such effects are exactly what have been observed in many of the measurements. The two stress coefficients $(\sigma_{11} - \sigma_{33})$ and σ_{13} may be obtained by performing a multiple regression of $d_{0,\psi}$ versus $\sin^2\psi$ and $\sin 2\psi$, a procedure readily accomplished on a wide range of statistical analysis packages available on both mainframe and IBM-PC (International Business Machine-Personal Computer)[45] computers. ABSTAT[46] running on an IBM-PC clone and SAS[47] running on IBM-3090 were used for this project.

3.1.3 Effect of Sample Misalignment

The relationships between the x-ray measurements of crystal d-spacings and the various components of the stress tensor presented in Equations (3-2) and (3-6) were established implicitly assuming that the x-ray diffractometer was perfectly aligned with respect to the component surface at the location where the measurements were made. Because of the complicated geometry in the heat-discolored region in the plate of the wheel, the diffractometer had to be tilted by an angle (Figure 4) to measure residual stresses. This implies that the stress tensor was determined in a different coordinate system. Therefore, in order to correct the stress to the true stress tensor ($\chi = 0$ in Figure 4) in the coordinate perpendicular to the sample an equation for the coordinate transformation should be considered.

The result for this case, by applying $\Delta\psi = \Delta\chi = 0$ to Equation (A-21) of Appendix A, can be obtained:

$$\frac{d_{\psi,\chi,\phi} - d_{0,\chi,\phi}}{d_0} = \frac{1+\nu}{E}\sin^2\psi\,\{(\cos^2\phi - \sin^2\chi\sin^2\phi)\,\sigma_{11} + (\sin^2\phi - \sin^2\chi\cos^2\phi)\,\sigma_{22}$$

$$- \cos^2\chi\,\sigma_{33} + \sin 2\phi(1+\sin^2\chi)\,\sigma_{12}$$

$$+ \sin 2\chi(\cos\phi\,\sigma_{23} - \sin\phi\,\sigma_{13})\}$$

$$+ \frac{1+\nu}{E}\sin 2\psi\{\sin\chi[\frac{\sin 2\phi}{2}(\sigma_{11} - \sigma_{22}) + (\sin^2\phi - \cos^2\phi)\,\sigma_{12}]$$

$$+ [\cos\chi(\sin\phi\,\sigma_{23} + \cos\phi\,\sigma_{13})]\}\ . \qquad (3-7)$$

In Equation (3-7), $d_{\psi,\chi,\phi}$ is the d-spacing of the (hkl) planes obtained after rotating the same (hkl) planes, which are spaced by d_0, by a ψ, χ, and ϕ angles as shown in Figure 4. d_0 is the d-spacing in a stress free state and $d_{0,\chi,\phi}$ is the d-spacing obtained after rotating by χ and ϕ. In the typical case where $\phi = 0$, Equation (27) becomes

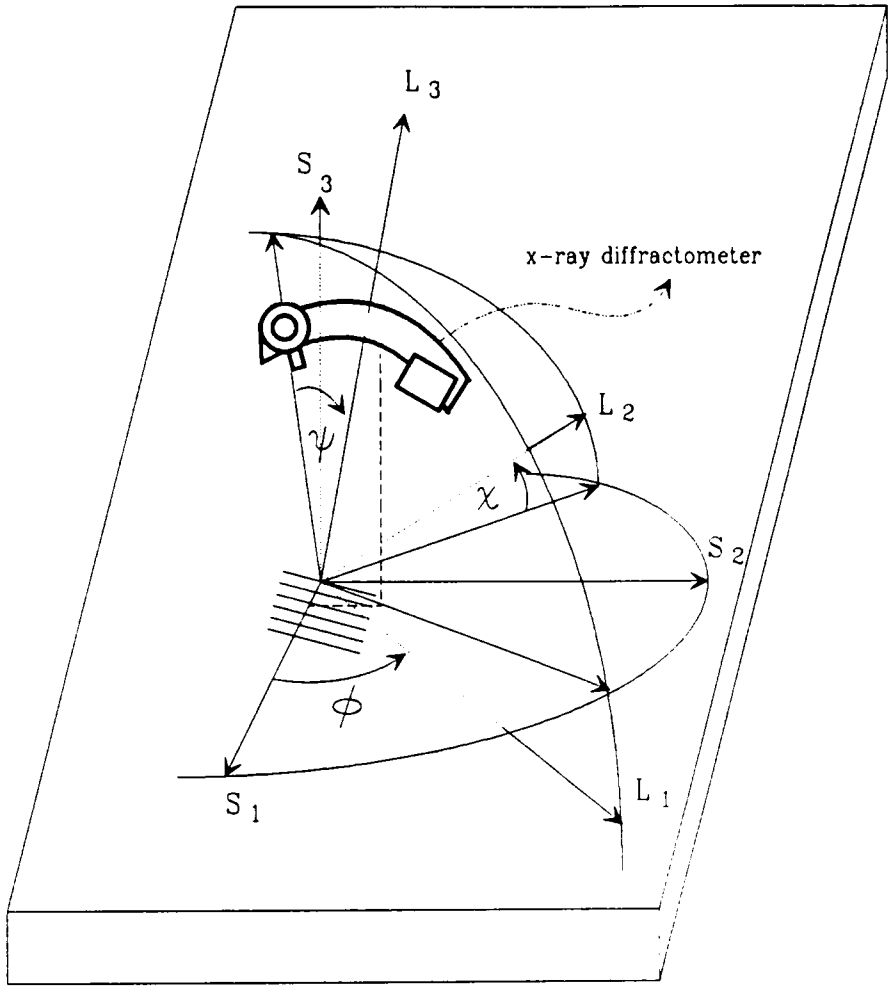

Figure 4. (a) A tilt of diffractometer due to complicated geometry of wheel.: (b)Orientation of crystal planes with respect to the sample coordinate system due to a tilt of the diffractometer. Rotation ϕ about S_3, ψ about L_2, and χ about L_2.

$$\frac{d_{\psi,\chi,\phi} - d_{0,\chi,\phi}}{d_0} = \frac{1+\nu}{E}\sin^2\psi\{(\sigma_{11}-\sigma_{33})[1 - \frac{\sin^2\chi(\sigma_{22}-\sigma_{33})}{\sigma_{11}-\sigma_{33}} + \frac{\sin 2\chi\sigma_{23}}{\sigma_{11}-\sigma_{33}}]\}$$

$$+\frac{1+\nu}{E}\sin 2\psi\{\cos\chi\sigma_{13} - \sin\chi\sigma_{12}\} \ . \qquad (3-8)$$

Thus it is seen that, depending on the specific values of the components of the tensor, the interpretation of the coefficients of the multiple regression of $d_{\psi,\chi,\phi}$ versus $\sin^2\psi$ and $\sin 2\psi$ as $(\sigma_{11}-\sigma_{33})$ and σ_{13} , respectively can lead to potentially significant errors. For this research, a χ tilt of the diffractometer of 18 degrees was applied at 3.5" from the rim corner in the plate of the six wheels. This means that the normal stress values determined at this location are 10% less than those obtained if this effect is ignored because $\sin^2 18° = 0.1$. For this result, it was the assumption that $\sin^2(18°) = 0.1$ and $\frac{(\sigma_{22}-\sigma_{33})}{(\sigma_{11}-\sigma_{33})} \simeq 1.0$. The x-ray normal stress in the x_2 axis, $(\sigma_{22}-\sigma_{33})$, can not be determined near the rim due to the wheel geometry. However, at other locations it was found that $\frac{(\sigma_{22}-\sigma_{33})}{(\sigma_{11}-\sigma_{33})} \simeq 1.0$. (i.e. $\sigma_{11} \simeq \sigma_{22}$). Therfore this assumption was also made at these locations. The importance of these corrections explains some of the difficulty Professor Hendricks[48] has had in interpreting the data from flat sheets of nickel-plated steel which were tilted through large χ-angles in an attempt to avoid serious preferred orientation problems.

X-ray stress measurements need careful alignment of the x-ray diffractometer with respect to the sample because misalignment of the x-ray diffractometer can lead to significant errors in the stress determination by the diffractometer. Accordingly, the effect of misalignment has been studied by many researchers[49-55] , who found that the misalignmnets were caused by sample displacement, sample curvature, and the deviation of true zero position of ψ. However, $\Delta\psi$ and $\Delta\chi$ misalignments of the x-ray diffractomter had not been considered specifically. Hence, they were examined in detail in this research.

The generalized equation considering these misalignments is derived in Appendix A. The resulting equation giving corrections for these misalignments is considered here. When the exper-

imental misalignment errors, $\Delta\psi$ and $\Delta\chi$, are small and $\chi = 0$ (no deliberate tilt of specimen and /or instrument), Equation (A-21) of Appendix A becomes:

$$\frac{d_{\psi\,\Delta\psi\,\Delta\chi\,\phi} - d_{0\,\Delta\psi\,\Delta\chi\,\phi}}{d_0} = \frac{1+\nu}{E}\{[\cos^2\phi\sigma_{11} + \sin^2\phi\sigma_{22} - \sigma_{33} + \sin 2\phi\sigma_{12}]$$

$$+ [-4S\phi\,\sigma_{23} - 4\,C\phi\,\sigma_{13}]\,\Delta\psi$$

$$+ [-2\,C\phi\,\sigma_{23} - 2\,S\phi\,\sigma_{13}]\,\Delta\chi\}\,\sin^2\psi$$

$$+ \frac{1+\nu}{E}\{[S\phi\,\sigma_{23} + C\phi\,\sigma_{13}]$$

$$+ [\cos^2\phi\,\sigma_{11} + \sin^2\phi\sigma_{22} - \sigma_{33} + \sin^2\phi\,\sigma_{12}]\,\Delta\psi$$

$$+ [\frac{\sin 2\phi}{2}\,\sigma_{11} - \frac{\sin 2\phi}{2}\,\sigma_{22} + (\sin^2\phi - \cos^2\phi)\,\sigma_{12}]\,\Delta\chi\}\,\sin 2\psi. \qquad (3-9)$$

If $\phi = 0$ (no deliberate rotation of specimen and /or instrument), Equation (A-22) becomes

$$\frac{d_{\psi\,\Delta\psi\,\Delta\chi} - d_{0\,\Delta\psi\,\Delta\chi}}{d_0} = \frac{1+\nu}{E}\{[\sigma_{11} - \sigma_{33}] - 4\,\sigma_{13}\,\Delta\psi - 2\,\sigma_{23}\,\Delta\chi\}\,\sin^2\psi$$

$$+ \frac{1+\nu}{E}\{\sigma_{13} + [\sigma_{11} - \sigma_{33}]\,\Delta\psi - \sigma_{12}\,\Delta\chi\}\,\sin 2\psi. \qquad (3-10)$$

Equation (3-10) implies that $\Delta\psi$ and $\Delta\chi$ induce fictitious shear stresses because they are multiplied by $(\sigma_{11} - \sigma_{33})$ and σ_{12}, respectively, in the second term of the right hand side. It is noted that the magnitude of the errors in the x-ray stress measurement depends on both the misalignments and the stress condition. Thus, it is also critical that the diffractometer be carefully aligned such that $\Delta\chi = \Delta\psi = 0$.

Figure 5. Technology for Energy Corporation (TEC) Model 1670 Mobile X-Ray Stress Analysis System[56,57]

3.1.4 Experimental Technique

The residual stress measurements were made using a Technology for Energy Corporation (TEC) Model 1610 Mobile X-Ray Stress Analysis System. A photograph of this unit is shown in Figure 5. The measurements were made with vanadium-filtered Cr K_α radiation (λ = 2.2906 Å) diffracted from the (211) planes of iron. The radiation was recorded in a Xenon-filled linear position-sensitive x-ray proportional counter[58]. The low-power x-ray tube was operated at 35 kV and 1.7 mA. Typically, pinhole collimators 4 mm in diameter were used. Data were collected for 60 s per ψ-angle for each stress measurement, and 7 angles were recorded in an angular range of -45 to +45°. Under some circumstances, other collimators, measuring times, and numbers of ψ-angles were used as dictated by the data to be acquired. The x-ray elastic constant S_2 was obtained from the literature and was programmed into the TEC software system.[59]

The acquired data were recorded in the on-line Digital Equipment Corp. (DEC) LSI 11/23 Plus minicomputer and were stored on floppy disks. The software system applied all standard x-ray diffraction corrections to the data-background scattering, sample absorption, Lorentz polarization, Compton scattering and then computed, by a least squares fitting routine, the angular position of the diffraction peak. Bragg's law was used to compute the d-spacing of the lattice planes (Equation 3-1). Corrections were made for $K_{\alpha 1} - K_{\alpha 2}$ wavelength spreads and for sample tilts. The resultant data were then plotted as d versus $\sin^2\psi$ plots as required by Equations (3-4) and (3-6). Typical results of these analyses are shown in Figures 6 and 7. It is to be noted that almost 1000 such two-page computer analyses were performed in obtaining the data presented in Sections 4 and 5. Instead of reporting each and every one of the analysis in this dissertation, only the final results are reported here. The original data are available from Professor Hendricks.

It is to be noted that the data in Figure 6 show no $\sin^2\psi$ split while the data of Figure 7 show a significant split. This is of particular significance to the correct interpretation of stresses in railroad car wheels. These data were acquired at two different locations on the same wheel (serial number 37334), and indicate that location B has significant shear stresses present. Use of standard multiple

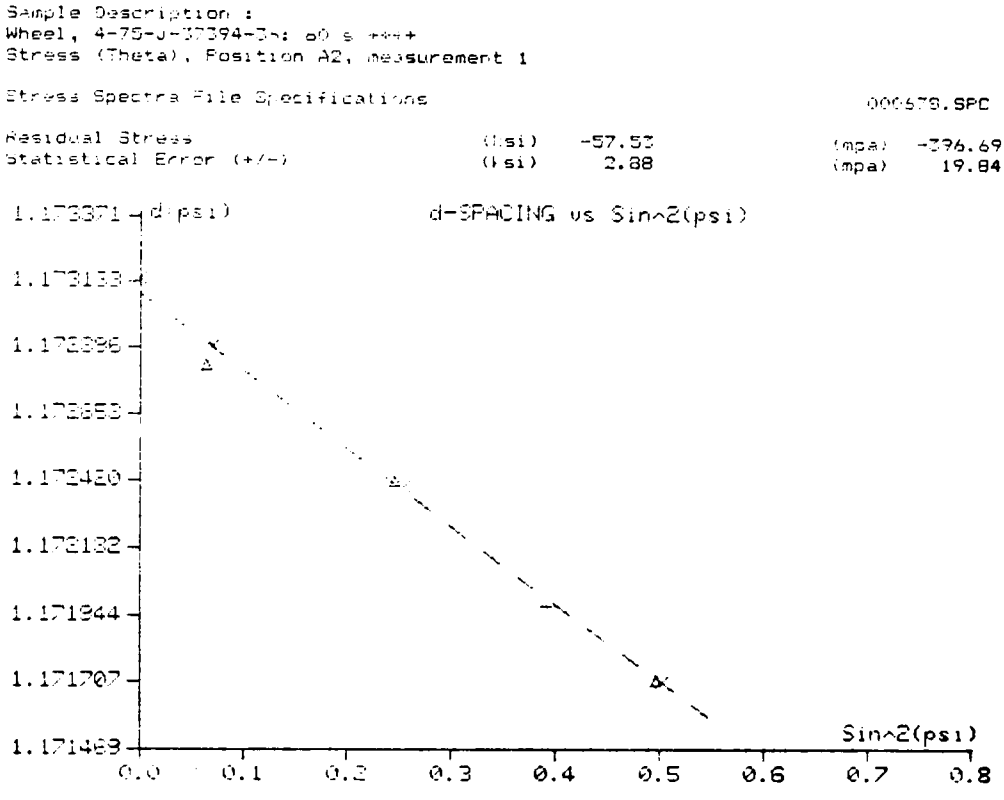

Figure 6. Typical d versus $\sin^2\psi$ plot for a railroad wheel steel in which no shear stresses are present.

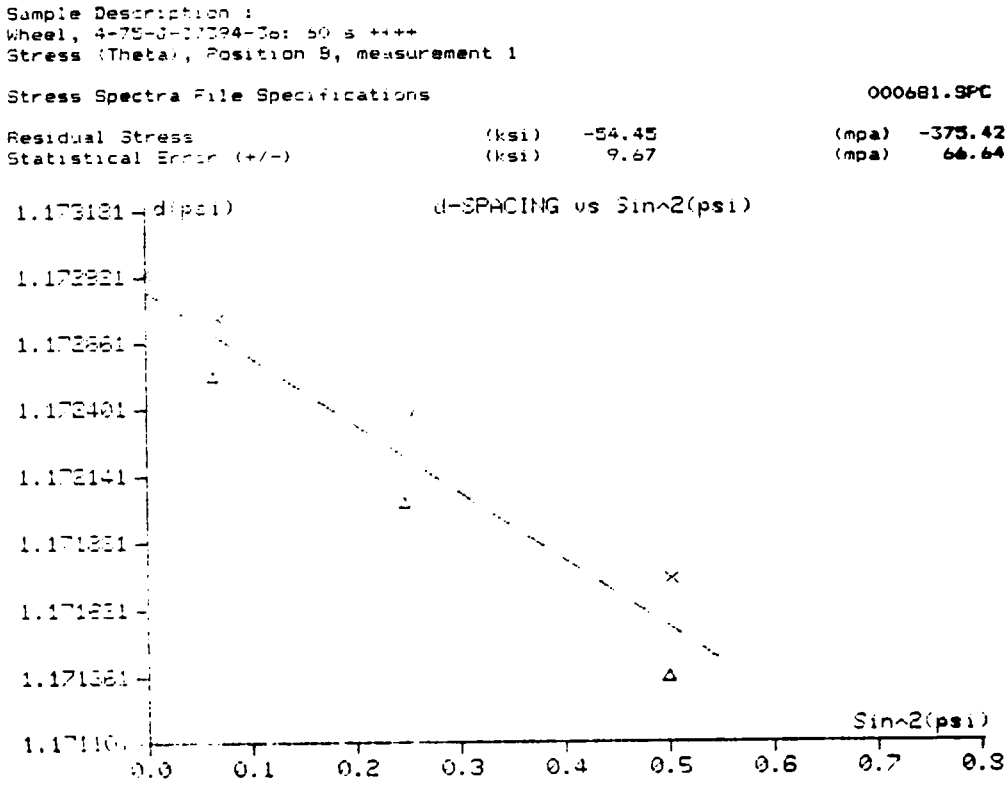

Figure 7. Typical d versus $\sin^2\psi$ plot for a railroad wheel steel in which shear stresses are present.

regression techniques on an IBM-PC compatible personal computer allowed the fitting of Equation (3-6) to such data to recover accurate values for both the normal stresses and the shear stress as well as estimates of the variance of each stress. These data will play a critical role in the statistical interpretations presented in Sections 4 and 5. Additional information concerning the use of the TEC X-ray Analysis System can be found in the TEC Operation and Maintenance Manual[60]

3.2 HOLE DRILLING

3.2.1 Basic Theory

The determination of residual stress by hole drilling is based on the relaxation of the neighboring material surrounding the position where the hole is drilled. The material relaxation is evaluated by reading strains from a strain gage rosette attached to the desired location. Using Kirch's approach to the stress field around a circular hole, the superposition principle for the stress states before and after the introduction of a hole, Hooke's law[41-44,61-63], and the assumption of a uniaxial stress field, the relationship for the relaxed radial and tangential strains in the plate after a hole is made are

$$\varepsilon_{rr} = \sigma_{ii}(A + B\cos 2\theta) \qquad (3-11a)$$

$$\varepsilon_{\theta\theta} = \sigma_{ii}(-A + C\cos 2\theta) \qquad (3-11b)$$

where

σ_{ii} = uniaxial stress in the i coordinate

$A = -\frac{1+\nu}{2E}(\frac{a}{r})^2$

$B = -\frac{1+\nu}{2E}[(\frac{4}{1+\nu})(\frac{a}{r})^2 - (\frac{a}{r})^4]$

$C = -\frac{1+\nu}{2E}[-(\frac{4}{1+\nu})(\frac{a}{r})^2 + (\frac{a}{r})^4]$

θ = angle between coordinates (refer to Figure 8).

If the biaxial stresses (σ_{11} and σ_{22}) are assumed, the radial component of the strain is:

$$\varepsilon_{rr} = A(\sigma_{11} + \sigma_{22}) + B(\sigma_{11} - \sigma_{22})\cos\theta \ . \qquad (3-12)$$

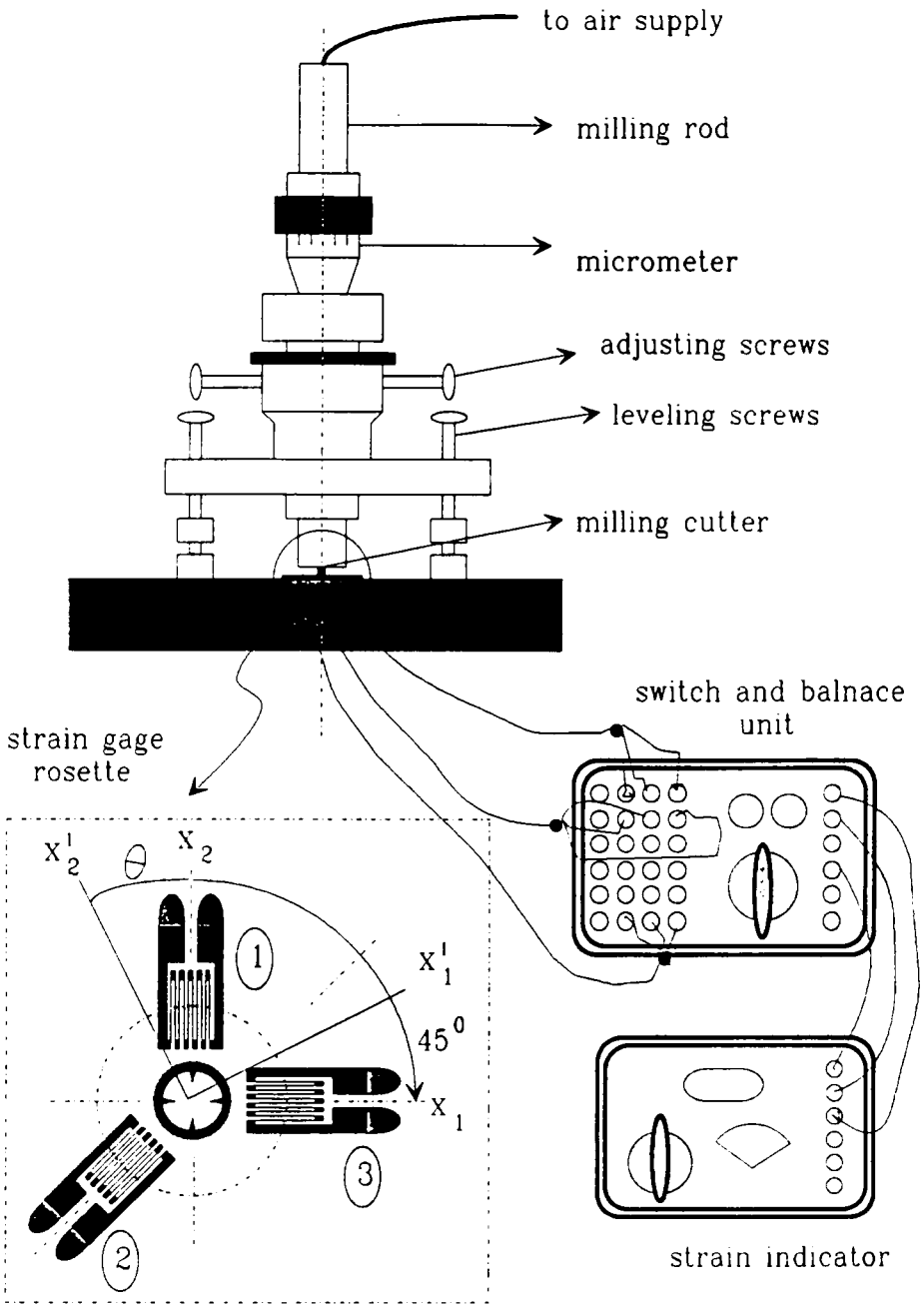

Figure 8. Milling guide, radially oriented strain gage rosette, strain indicator, and balance unit.

Only Equation (3-11a), the ε_{rr} term, is used for the derivation of Equation (3-12) because the relieved radial strain, ε_{rr} , is known to be significantly greater than tangential strain, ε_{θ}. As a result, commercial strain gage rosettes are designed with radially oriented grids as shown in Figure 8.[44] The two principal stresses and the angle between the direction of one of the principal stress and the coordinate system of the rosette may be obtained by evaluating Equation (3-12) at three different orientations. This is accomplished through the use of a strain gage rosette as shown in Figure 8.

The equations for determining minimum and maximum stresses and the direction of the principal stresses can expressed in terms of three strains which are obtained from the three radially oriented strain gage rosette with the geometry. The equations are:[41–44,64,65]

$$\sigma_{\max} = \frac{\varepsilon_1 + \varepsilon_3}{4A} - \frac{\sqrt{2}}{4B}\sqrt{(\varepsilon_1 - \varepsilon_2)^2 + (\varepsilon_2 - \varepsilon_3)^2} \qquad (3-13a)$$

$$\sigma_{mim} = \frac{\varepsilon_1 + \varepsilon_3}{4A} + \frac{\sqrt{2}}{4B}\sqrt{(\varepsilon_1 - \varepsilon_2)^2 + (\varepsilon_2 - \varepsilon_3)^2} \qquad (3-13b)$$

$$\tan 2\theta = \frac{\varepsilon_1 + \varepsilon_3 - 2\varepsilon_2}{\varepsilon_3 - \varepsilon_1} \quad . \qquad (3-13c)$$

where

$\varepsilon_1 < \varepsilon_3$: θ refers to σ_{max} ,

$\varepsilon_1 > \varepsilon_3$: θ refers to σ_{min} ,

$\varepsilon_1 = \varepsilon_3$: $\pm\theta = 45$,

$\varepsilon_1 < \varepsilon_2$: σ_{max} at + 45°,

$\varepsilon_1 > \varepsilon_2$: σ_{max} at - 45°,

and θ is the angle from gage 1 to the nearer principal axis.

These equations determine the average residual stresses over a volume from the sample surface to a certain depth after a hole is drilled through a thin plate. In order to use these equations for the blind hole case where the hole does not penetrate through the plate, certain factors such as strain gage rosette geometry, milling cutter size, and hole depth should be considered since parameters A and B are dependent upon them. In reality, the parameters should be determined by an experiment

with the same sample condition, which is virtually impossible in almost all practical cases including this research. Fortunately, Schajer[64] has determined these parameters based on a finite element analysis. For this research, his values of the parameters were used.

In the preceeding analysis, a biaxial state of stress in which $\sigma_{11} = 0$ has been assumed. Nichola[65] has shown that an approximation for depth dependence of the residual stresses can be obtained with the following relationship:

$$\sigma_{n'} = \frac{\sigma_n Z_n - \sigma_{n-1} Z_{n-1}}{Z_n - Z_{n-1}} \qquad (3-14)$$

where

σ'_n = approximate residual stress in the nth drilling

σ_n , σ_{n-1} = average stress from the surface to depth, and

Z_n , Z_{n-1} = depths of drilling increments n and n-1.

The stress components in the sample coordinate system can be obtained using a Cartesian coordinate system stress transformation law, $\sigma'_{ij} = a_{im} a_{jn} \sigma^{61,63}_{mn}$ (The detailed expansion of the transformation law is presented in Appendix A):

$$\sigma_{11} = \cos^2\theta \sigma'_{11} + \sin^2\theta \sigma'_{22} \qquad (3-15a)$$

$$\sigma_{22} = \sin^2\theta \sigma'_{11} + \cos^2\theta \sigma'_{22} \qquad (3-15b)$$

where the strain gages 1 and 3 represent σ_{22} and σ_{11} , respectively, and σ'_{11} and σ'_{22} are the principal stresses (Figure 8). After strains are read from the strain gage rosette, the average and the approximate residual stresses in the principal coordinate system and the stress components in the sample coordinate system may be easily obtained on a personal computer using Equations (3-12) to (3-15) and a spreadsheet program such as Lotus 123[66].

3.2.2 Experimental Technique

The residual stress measurements were made using several strain gage devices supplied by the Measurement Group with the following procedure. After the sample surface was cleaned with the cleaning solution provided by the Measurement Group, a strain rosette (Figure 8), Measurement Group TEA-06-062RE-120, was applied at the position where the stress was to be measured[67,68]. The wires were connected between strain gages and a portable strain indicator, Measurement Group Model P-3500[69], which converted a change in the resistance of the strain gage to the voltage signal and calibrated itself. Since the strain rosette was used, a portable switch and balance unit, Measurement Group Model SB-10[70] was connected to the strain indicator. Each strain gage in the rosette was balanced and switched individually by the unit before the measurements[70]. A milling guide, Measurement Group Model RS-200 [71], was centered over the strain gage rosette and then cemented to the sample. The milling rod was inserted into the milling guide after the milling cutter was inserted into the rod. The air supply system was assembled to the rod. Then nitrogen gas (about 20-35 psi) was applied to rotate the milling cutter to cut a hole. At each 0.0025″ increment of the hole depth, the strains were read from the strain indicator. After each increment, the milling cutter was stopped for 10 seconds to cool the sample[72]. A new milling cutter was used for every measurement position in order to obtain more accurate and consistent data[72]. The parameters A and B in Equation (3-12) of Section 3.2.1 for residual stress determination were obtained from Schajer's table[64] , which considered the strain gage rosette, milling cutter, and hole depth. Additional information in the use of this experimental technique can be found in the references 72 through 74.

4.0 RESIDUAL STRESSES IN RAILROAD CAR WHEELS

In this section the results of the investigation of residual stresses in the six wheels provided by CSX Transportation are reported. Section 4.1 describes the analytical procedures and methods, including a description of the wheels studied, metallographic chracterization, wheel terminology, the design and construction of special carriers which allow the performance of the x-ray measurements at nearly any location on each wheel, the procedures used to prepare the wheel surfaces for measurement, and the choice of measurement locations. Section 4.2 presents the experimental results, including their variation with axial location and with azimuthal location on the wheels, and a comparison of the results from the wheels of varying service histories. This analysis shows that there are statistically significant differences between the observed stresses in certain key locations on these wheels. In addition, the x-ray and hole drilling residual stress data are intercompared. The residual stress variation with depth obtained by the hole drilling technique is shown.

4.1 PROCEDURE

4.1.1 Description

Six railroad car wheels of various service histories were provided by CSX Transportation for this investigation. Included were four flat plate and two curved plate wheels. Two were new, two were used with normal wear, and two were heat discolored. One of the heat-discolored wheels had severe tread grooves. The details of each wheel, plus two other wheels of lesser known service histories - wheels which were held in reserve - are presented in Table 1. It is important to note several of the major differences among these wheels. They were produced by three different manufacturers over a period of 12 years; one was a wrought wheel (H-36 in Table 1), the others were cast (CH-36 in Table 1); one was a class C heat-treatment, while the others were class U, and two different stress designs were represented (flat and curved plate). Although, as will be seen in the analysis section, such a wide choice of parameters makes detailed statistical intercomparisons of the results from one wheel to the next quite difficult and subject to larger uncertainties than are normally desirable, it was important to initially determine if there were any major residual stress differences among the wheels which could be attributed to these variables. Thus it was concluded that in this research it was important to examine a variety of wheels which were representative of those most commonly found in service in the industry.

4.1.2 Optical Metallography and Hardness

For microstructural analysis, small sections were taken from the inner corner of the hub (Figure 9) of the the wrought, normal wear wheel (Wheel A) and the cast, normal wear wheel

Table 1. Wheels shipped to Virginia Polytechnic Institute in 1987 for residual stress measurements[75]

	A	B	C	D	E	F
Manufacturer	Sumimoto	Abex	Griffin-GS	Griffin-GC	Griffin-GX	Abex
Serial Number	37334	125049	59494	61681	17636	169518
Production Date	4-75	8-82	3-87	11-87	7-81	9-76
Furnishing Shop	RCS 7-87	RCS 7-87	RCS 7-87	LVLE 12-87	RCS 12-87	RCS 12-87
Design	H-36	CH-36	CH-36	CH-36	CH-36	CH-36
Stress Design	High	Low	Low	Low	Low	High
Plate Design	Flat	Curved	Curved	Curved	Curved	Flat
Class of Heat Treat.	U	U	C	U	U	U
Apparent Defects	Normal Wear	Severe Tread Grooves; Heat Discolor.	New Misfit	None	Greater 4" Heat Discolor.	Normal Wear
Tread/Flange			27/16; 23/16	14/16; 4 pts.	14/16; 4 pts.	

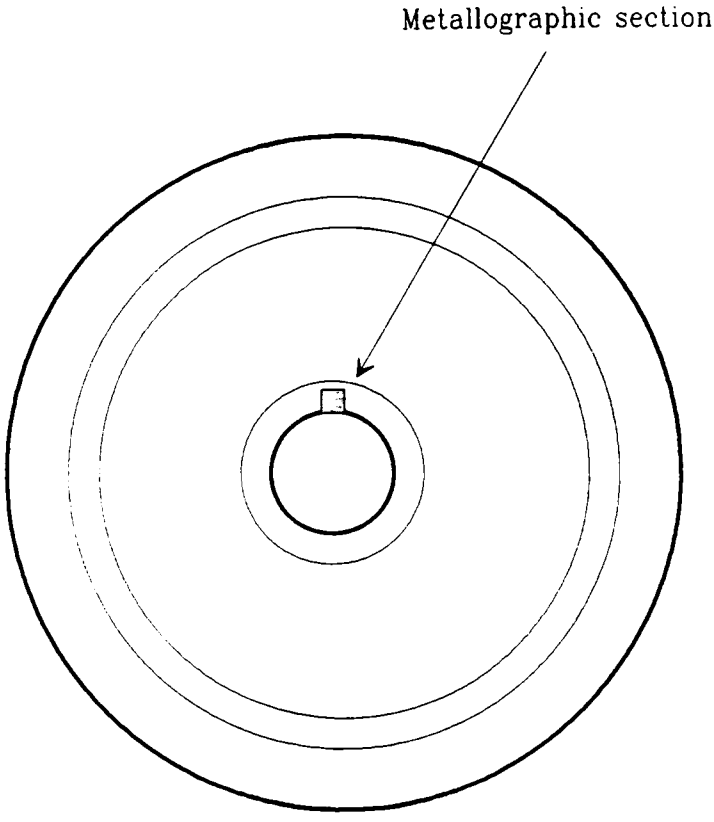

Figure 9. Location of microsection on the hub.

(Wheel F). Microstructures of other areas such as the tread, flange, and front and back rim were not determined. This was because destruction of the wheels for microstructural analysis changes their stress field and could cause catastrophic failure. Furthermore, it is expected that these wheels will be used in future experiments such as magnetoelastic analysis and saw cutting. The microstructures of these areas of wheels with different service histories have been studied by other research groups[34,76].

After polishing the microsections and etching them with 2% nital, micrographss were made using a LECO NEOPHOT-21 light metallographic microscope. Scanning electron micrographs (SEM) were made on the same samples using a JEOL JSM-35 equipped with a KeVex x-ray flourescence analyzer. The micrographs are shown in Figures 10 and 11. Both microstructures show that the wheel is a essentially fully pearlitic steel as pointed out by Carter et al[34].

From these micrographs, prior austenite grain size and pearlite colony size were assessed using the linear intercept method[77,78] and interlamellar spacing was determined using the method described by Ridly.[79] The results are shown in Table 2. Table 2 shows there is no difference in interlamellar spacing for the two samples. However, the prior austenite grain size of the wrought, normal wear wheel is shown to be about three times larger than that of the cast, normal wear wheel while the pearlite colony size was about 50 percent greater. The difference in pearlite colony size of the two wheels was also imdicated by their microhardnesses. This test showed that the microhardness of the wrought, normal wear wheel was 230 VHN_{300} and that of the cast, normal wear wheel was 529 VHN_{300}. The microhardeness test was carried out with a LECO DM-400 Hardness Tester using the method described by Dillinger.[80]

The microstructure in the rim of wheels subjected to severe braking has been reported by Wardriso and Devez.[76] There it was found that if cast-iron brakes were used, three different regions of microstructure were formed as a result of the heat generated by brake shoe contact with tread. First, the microstructure near the tread surface consisted of martensite, nodular pearlite, and bainite. Beneath the surface, in the tempered area, the microstucture becomes ferrite, pearlite, and spherodized

(a)

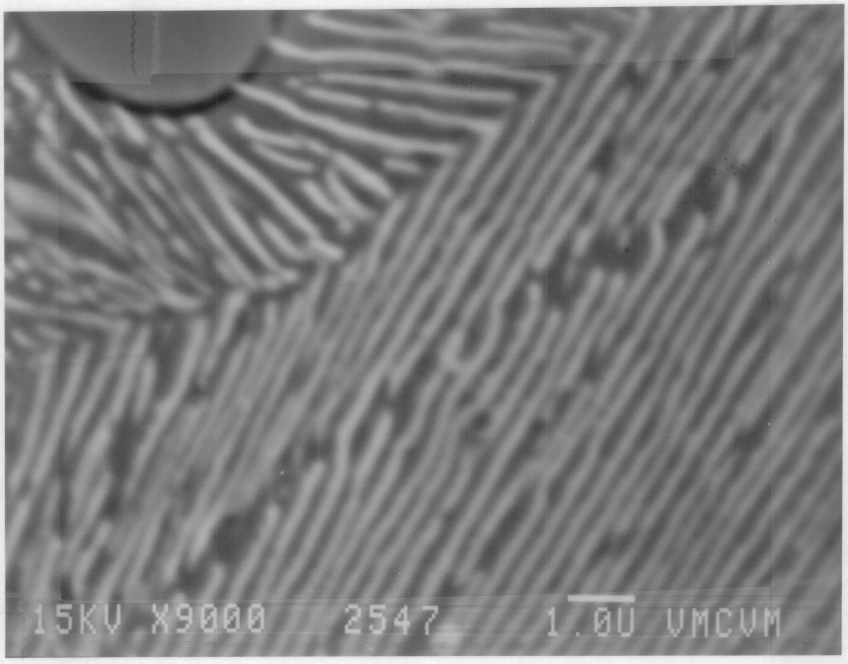

(b)

Figure 10. Photomicrographs of the microsection in the hub of wrought, normal wear wheel.: (a) SEM at X1000 magnification (b) light micrograph at X100 magnification, etchant : 2% nital.

(a)

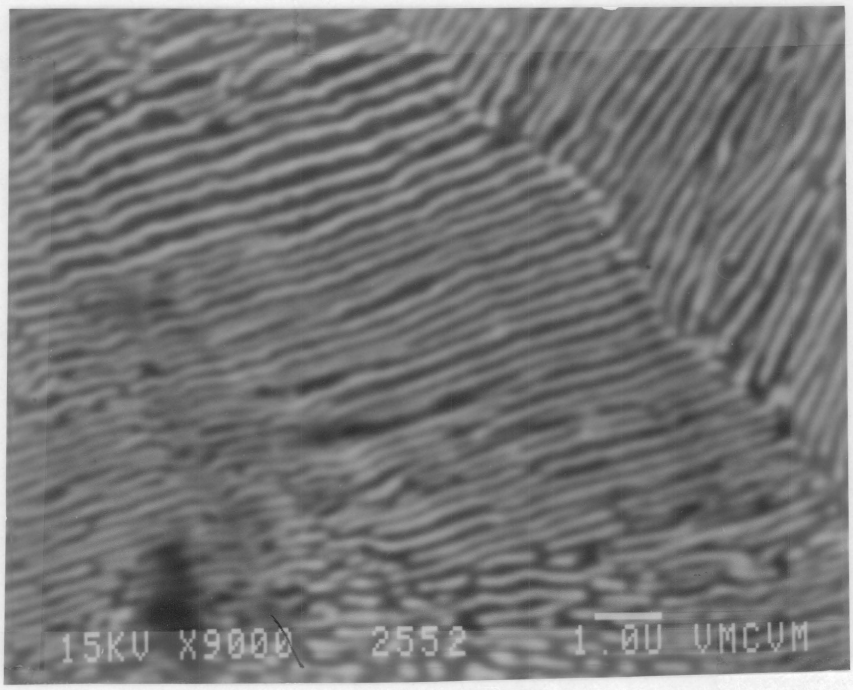

(b)

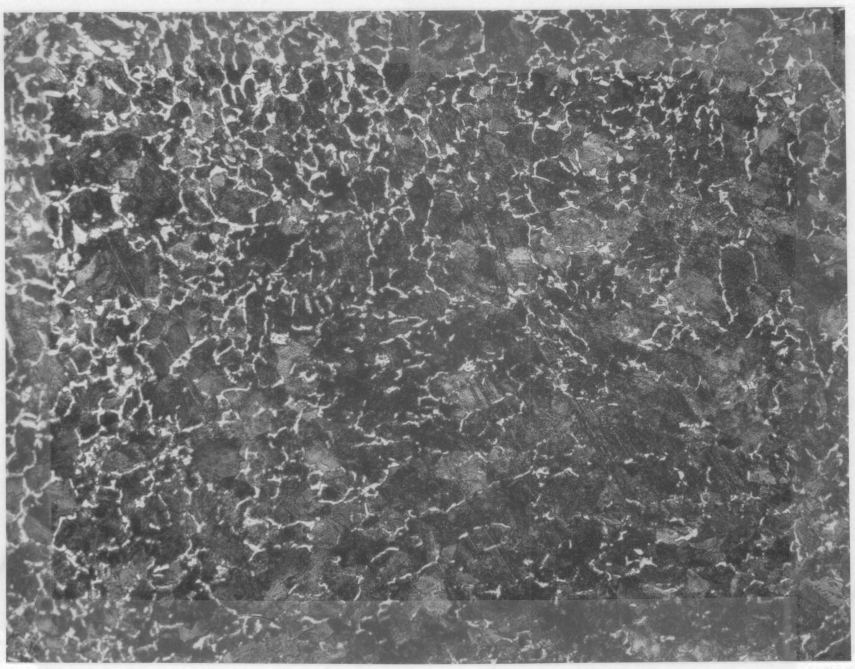

Figure 11. Photomicrographs of the microsection in the hub of cast, normal wear wheel.: (a) SEM at X1000 magnification (b) light micrograph at X100 magnification, etchant : 2% nital.

Table 2. Microstructural features determined in the hub of wrought and cast, normal wear wheels.

	Wrought wheel	Cast wheel
Pearlite interlamellar spacing (μm)	0.28±0.02	0.25±0.02
Pearlite Colony size (μm)	32±5	21±5
Prior austenite grain size (μm)	114±8	33±2
Hardness (VHN_{300})	230	529

carbides. In the next region, positioned below the heat affected areas, fine pearlite with a small amount of proeutectoid ferrite at the grain boundaries was produced. However, if composite brake shoes were used, less heat was generated than with cast-iron brakes because the composite brake shoes are designed to have a higher coefficient of friction.[81] As a result, the tread is tempered and the microstructure even near the tread surface consists of ferrite, pearlite and spherodized carbides as well.

4.1.3 Design and Construction of Wheel Carriers

Two wheel carriers were designed and constructed which permitted x-ray residual stress measurements to be made in any direction at almost any location on the wheel. The first carrier provided for vertical mounting (in order to allow movement of mounted wheels through standard 36-inch doorways) and rotation of the wheel about its center. The mounting angle fixture with clamps and brackets allowed the positioning of the x-ray diffractometer head and milling guide at almost any location on any surface of the wheel which might prove to be important or interesting from a stress point of view. Schematic diagrams of this carrier are shown in Figures 12 and 13. The x-ray diffractometer mounted on the carrier and the articulated arm of the diffractometer are shown in Figure 12. Figure 13 shows the hole drilling equipment: milling guide, strain indicator, and balance unit. (Note: There are some locations at which x-ray measurements could not be made because of the restrictions due to the geometry of the wheel and the x-ray head.) The carrier has been found to perform satisfactorily.

The second carrier was a simple device, constructed of four sections of 6 x 6 inch timbers bolted together and mounted on wheels. This unit allowed movement of the railroad wheel into any orientation for the measurements on the rim, hub, and plate. A schematic drawing showing the x-ray diffractometer positioned on the plate area of a wheel is shown in Figure 14.

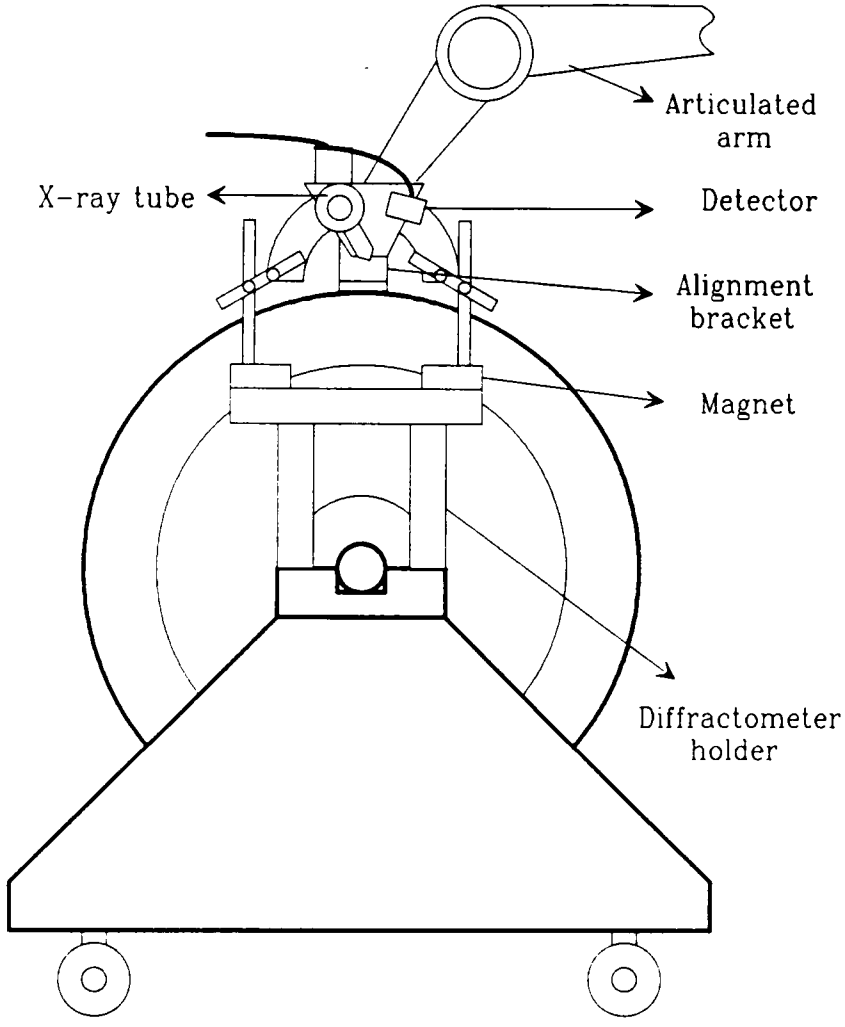

Figure 12. Schematic drawing of vertical wheel carrier with the x-ray diffractometer mounted.

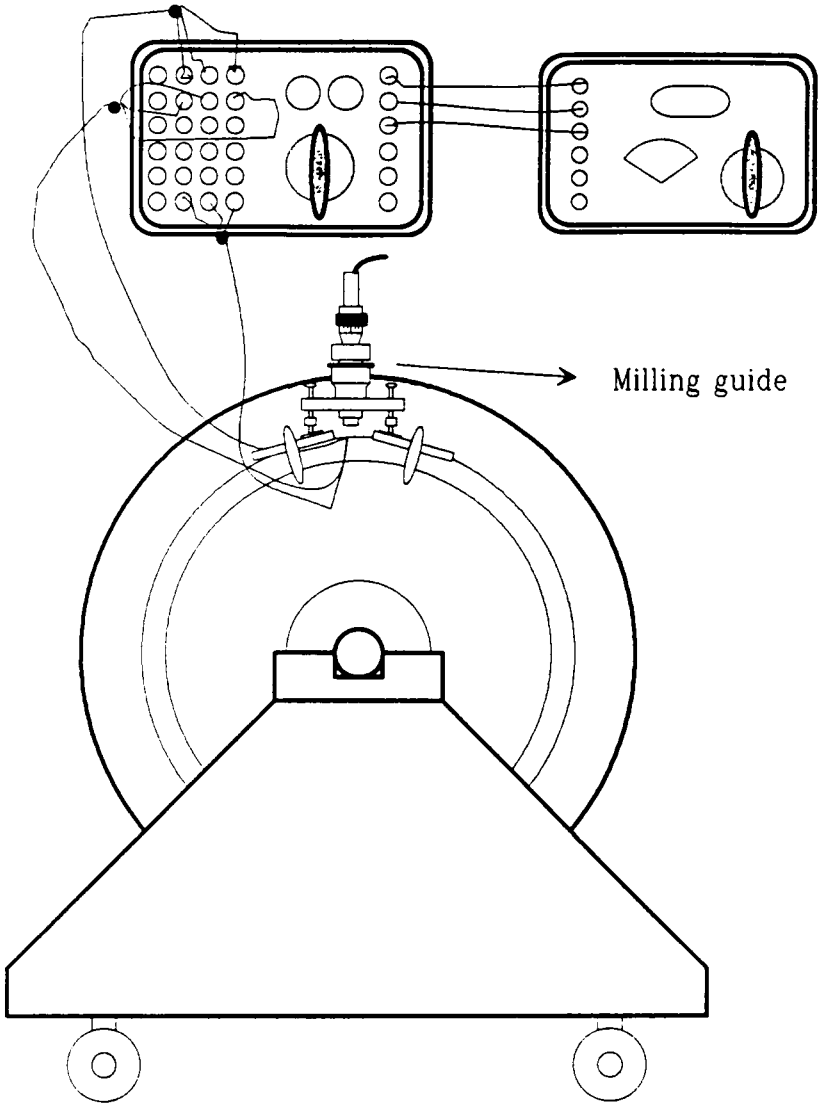

Figure 13. Schematic drawing of vertical wheel carrier with the hole drilling device mounted.

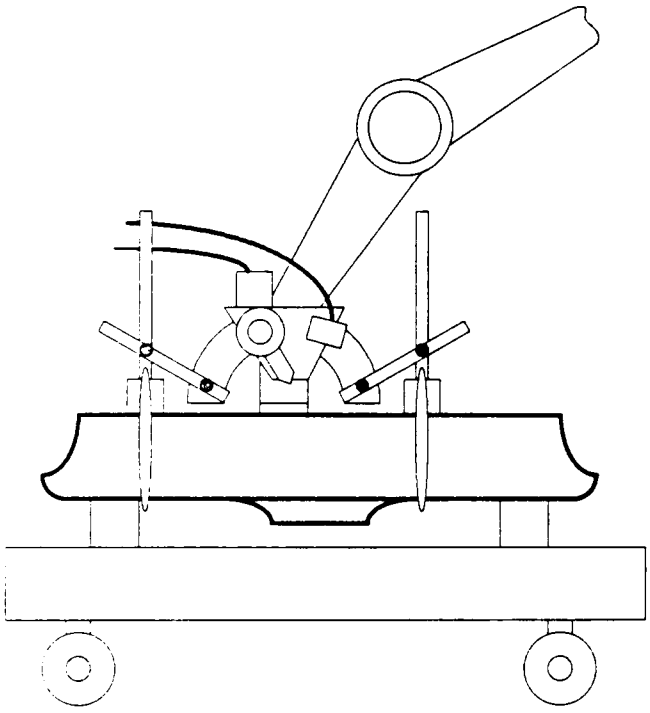

Figure 14. Schematic drawing of horizontal wheel carrier with the x-ray diffractometer mounted.

4.1.4 Surface Preparation

The effect that rust on the surfaces to be measured might have on the ability to accurately determine residual stresses in wheels caused major concern. Through contacts at Caterpillar Tractor Company, the formulas of two different solutions known to remove rust were obtained. One, a mixture of hydrochloric and nitric acids, was believed to also remove some of the base metal of the wheel. Although this first solution was completely successful in removing rust from the wheels, a second organic-based solution was sought because of the desire to measure the surface residual stress without the need to correct for the removal of any material. The solution of choice, based on 2-butyne-1,4 diol which acts as a strong inhibitor on the acid, was found to completely remove rust with no apparent effect on the base metal. This solution was routinely used for cleaning the wheels. It was found in measurements on the wheel tread where there was not as much rust as on the plate, that measurements before and after the rust removal treatment gave statistically equivalent results. Thus, it is believed that all problems associated with wheel preparation for reliable stress measurements were solved.

4.1.5 Choice of Measurement Locations

Although examination of the literature indicates that wheel fractures initiate at a few well-defined locations[34], it was believed to be important to thoroughly characterize the state of surface residual stress at a wide range of locations in railcar wheels. A cross section of a wheel with the various wheel terminologies is shown in Figure 15. Sixteen locations were defined on the hub, plate, rim, tread and flange of the wheel as depicted in Figures 16 and 17.

It is of critical importance if the technology developed in this research is to be applied in service that the stresses which characterize an overheated wheel be measured as rapidly as possible. This

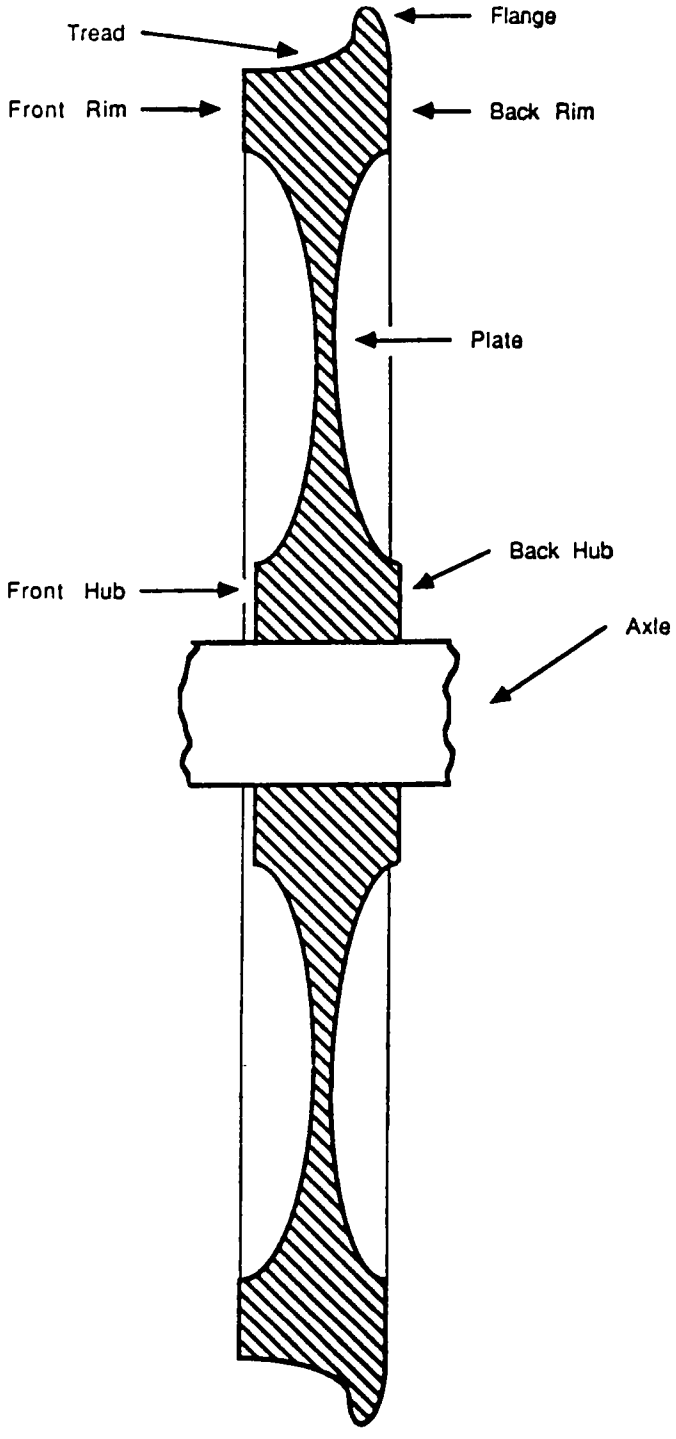

Figure 15. Wheel terminology[2,83].

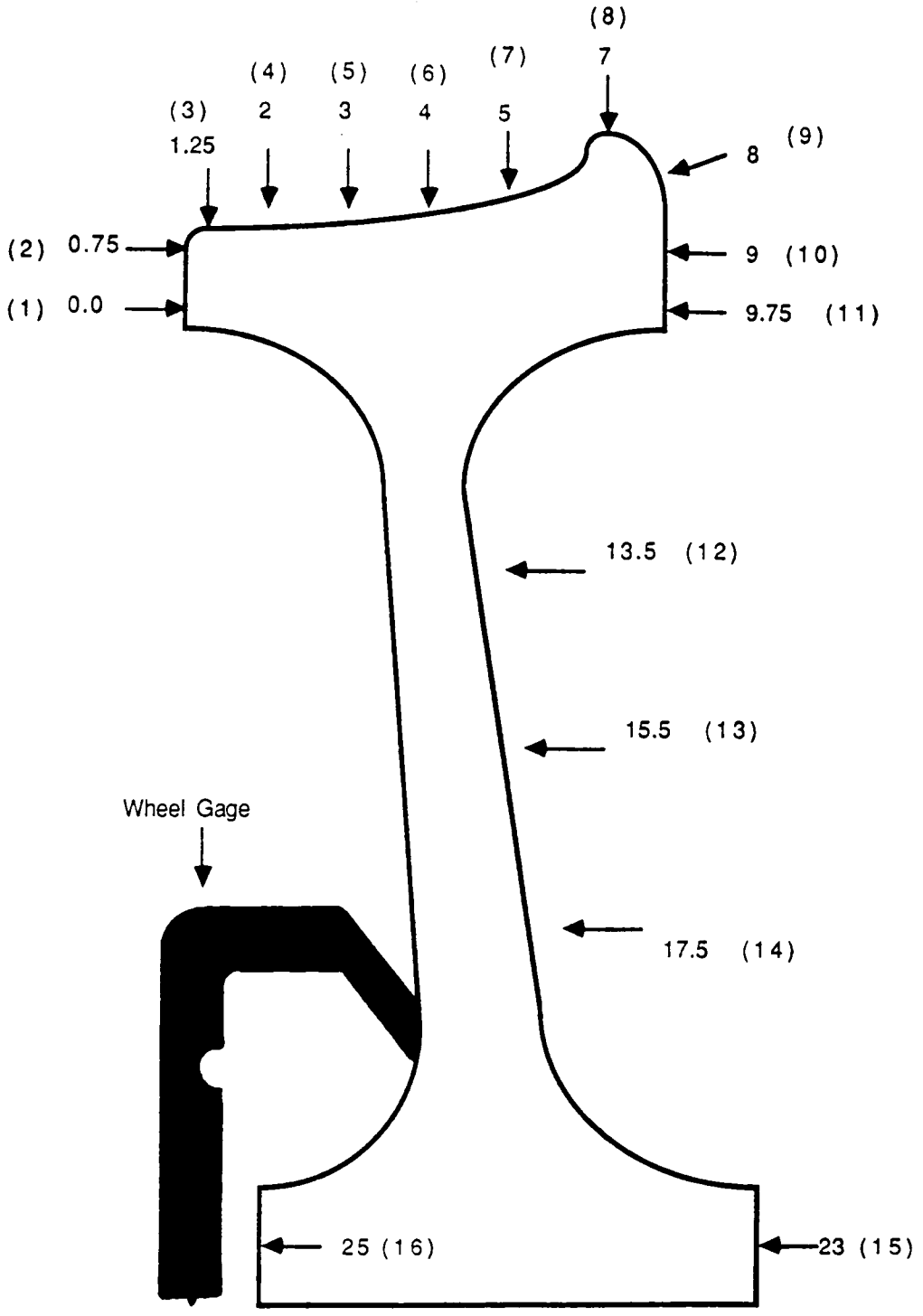

Figure 16. Positions in a flat plate wheel[2].: Numbers in parentheses represent the designation of the location on the wheel perimeter. Numbers represent the approximate distance (in inches) on the perimeter from the first measurement point.

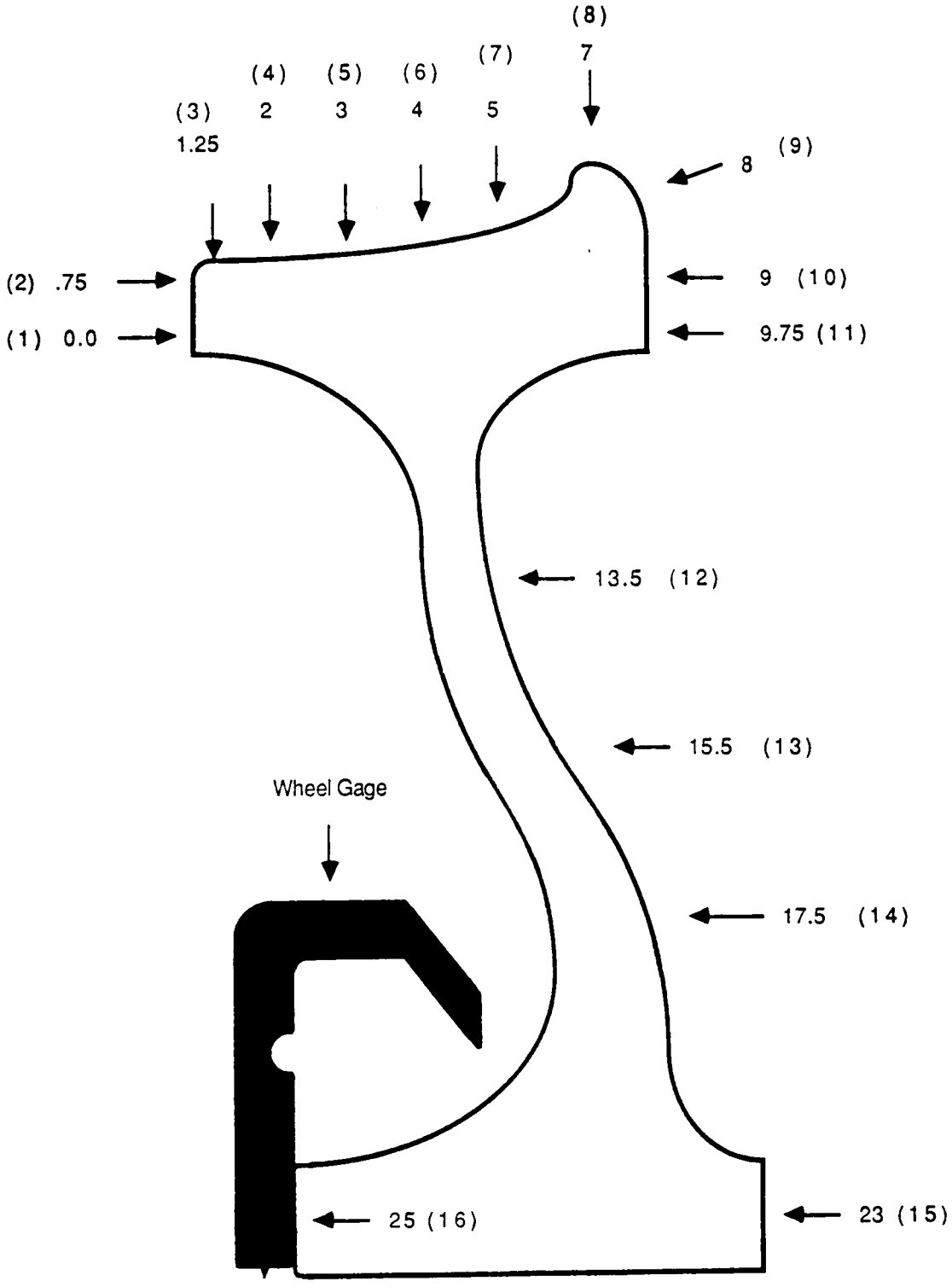

Figure 17. Positions in a curved plate wheel[2].: Numbers in parentheses represent the designation of the location on the wheel perimeter. Numbers represent the approximate distance (in inches) on the perimeter from the first measurement point.

means that only a few (preferably a single) measurements be made at a single, carefully controlled location. It is also important to determine which component of the stress tensor at this critical location -- if one can be found -- is most strongly correlated with wheel overheating. Thus, the first objective of this research was to seek such a location. Based on previous work at the AAR, the locations identified in Figure 16 were selected for measurement. These include measurements on the front rim, tread, flange, back rim, back plate, and hub. Previous work[34] indicated that these were the locations of crack initiation in many wheels failures. Measurements were made at each location at four equispaced angular positions around the wheels (0°, 90°, 180°, and 270°). Initially, residual stresses in hoop and axial directions were determined at each location. Finally, in order to fully characterize the first wheel, measurements were made at ten different, more closely spaced locations on the first wheel (Wheel A in Table 1).

It was learned very early in the research that the radial and axial components of the stress tensor for the wheel were uninteresting. It was only the circumferential or hoop stresses which appeared to contain the information sought. Thus, in the following section, only normal and shear stresses in this direction are reported. Furthermore, after careful examination of the first wheel (Wheel A) it was found that the data showed cylindrical symmetry. Therefore the measurement program of the remaining wheels was, in the interest of time, reduced to acquire data only at the 0° and 90° positions. Because of the possibility of the measurements on the heat-discolored wheels showing fluctuation of stress, or hot zones, in the range of 90 to 120 degrees, measurements were made at the four intervals of 90° for determination of critical points.

After the critical point in the axial direction was found using the likelihood statistics, the sixteen orhtogonal azimuthal positions around the wheel at the critical point were chosen in intervals of 22.5 degrees, as shown in Figure 18. The azimuthal stress data from the six wheels were used for discrimination of good and bad wheels using the variance statistics and, as was noted in Section 2, gives a clue to identify a wheel with hot zone.

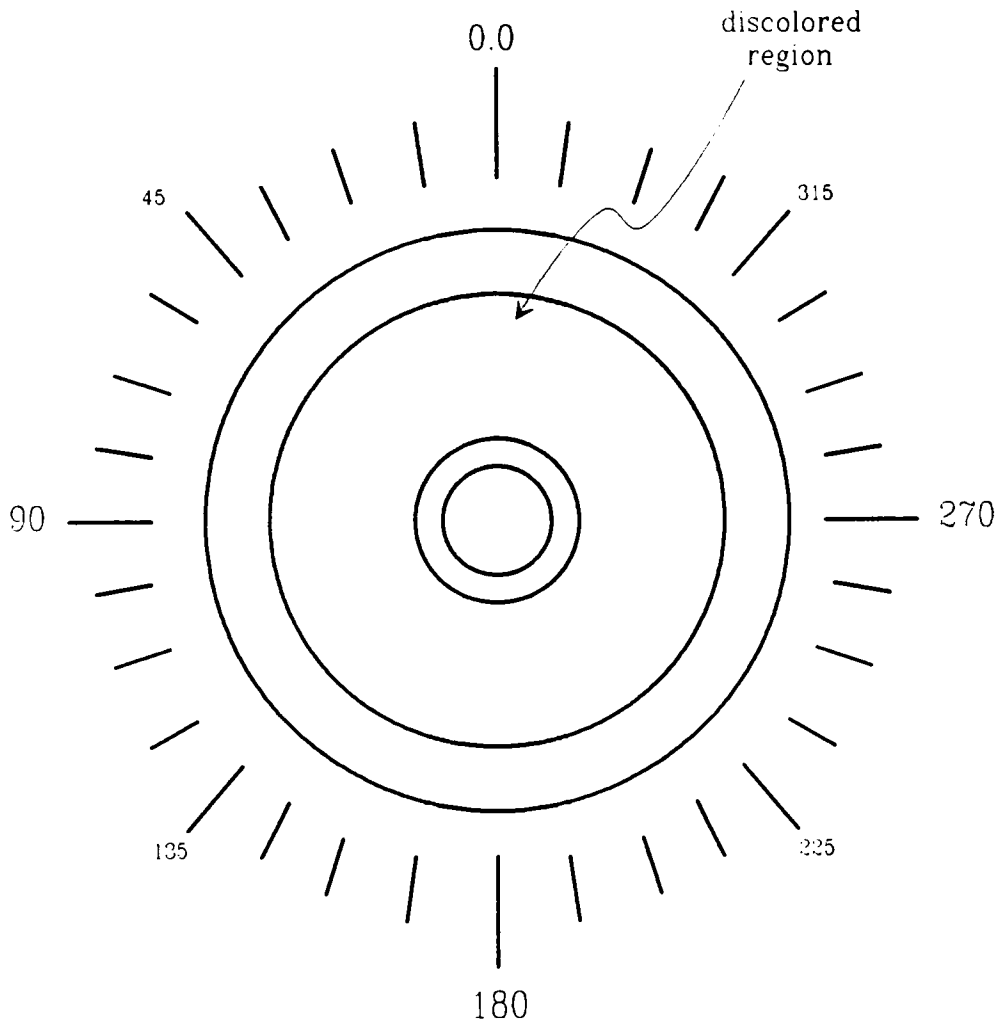

Figure 18. Sixteen angular positions in the tread of wheel.

4.2 RESULTS

The objective of the work performed on the first wheel was to characterize a flat plate wheel, a normal wear wheel, and a heat-discolored (less than 4") wheel, as fully as possible. The results of this study are reported in Section 4.2.1. Section 4.2.2 introduces the intercomparison between the drilling and x-ray residual stress measurement and also explains the variation of the residual stress in depth.

4.2.1 X-ray Residual Stresses

A straight plate wheel with normal wear (Wheel A) was used for the initial studies. Stress measurements were made in the circumferential (hoop) direction at ten different locations across the tread width at each of four rotational positions (indicated as 0, 90, 180, 270 degrees from an arbitrary starting position). Typical plots of lattice spacing, d, versus diffractometer tilt angle, ψ, are shown in Figures 6 and 7. It will be noted that the curve shown in Figure 7 is split, with data for negative ψ and positive ψ angles following different curves. This is a very significant observation. It indicates either a non-zero shear stress in the plane perpendicular to the wheel axis or a misalignment of the instrument. Because of the difficulties associated with precision alignment of the diffractometer on a railroad wheel, particular care was taken to verify that the observed split is real and not an experimental artifact. It was determined that the observed split can be reliably interpreted as arising from shear stresses in the wheel. With this assurance the data for each measurement location was fitted by a least squares multiple regression model to obtain both the normal and shear stresses in the hoop direction. A plot of the normal stresses at each location is shown in Figure 19, and a plot of the shear stress is shown in Figure 20. In these figures the mean stress and the 1σ error bars of the measurements are both shown. The standard deviations of each

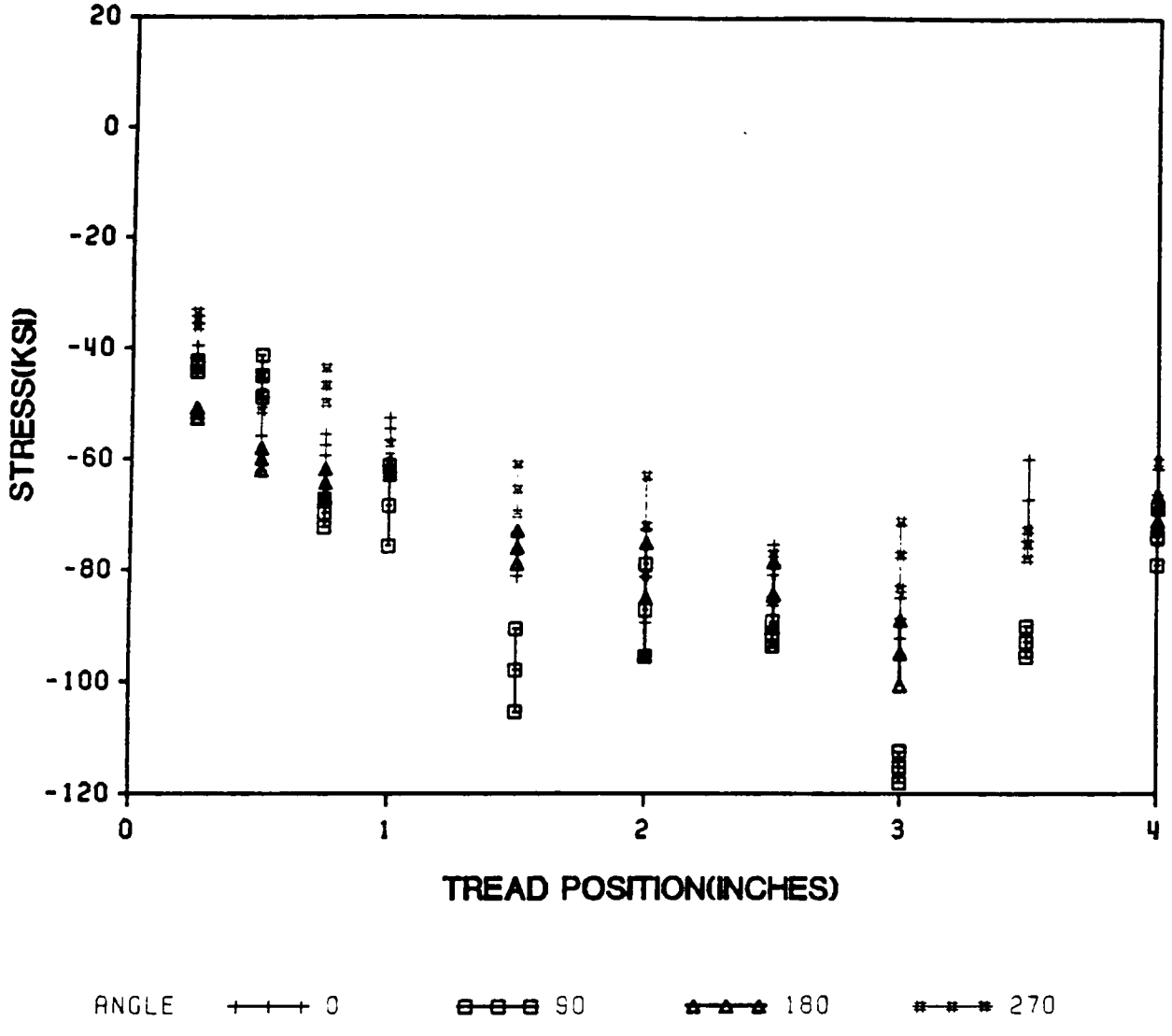

Figure 19. Circumferential normal stresses in the tread of Wheel A at four different wheel rotations: as a function of distance from the rim.

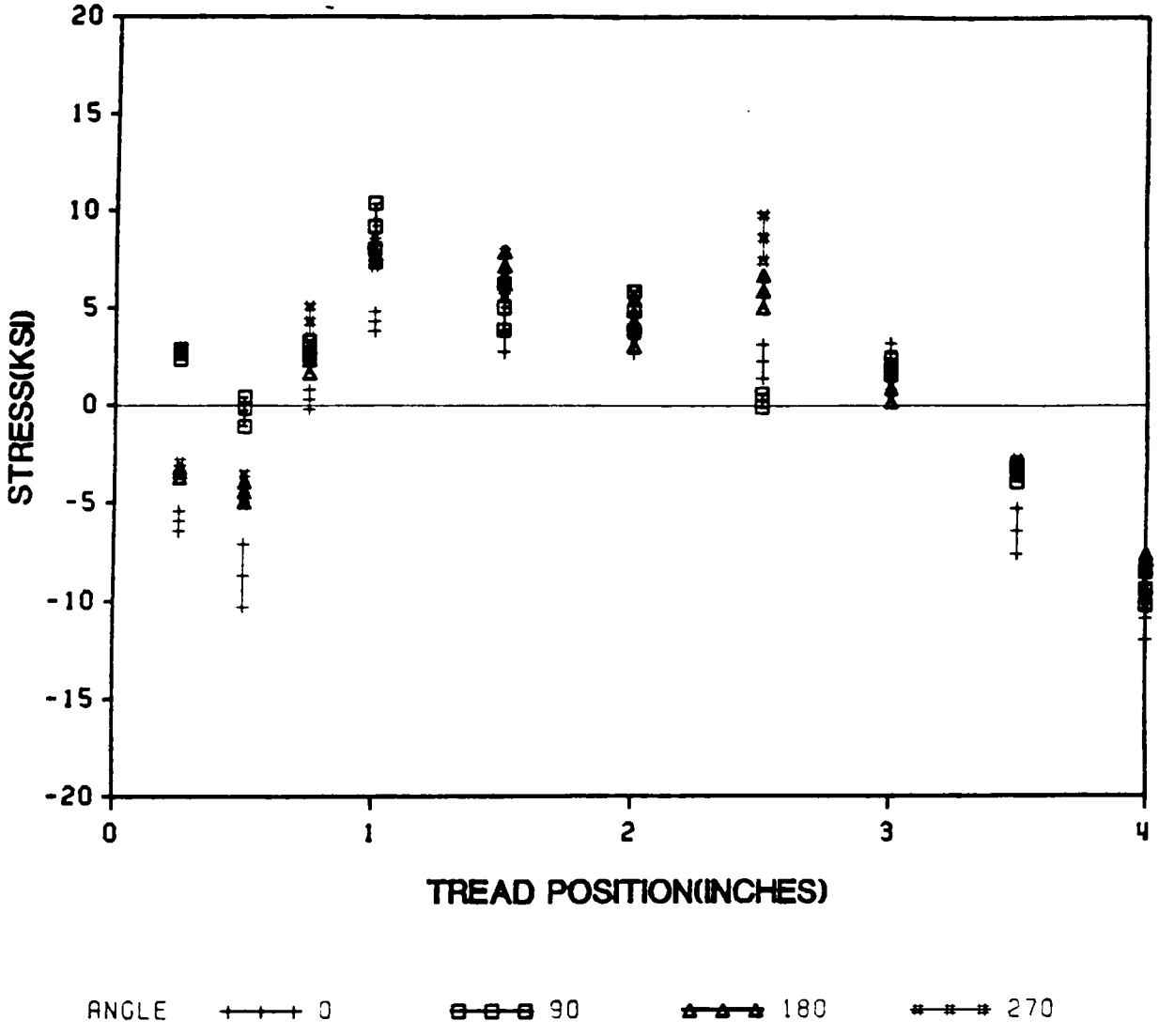

Figure 20. Circumferential shear stresses in the tread of Wheel A at four different wheel rotations: as a function of distance from the rim.

measurement are estimated to be approximately ± 2.5 ksi for the normal stresses and ± 0.5 ksi for the shear stresses.

Several important conclusions can be drawn from these results. First, although the variation of both the normal and shear stresses at the various wheel angles in wheels exceeds the estimated 1σ value for each measurement by approximately a factor of 5, the data are still remarkably uniform at each position on the tread as the wheel is rotated about its axis. This degree of symmetry was maintained when the measurements were extended to include the other points on the front rim, flange, back rim, plate and hub. These data show no evidence of significant hot zones which would be expected to produce major deviations from cylindrical symmetry. Second, from Figure 19 it can be seen that the normal (hoop) stress is larger and compressive, varying from about -50 ksi at the front rim corner of the tread to about -90 ksi towards the flange. There is clearly a maximum compressive stress about 3 inches on the tread from the front rim corner. Finally, it is seen from Figure 20 that the shear stresses are small (-10 ksi to + 10 ksi) and that in the center of the tread they are of opposite sign to the shear stresses near the rim or the flange. This is a very unusual result, and a great deal of effort was expended to verify that the analysis was valid. Based on a preliminary analysis of the errors in the stresses, and from the reproducibility of the data both at a given location and as a function of wheel rotation, we are confident that the error bars on these data points are approximately $\pm$ 0.5 ksi, and the results are valid.

Based on these data it was concluded that, within the accuracy required for the measurements, this wheel (Wheel A) was cylindrically symmetric (As will be seen in Section 5.2, the data from the heat-discolored (more than 4") curved wheel shows significant deviations from azimuthal symmetry.). Thus, in the interest of time it was decided that for all further work, unless larger variations of the data than observed here were found only two measurements (0 and 90°) would be made on each wheel for the likelihood statistical analysis to be described in the next chapter.

Measurements were also made at most of the sixteen axial locations for at least two (0 and 90°), and often more, azimuthal rotations on the six wheels (A through F) for the variance statistical analysis. The data were analyzed as before to recover both the normal and shear components in the hoop direction. Complete results are presented in Appendix B.

Graphical representations of the x-ray normal and shear residual stress data of the six wheels are shown in Figures 21 through 32. In these figures, the data are plotted on a radial cross section of the wheel to show the values and the locations from which they come. Based on the initial likelihood statistical analysis described in the next chapter, a few locations on the wheel were identified as being most sensitive to changes in residual stress as a function of service history. One of the locations, location 5, was in the center of the tread. At this critical point the x-ray stresses were measured in azimuthal intervals of 22.5 degrees around each wheel. The azimuthal distribution of the x-ray stresses at this key location is shown in Figures 33 through 38. In all of these figures (21-38), the magnitude of either the normal stress or the shear stress in each wheel is plotted as a vertical distance from the surface of the wheel at the measurement location. The shaded bands represent the interpolated stresses at the surface of the wheels. Compressive normal stresses are represented outside the wheel, while tensile stresses are inside. A ruler at several locations around wheel aids to visually estimate the magnitude of the stresses.

It is important to note that both heat-discolored wheels (Wheels B and E) showed grooves in the tread. Sketches of the locations and magnitudes of these grooves are shown in Figure 39. The grooves are made by friction, wear, and spalling in the instantaneous contact area between the brake shoe and the wheel. The position of brakes on the tread of two wheels is shown in Figure 40. The brake shoe contact with the tread does not exceed 50 percent of the area of the shoe face[82], whose width is about the same as the tread and whose height may be as little as several thousandths of an inch higher than neighboring regions on the tread or on the brake shoe.[76] This uneven brake shoe contact and the worn out brake pad are believed to be the cause of the grooves in the tread, as shown in Figure 39.

The approximate stress measurement locations are also shown in Figure 39. Note that location 6, which is approximately 3 inches from the rim, is inside both grooves. Because of the surface roughness effects inside the grooves, it was sometimes necessary to shift the measurement location by a fraction of an inch to either side of the normal location. Figures 29 and 31 clearly show that the groove is a boundary to reverse the sign of the stress. This may be because either thermal cycling,[76] different thermal expansions between two regions,[31] or both processes take place.

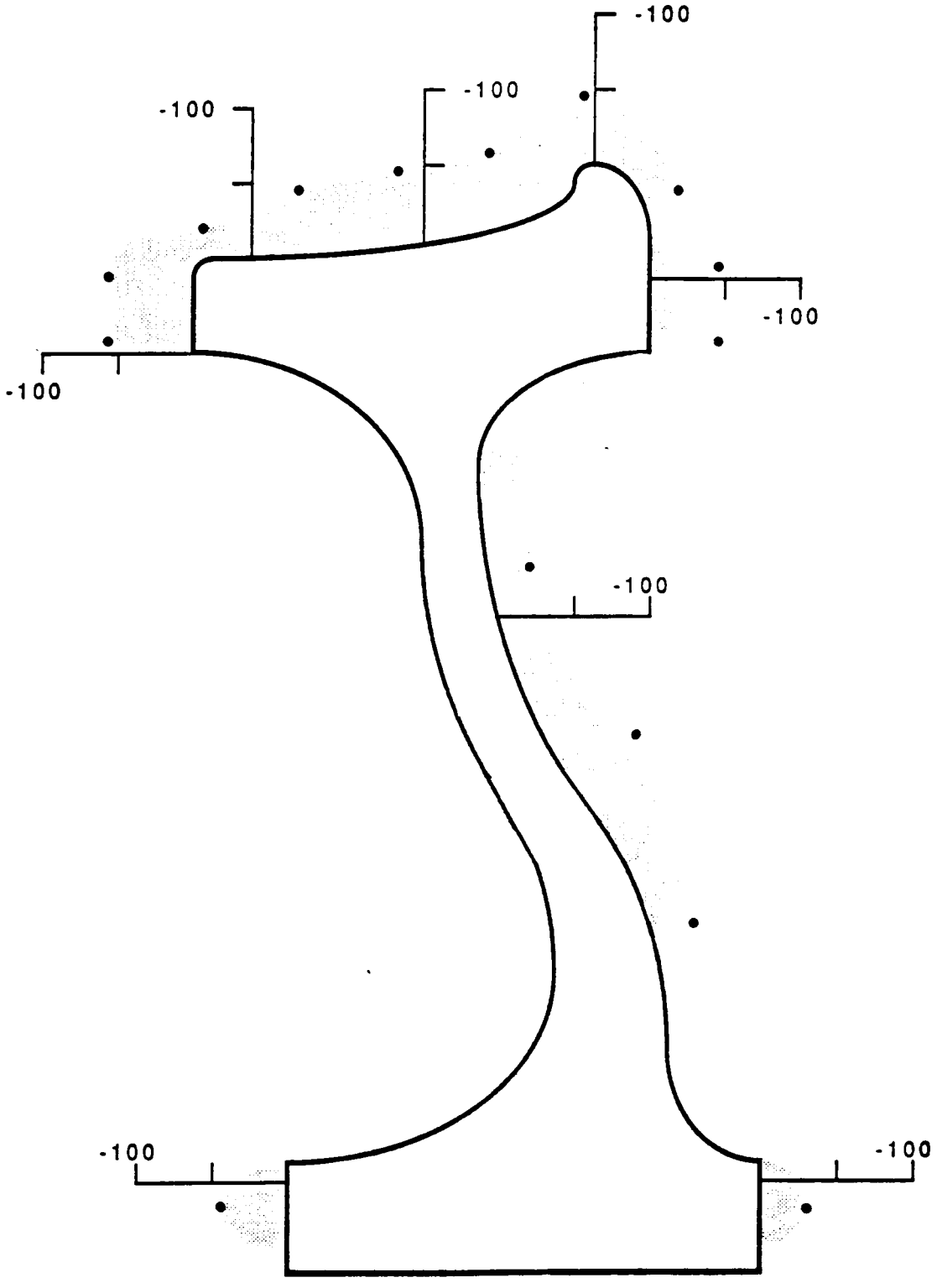

Figure 21. Normal stresses in axial direction in cross view of a new, curved plate wheel (Wheel D).

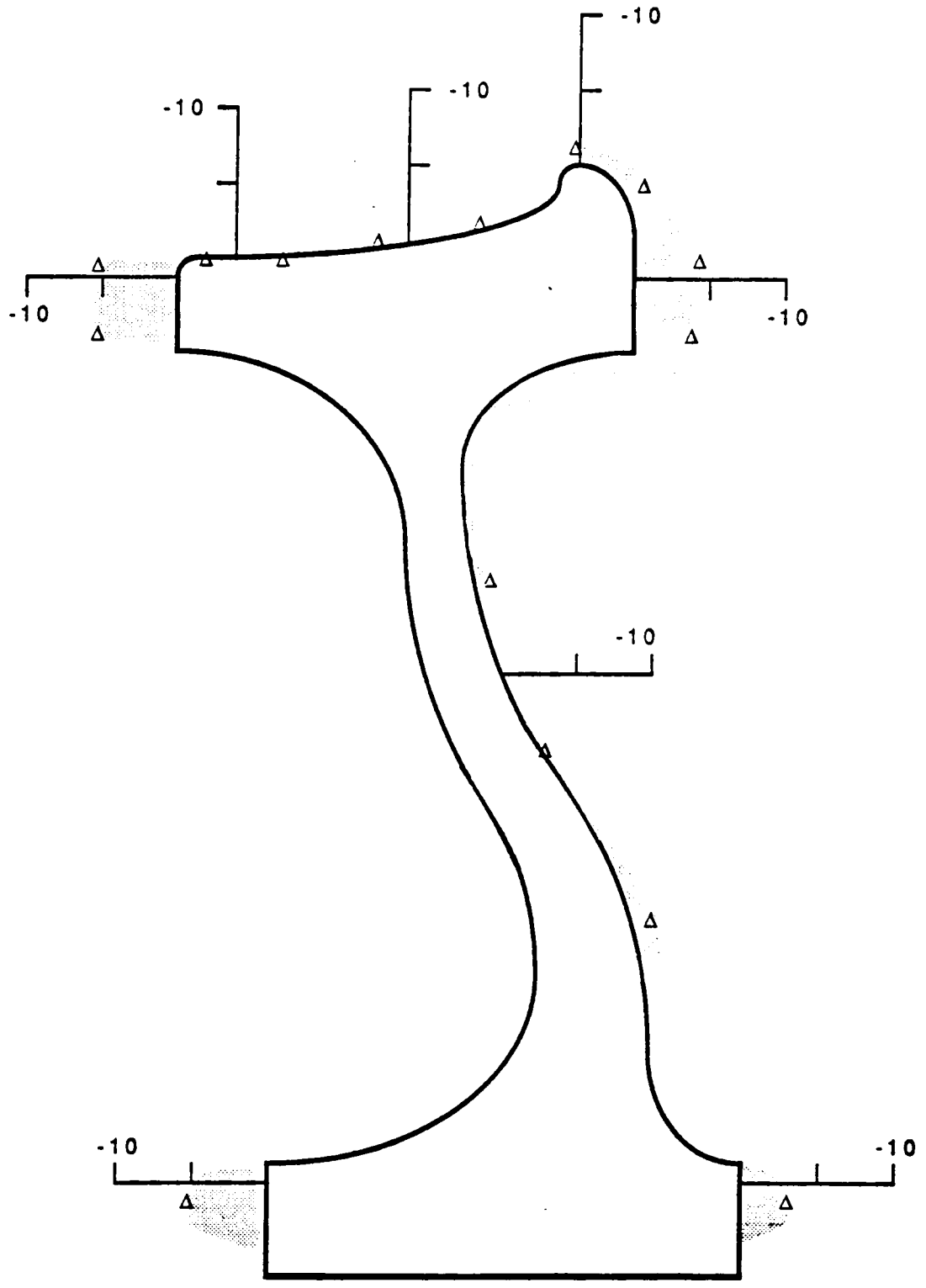

Figure 22. Shear stresses in axial direction in cross view of a new, curved plate wheel (Wheel D).

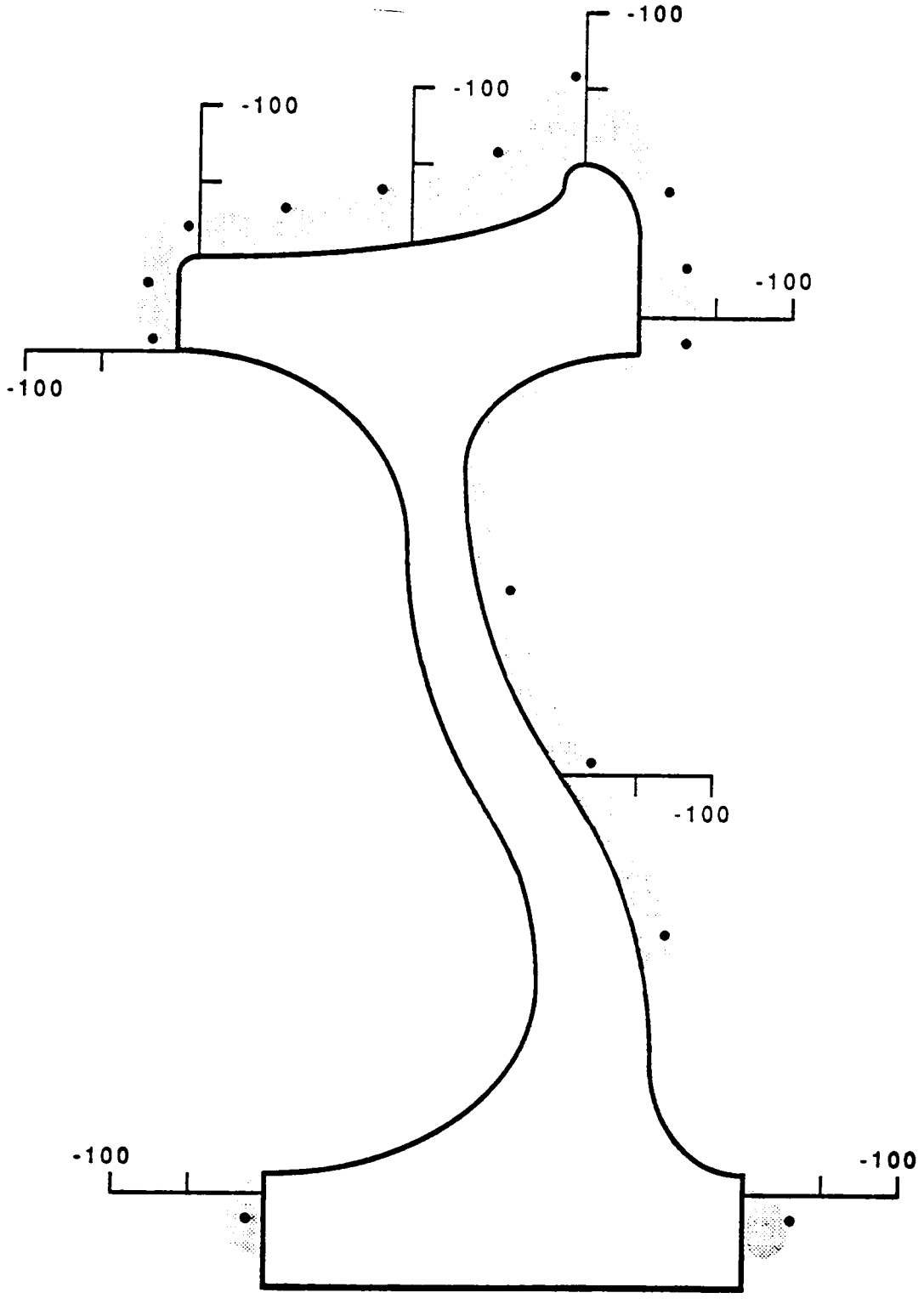

Figure 23. Normal stresses in axial direction in cross view of a new, misfit curved plate wheel. (Wheel C)

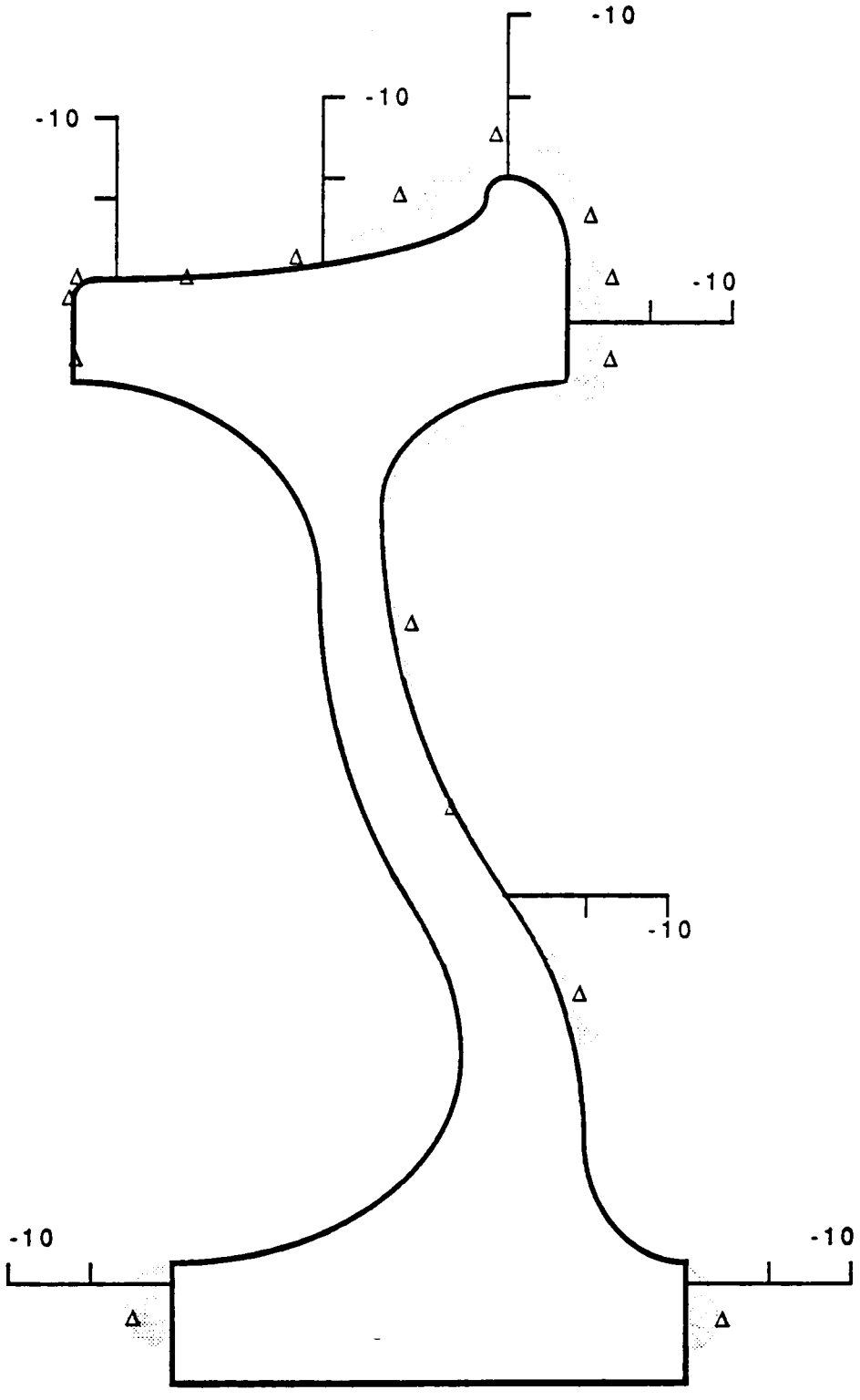

Figure 24. Shear stresses in axial direction in cross view of a new, misfit curved plate wheel. (Wheel C)

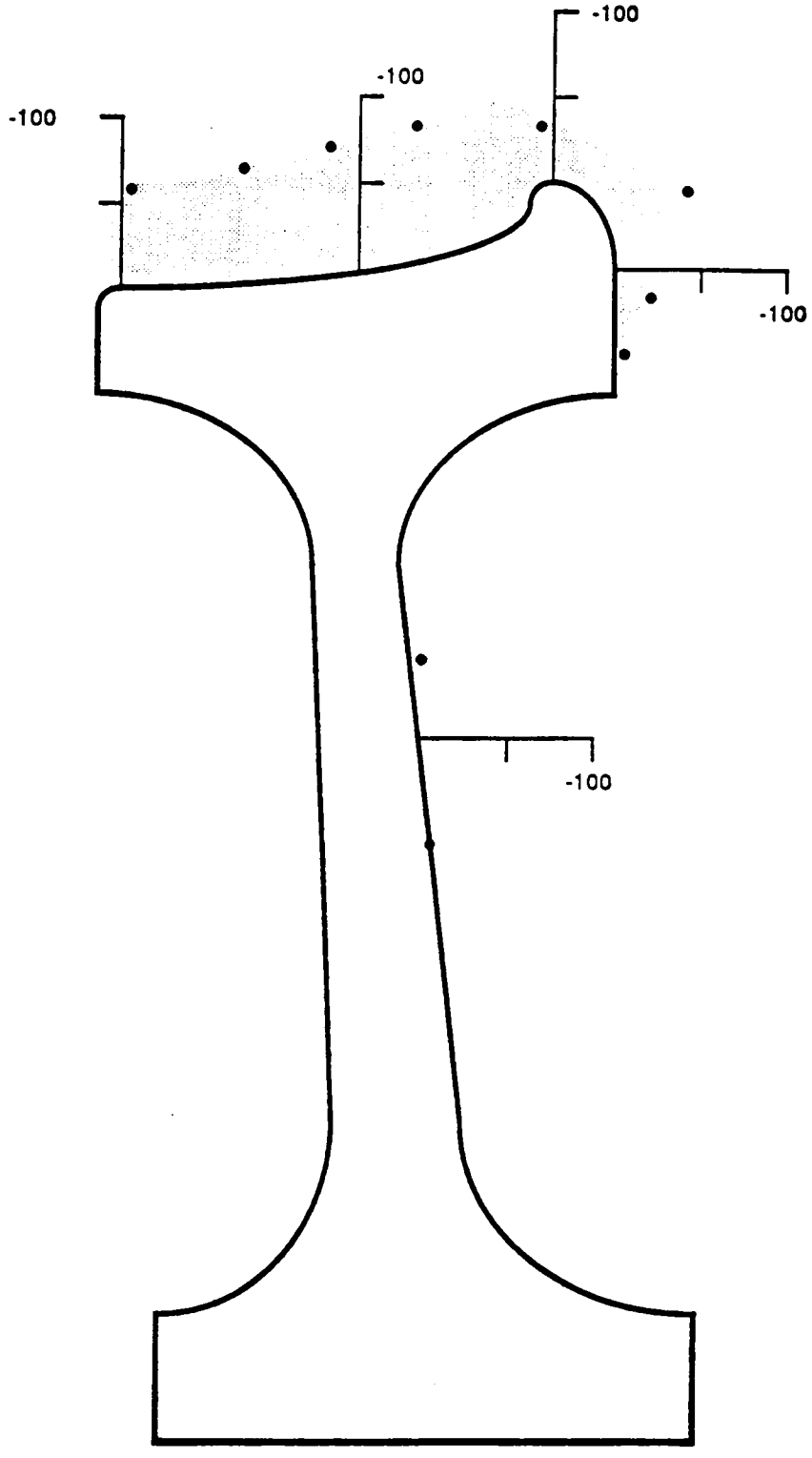

Figure 25. Normal stresses in axial direction in cross view of wrought, normal flat plate wheel (Wheel A)

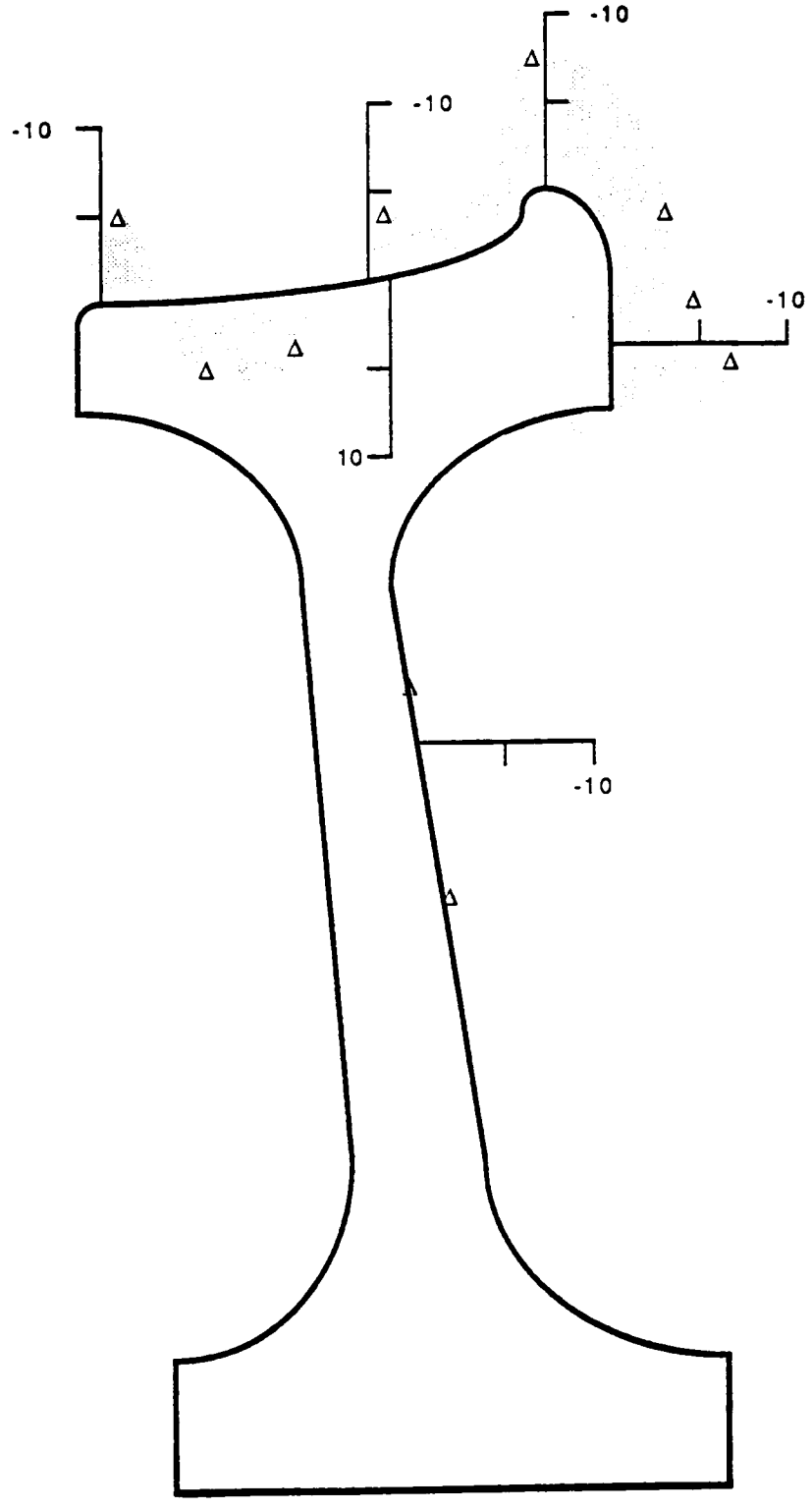

Figure 26. Shear stresses in axial direction in cross view of wrought, normal flat plate wheel (Wheel A)

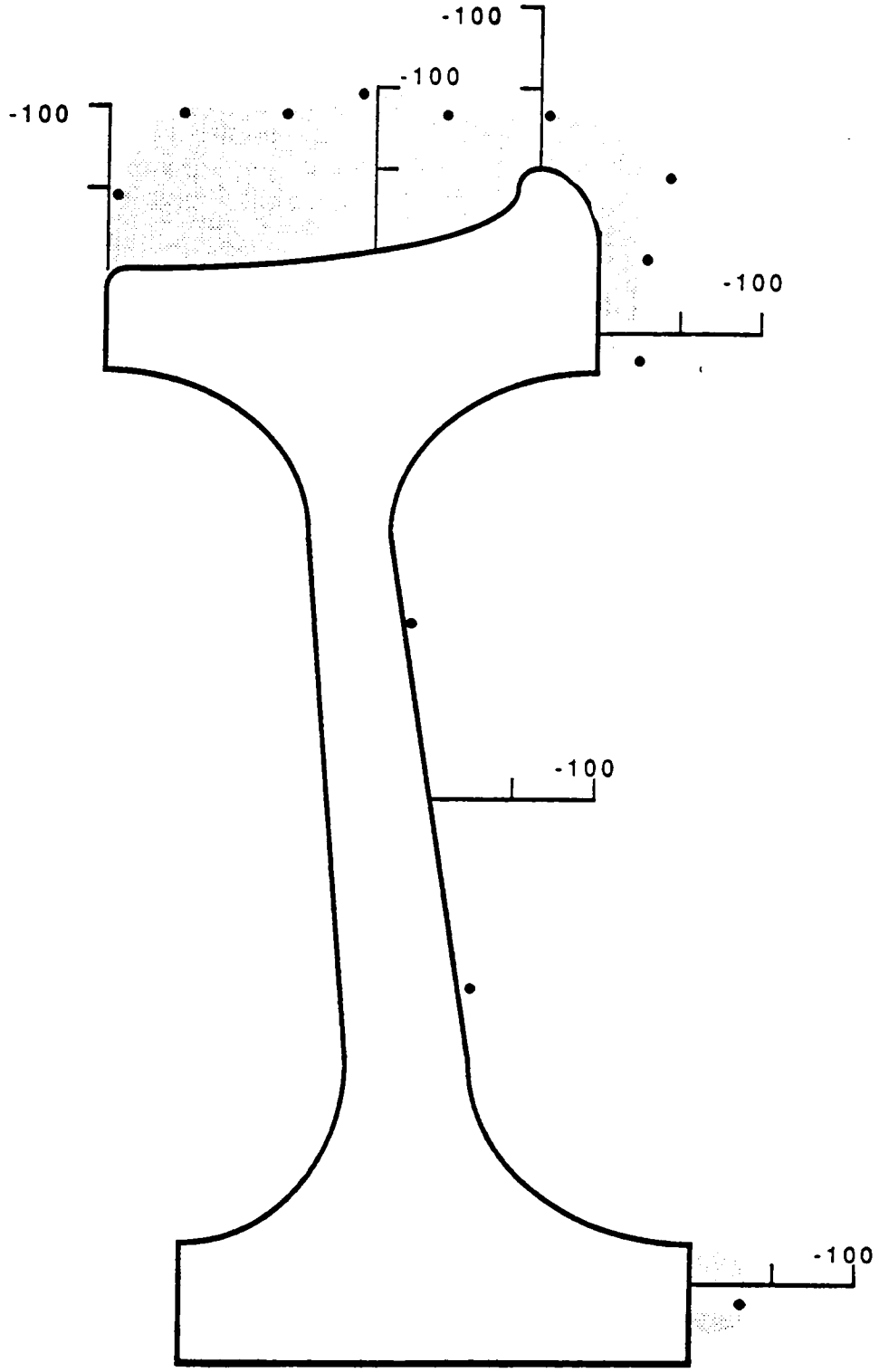

Figure 27. Normal stresses in axial direction in cross view of a cast, normal wear, flat plate wheel (Wheel F).

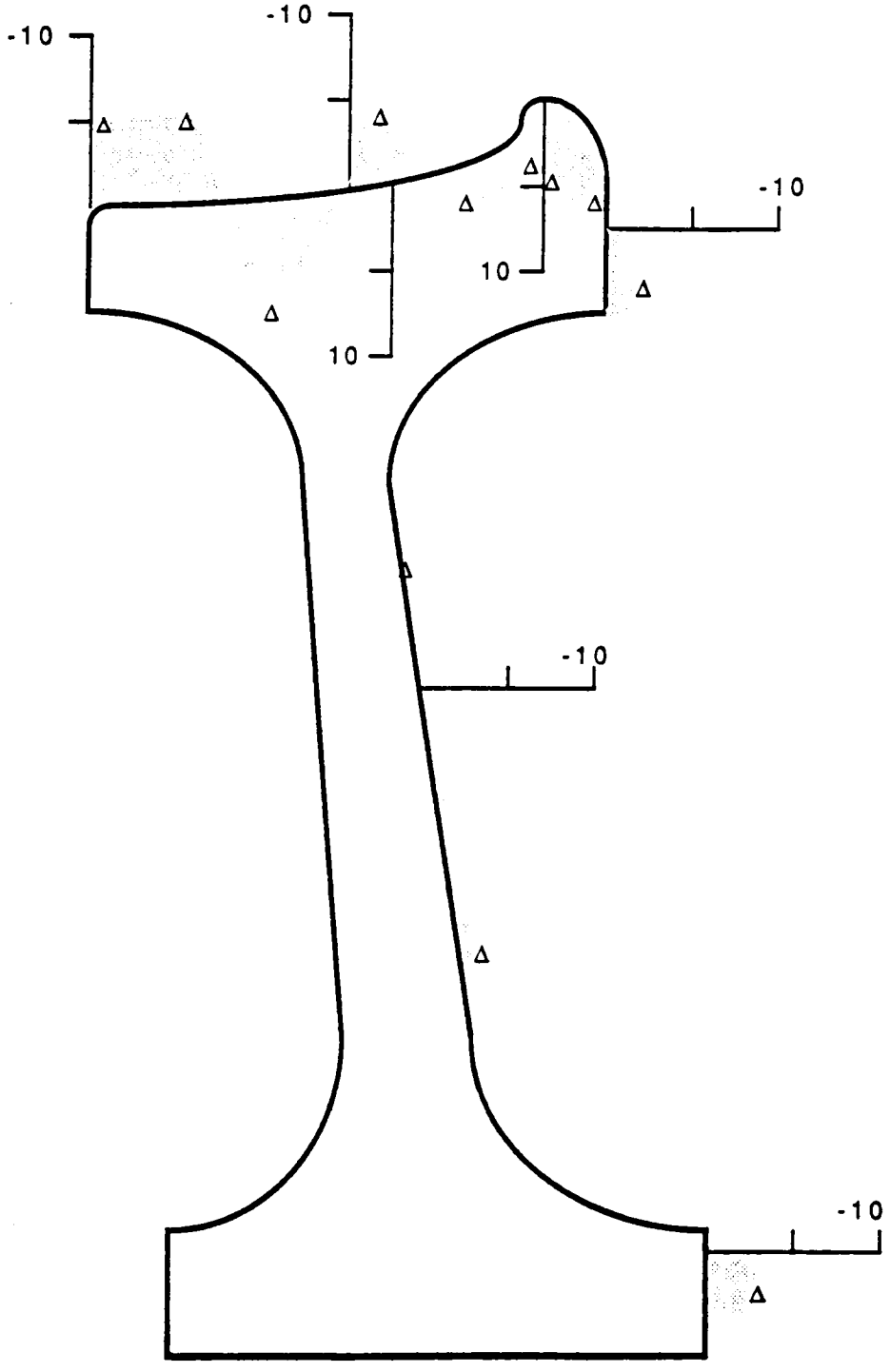

Figure 28. Shear stresses in axial direction in cross view of a cast, normal wear, flat plate wheel (Wheel F).

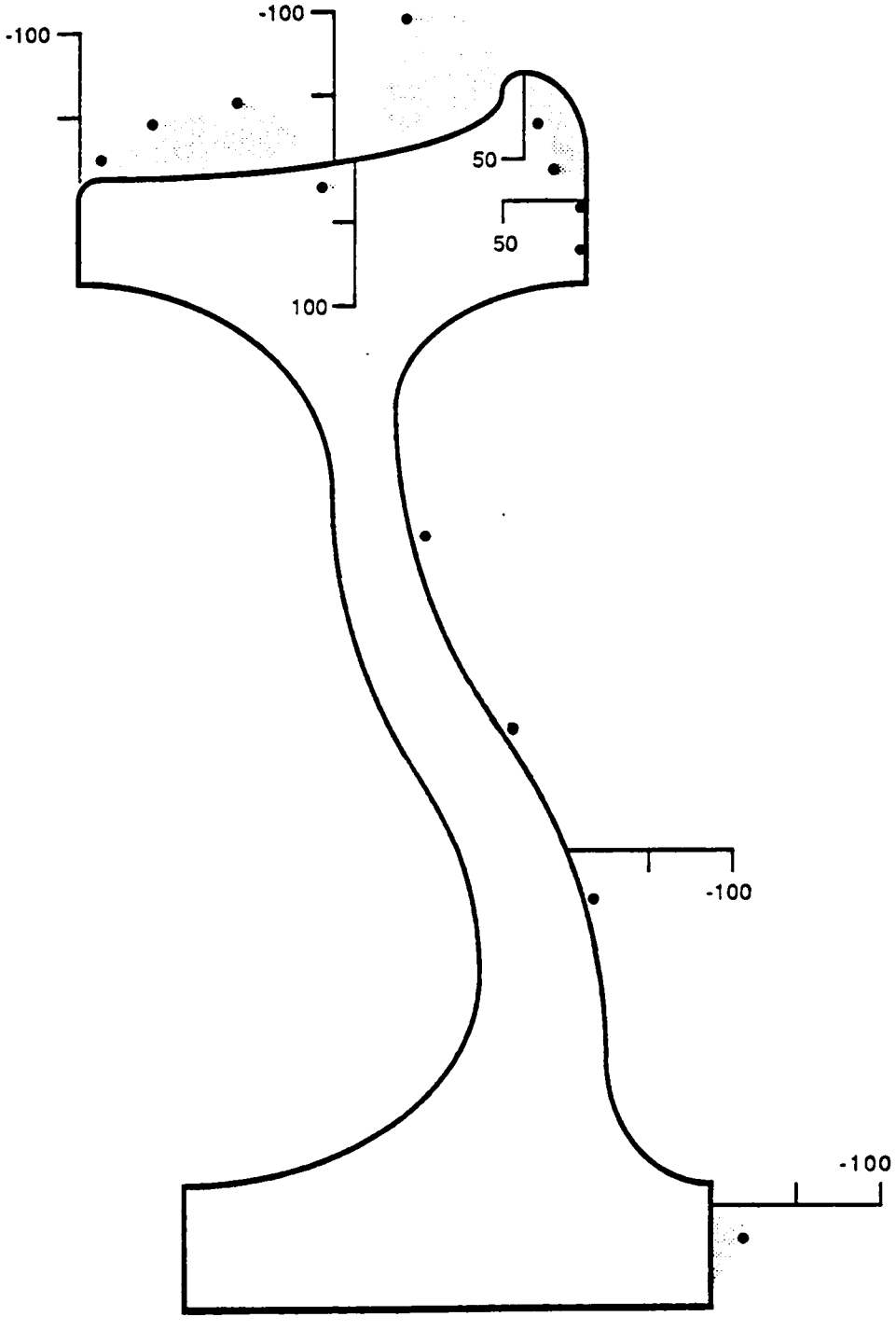

Figure 29. Normal stresses in axial direction in a heat-discolored (less than 4") severly grooved curved-plate wheel (Wheel B).

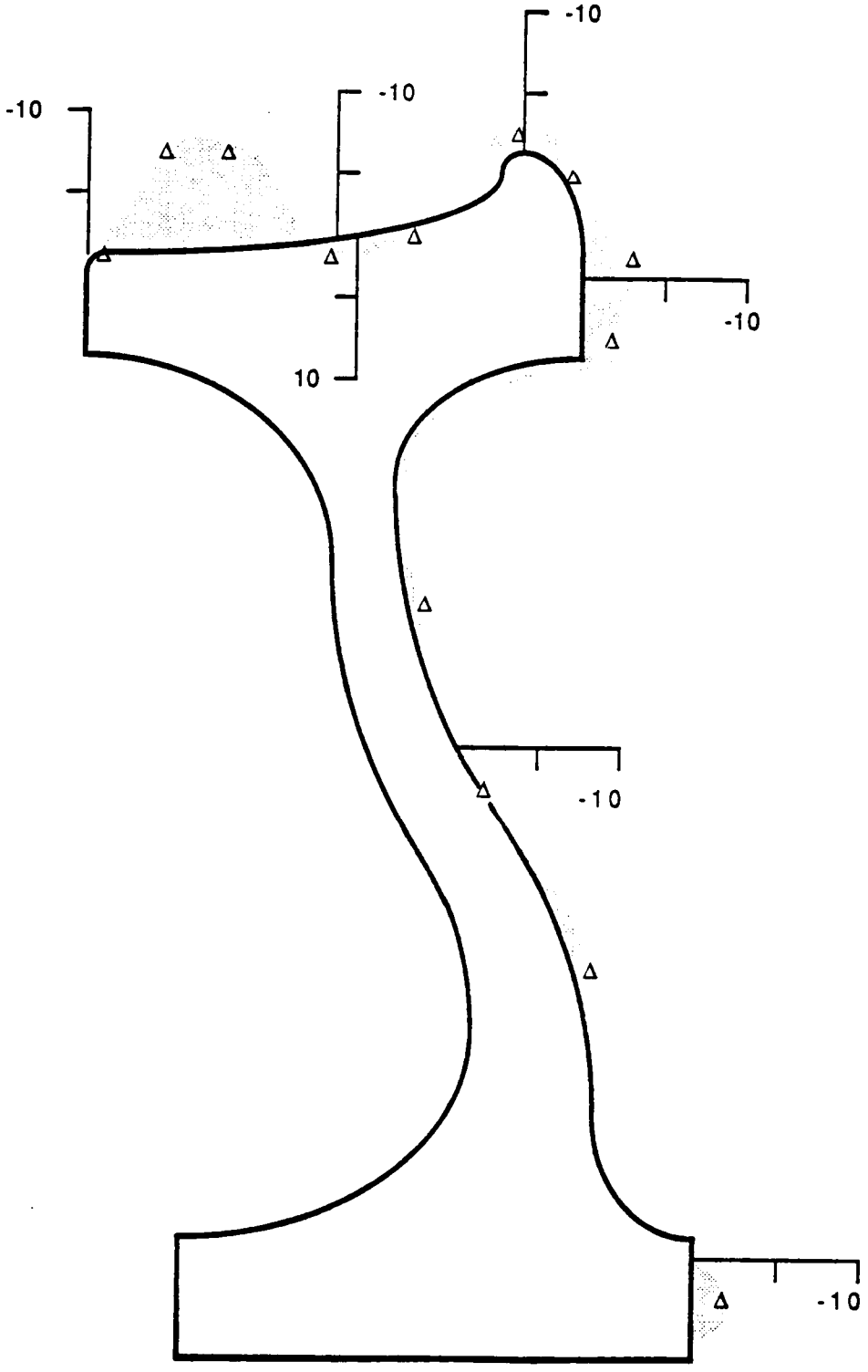

Figure 30. Shear stresses in axial direction in a heat-discolored (less than 4") severly grooved curved-plate wheel (Wheel B).

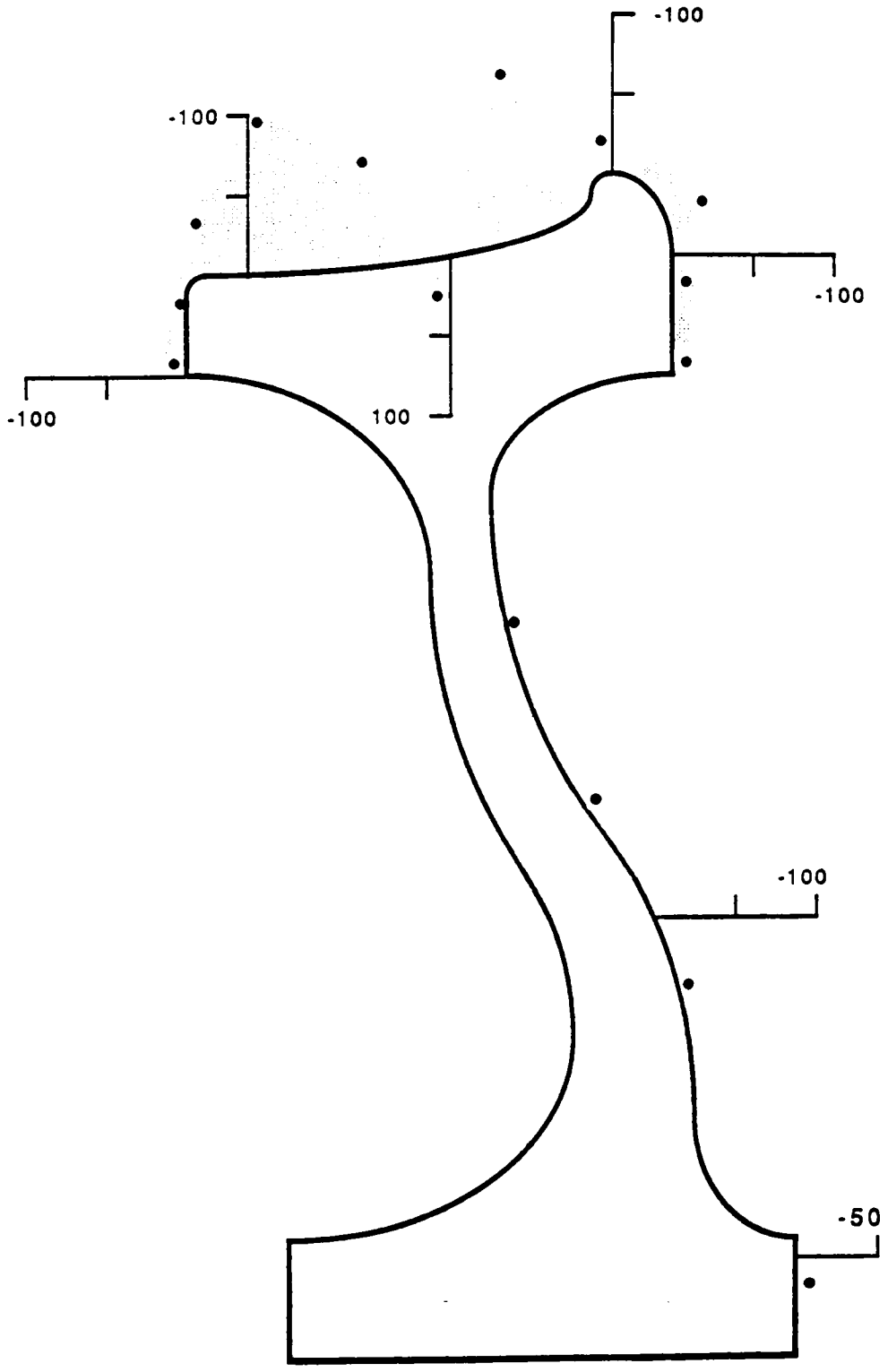

Figure 31. Normal stresses in axial direction in cross view of a heat-discolored (more than 4") curved-plate wheel (Wheel E).

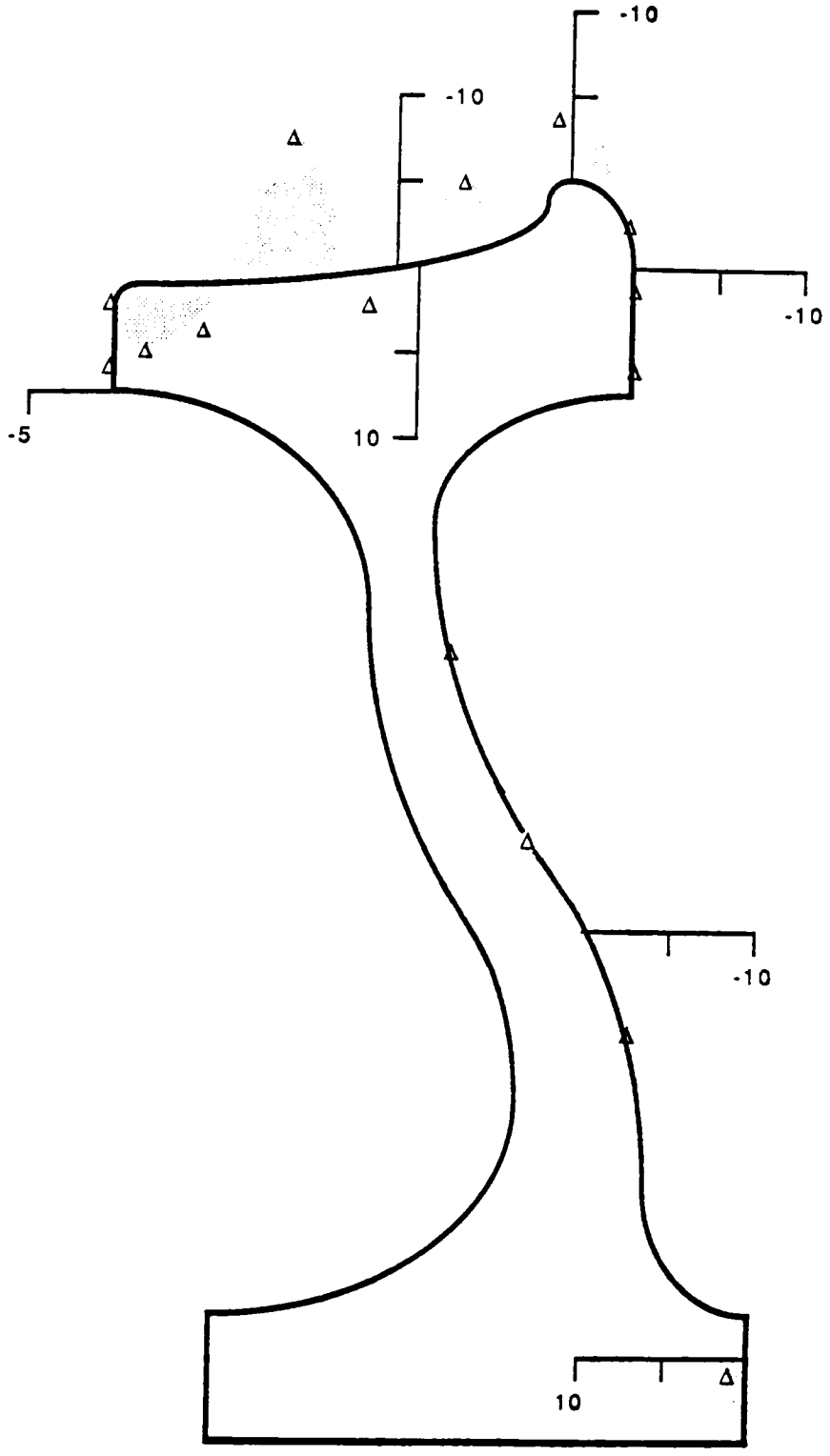

Figure 32. Shear stresses in axial direction in cross view of a heat-discolored (more than 4") curved-plate wheel (Wheel E).

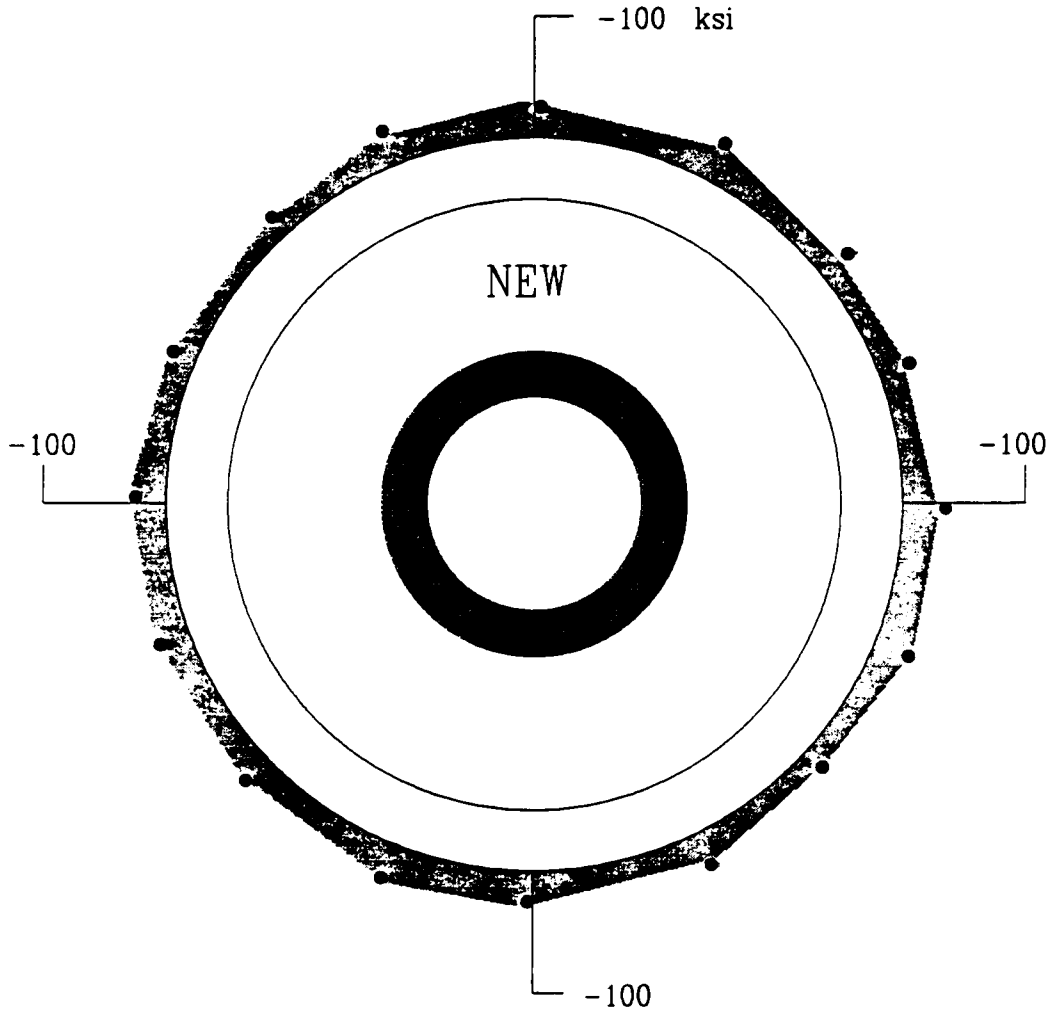

Figure 33. Normal stresses in azimuthal direction in side view of a new, curved plate wheel (Wheel D).

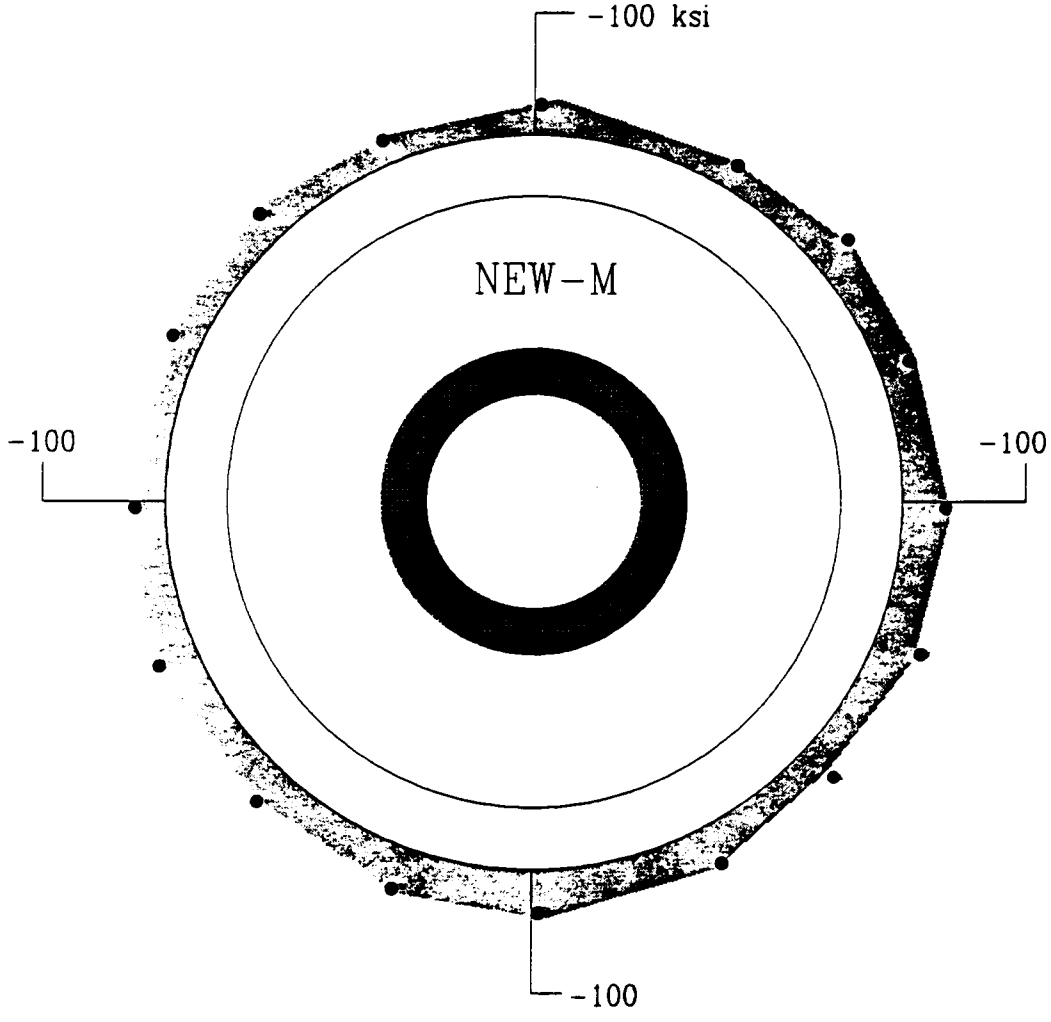

Figure 34. Normal stresses in azimuthal direction in side view of a new, misfit curved flat plate wheel. (Wheel C)

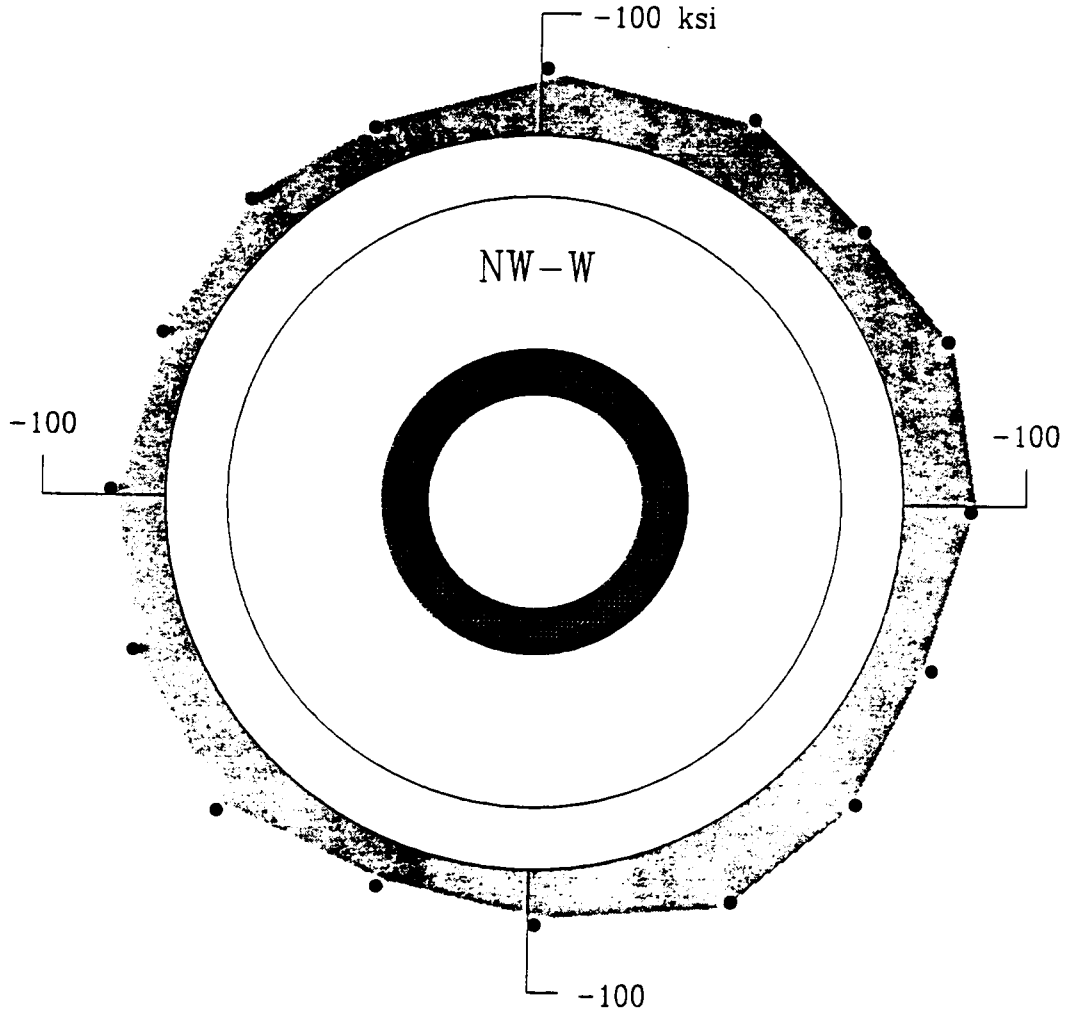

Figure 35. Normal stresses in azimuthal direction in side view of wrought, normal flat plate wheel (Wheel A)

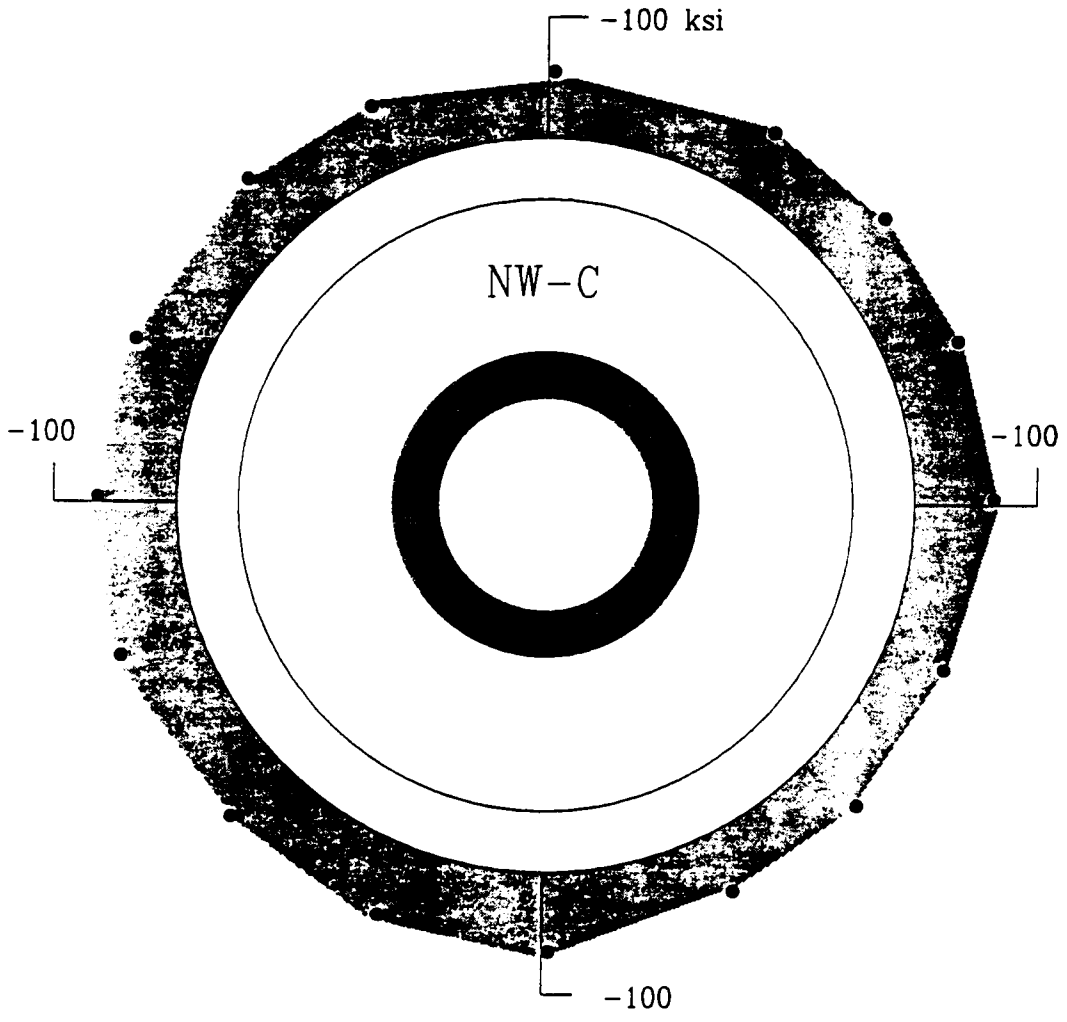

Figure 36. Normal stresses in azimuthal direction in side view of a cast, normal wear, flat plate wheel (Wheel F).

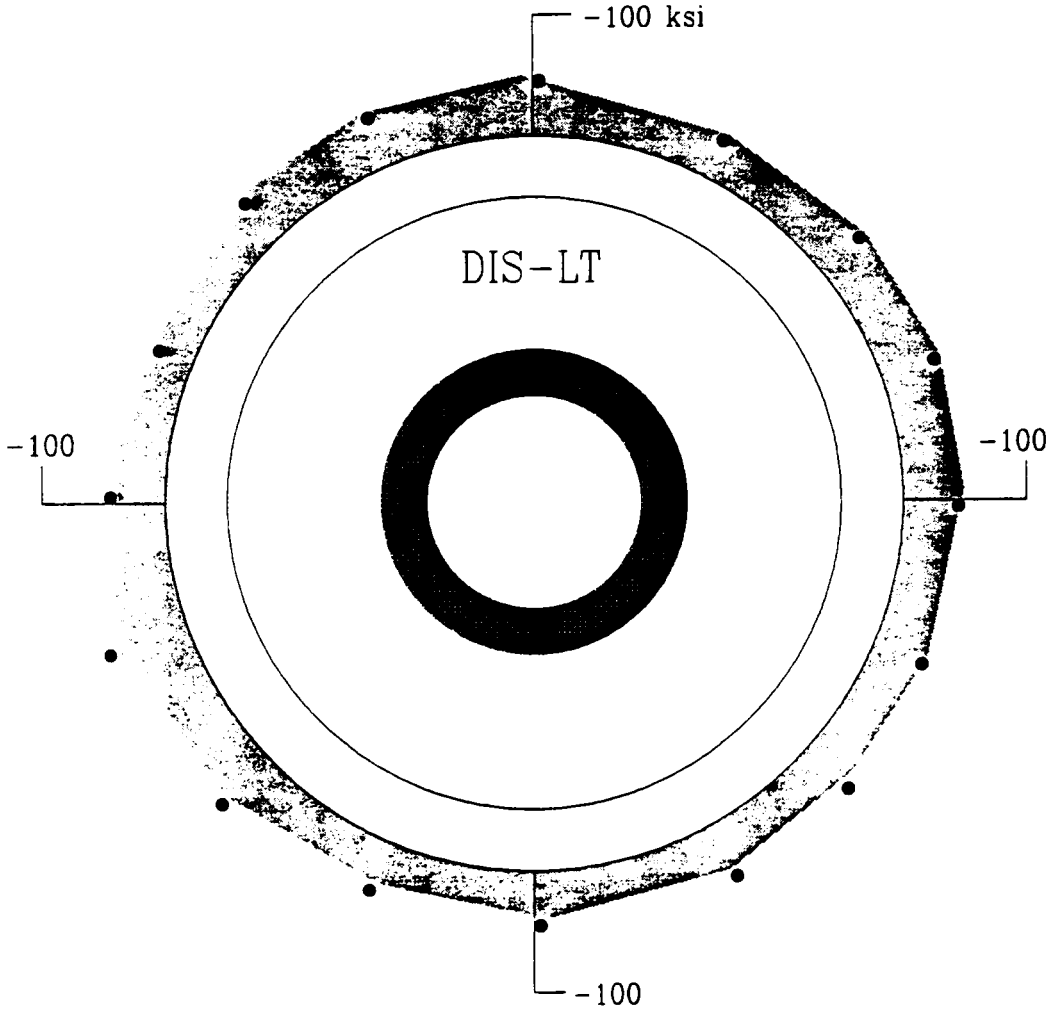

Figure 37. Normal stresses in azimuthal direction in a heat discolored (less than 4") severly grooved curved plate wheel (Wheel B).

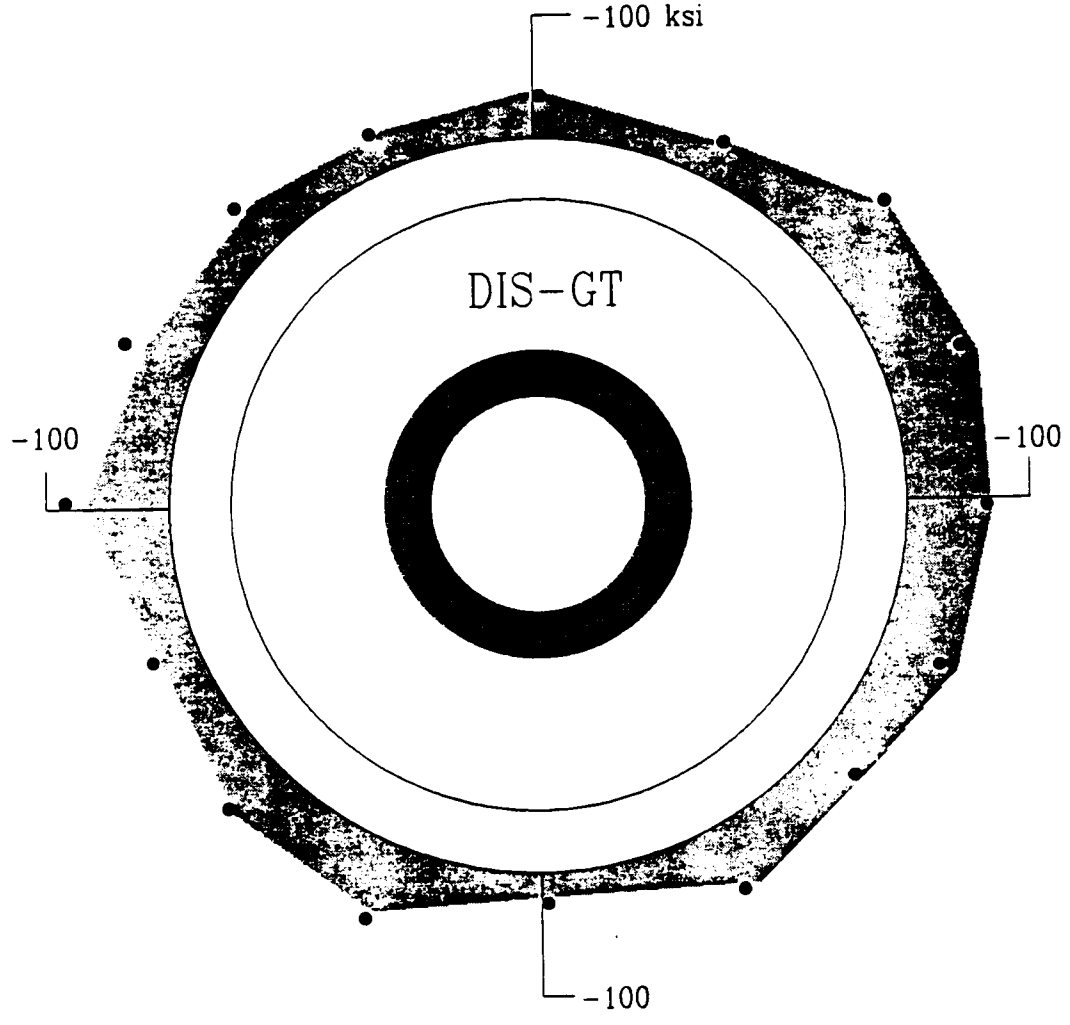

Figure 38. Normal stresses in azimuthal direction in side view of a heat discolored (more than 4") curved plate wheel (Wheel E).

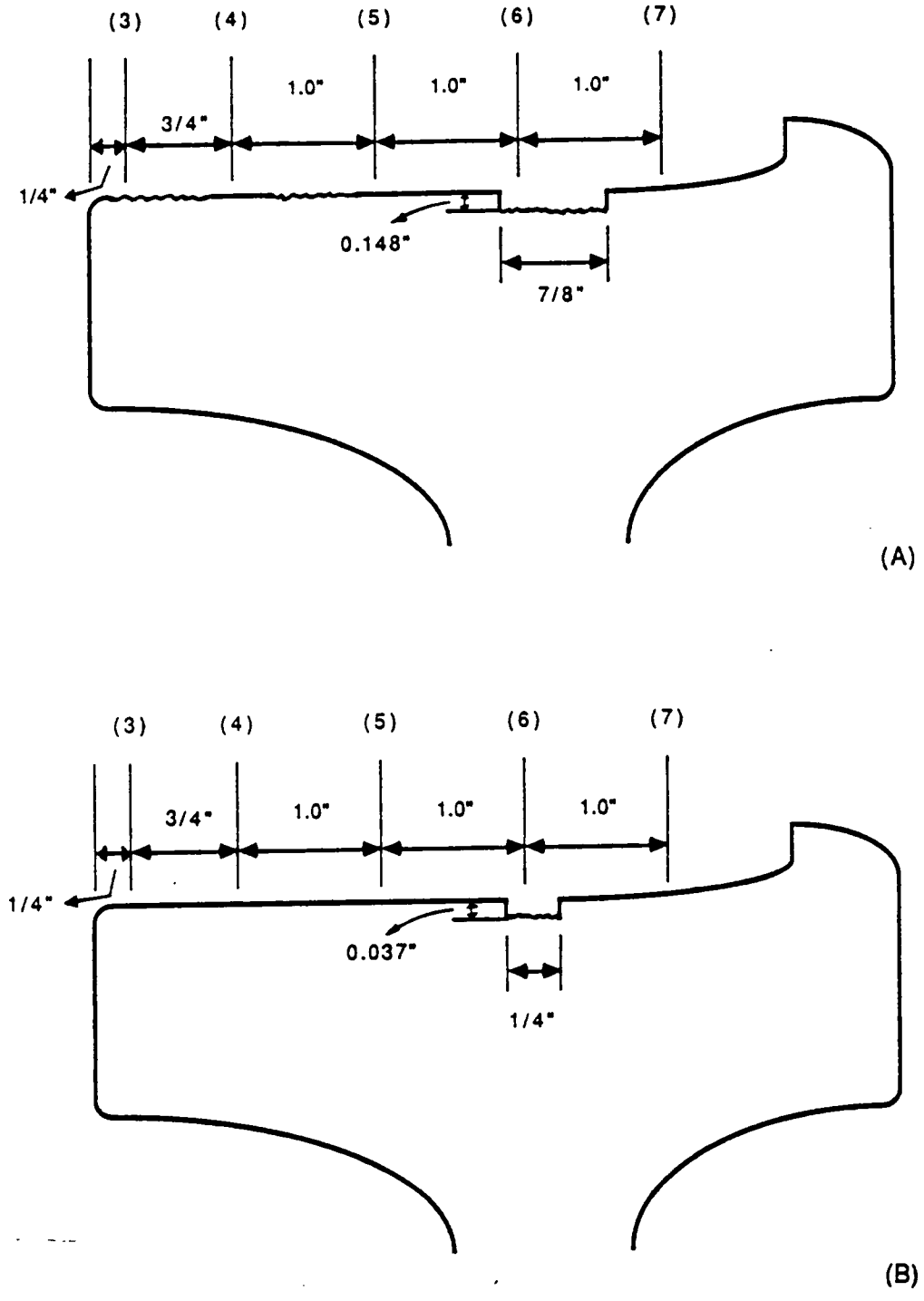

Figure 39. Grooves on the treads of the discolored wheels.

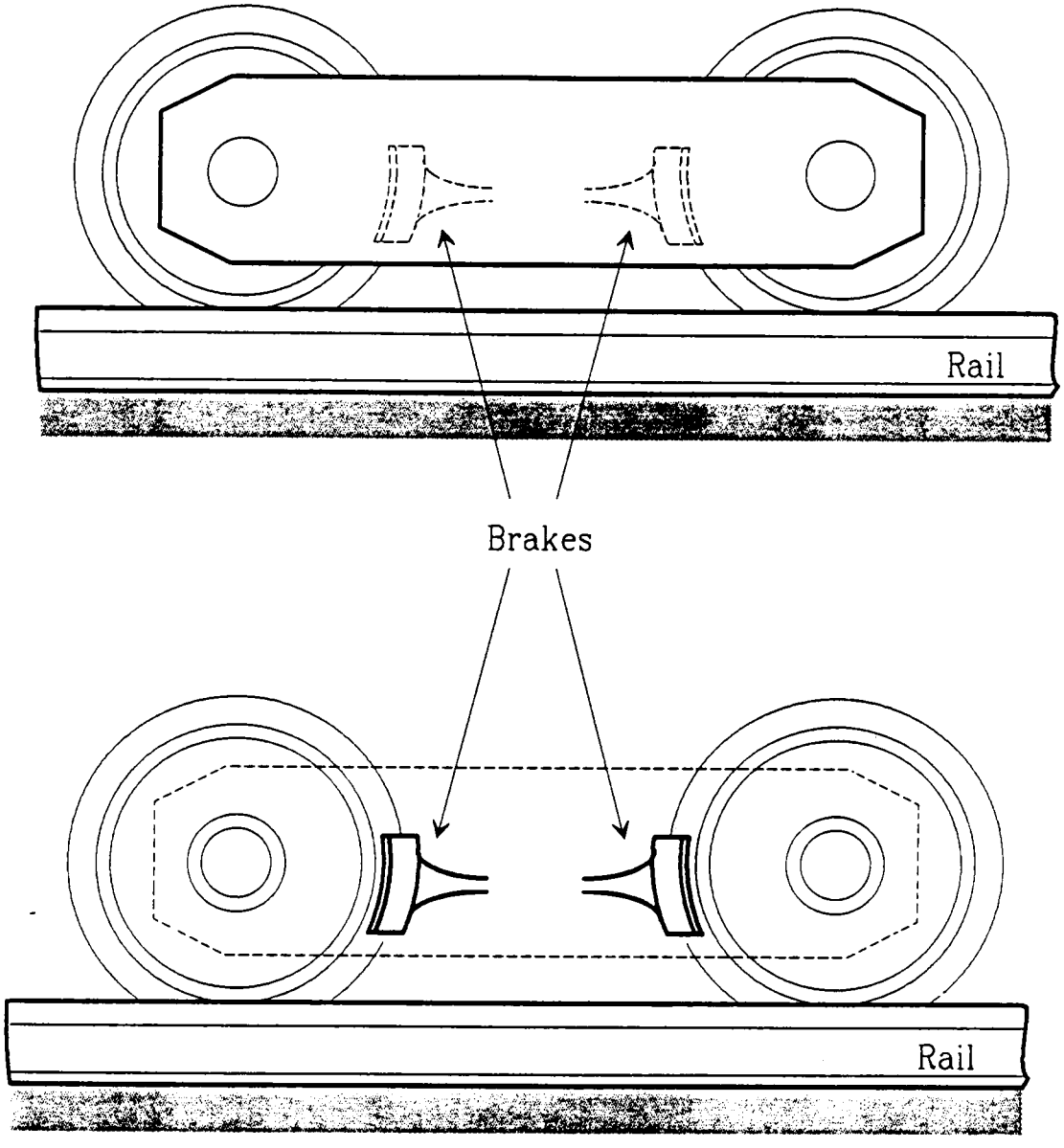

Figure 40. Position of the brake shoes on the tread of wheels.

Figure 41 illustrates how our postulate of thermal cycling might generate residual stresses.[76] During heating generated by the friction of the brake shoe contact with tread in the initial braking cycle, the grooved region in the tread deforms first elastically and then plastically in compression along the trace AB. At elevated temperatures, stress relaxation will occur along BB'. On the other hand, during cooling the grooved region follows the trace BC. When the wheel is completely cooled after the initial braking cycle, a residual tensile stress (AC) is developed in the groove. After each successive braking cycle, the residual tensile stresses will be increased gradually and will reach a range of cyclic thermal stresses from a tensile stress, S_T, to a compressive stress, S_C, in the closed hysteresis loop, GH.

The postulate of how residual stresses may be generated by the different thermal expansions between the groove and its neighboring regions[31] is illustrated in Figure 42. When the grooved region is heated to a relatively high temperature, it expands but is also restricted by the neighboring material. This causes the development of compressive stresses in the grooved region and tensile stresses in its neighboring regions. If the thermal gradient is large enough and the heating rate is fast enough, permanent yielding (plastic deformation) will occur between the groove and the neighboring regions. This results in more expansion of the neighboring regions than in the grooves. After the wheel is air-cooled, tensile residual stresses are developed in the groove and compressive stresses in the neighboring regions.

We note, however, that service residual stresses may be complicated by the initial residual stress field, by the condition of brake shoe contact with wheel, and by microsructural transformations in the material.

4.2.2 Hole Drilling Residual Stresses

Residual stresses were also measured by hole drilling for confirmation of the x-ray measurements as well as to obtain their depth profile. Section 12.2.1 shows the strains obtained from a

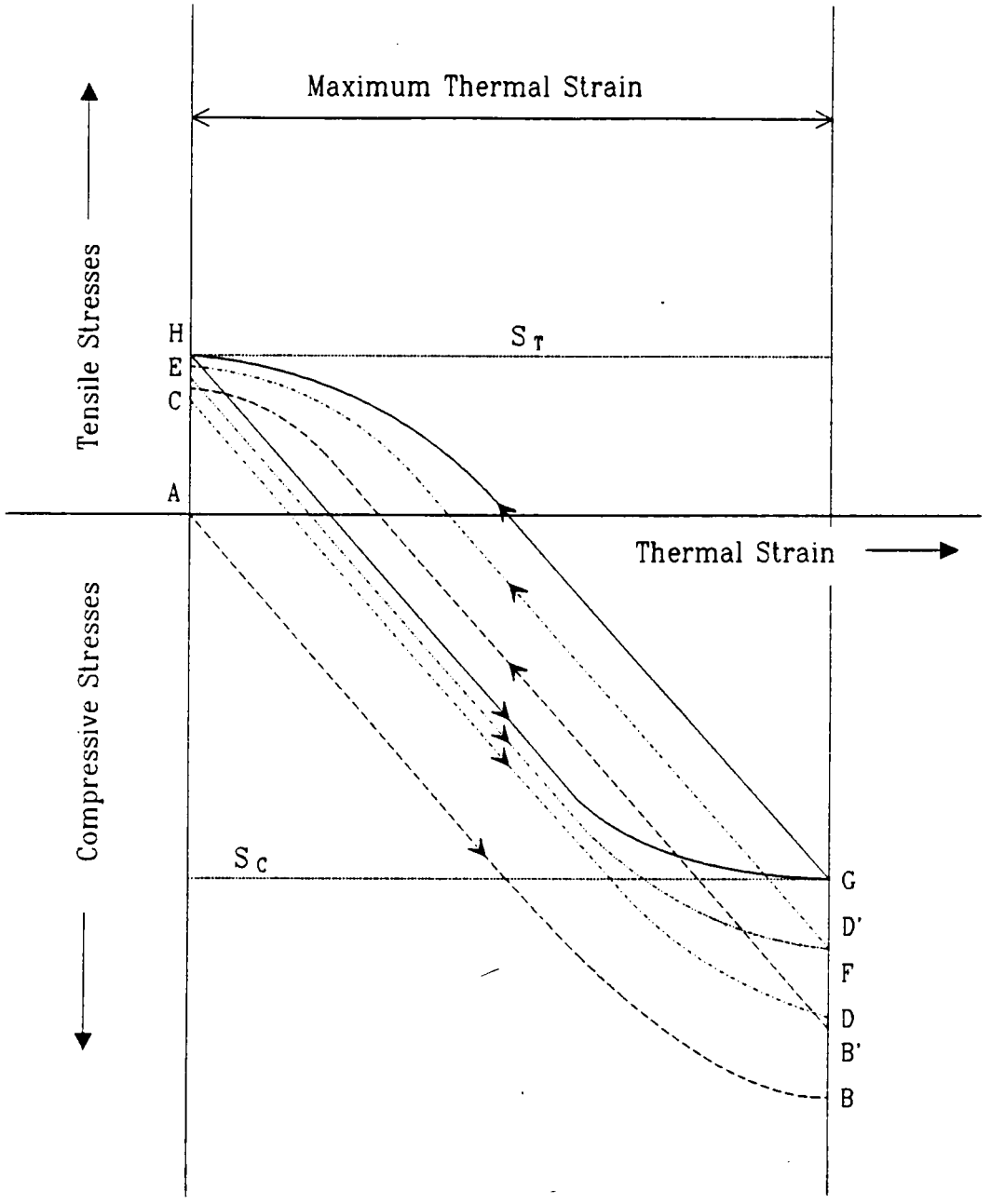

Figure 41. Schematic view of the generation of cyclical thermal stresses during repeated braking.[74]

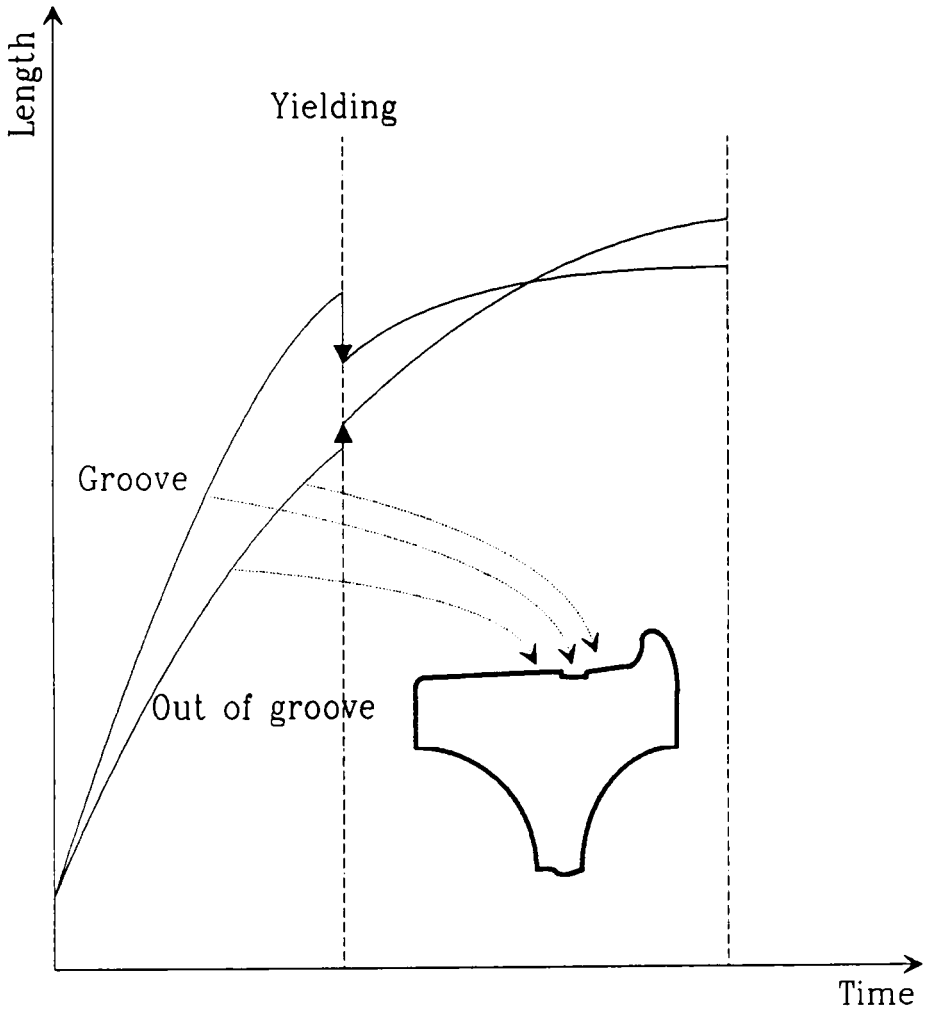

Figure 42. Schematic view of the expansion associated with heating rate.[75]

strain gage rosette mounted two inches from the front rim corner in the tread of the cast, normal wear wheel (Wheel F) and the approximate residual stresses in the sample coordinate system calcuated using Equations (3-14) through (3-15). The last column of Section 12.2.1 shows the more accurate residual stresses in the sample coordinate calculated using the finite element method which was supplied by Flaman.[84] Sections 12.2.2 and 12.2.3 show strains and approxiamte residual stresses at two inches and three inches, respectively, from the front rim corner in the tread of the heat-discolored (more than 4") wheel. Figure 43 shows the comparison of approximate and more accurate calcualtions of residual stresses for the cast, normal wear wheel (Wheel F). Both data show a smooth variation of residual stresses with depth. It is clear that the more limited approximation of Equation (3-14) does not differ greatly from the more exact results of the finite element calculatuion because the stress gradient is not too large. Since the residual stresses at the first depth increment should be the same between the two calculations, as is observed, and since we were interested only in the trend of how the residual stresses vary with depth, the simpler approach (Equation (3-14)) was used for all other hole drilling results presented in this work. Figures 44 and 45 show the residual stress variation with depth at 2" and 3", respectively, from the front rim corner in the tread of the heat-discolored (more than 4") wheel (Wheel E). Also, in both figures the x-ray and hole drilling residual stresses are intercompared at the near surface of the tread. The "x" represents the x-ray stress values. These figures indicate that x-ray residual stress measurements and hole drilling measurements are the same within the statistical accuracy of the data. For example, the x-ray measurement value at the surface of the groove of the heat-discolored (more than 4") wheel was 26 ± 5 ksi whereas the hole drilling measurement value at the same position was 20 ± 5 ksi.

The residual stress decreases with the depth, but does not vary steeply in the near surface region. This is a very important result in deciding whether x-ray diffraction can be applied to measure residual stresses in wheels. As was predicted by finite element analysis (See Figure 1.), the stress contours were expected to be perpendicular to the surface of the wheel. The data of Figures 43-45 are consistent with this hypothesis, suggesting that x-ray near surface measurements are indeed a valid measure of the state of stress in the wheel.

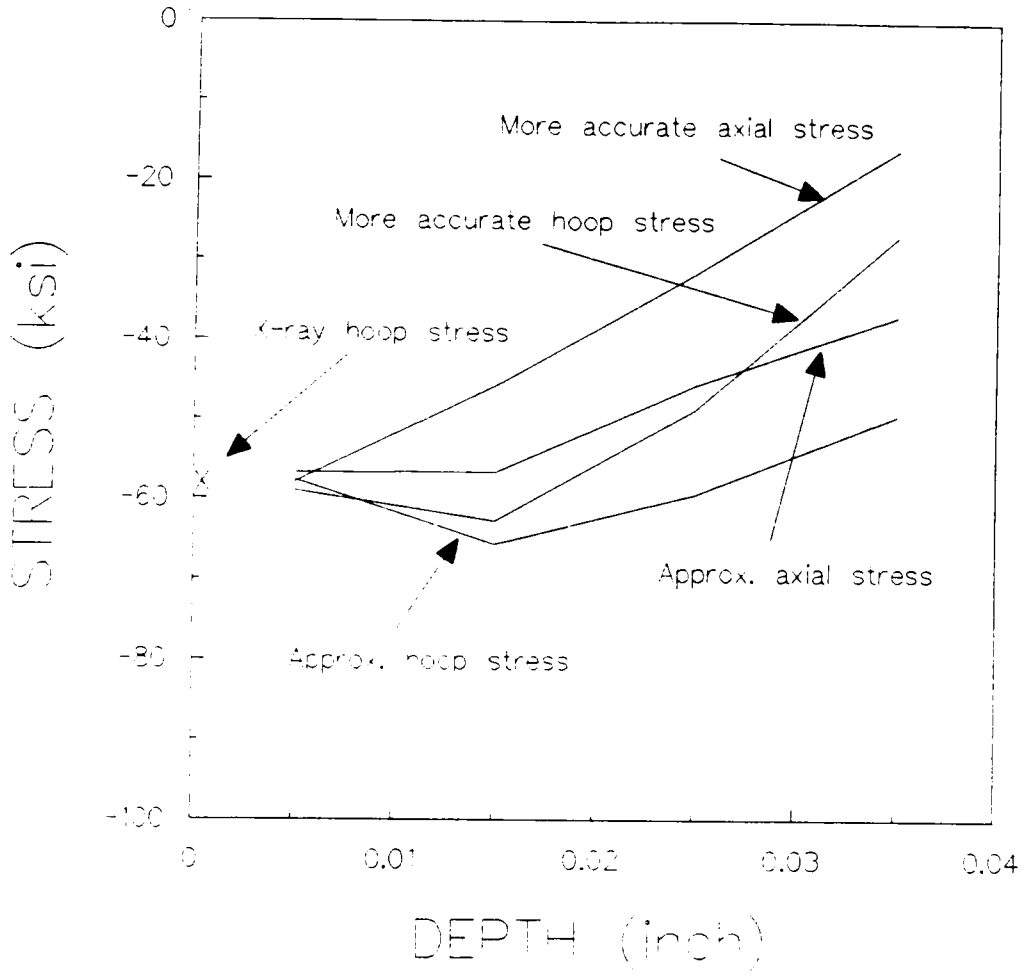

Figure 43. Comparison of approximate and more accuratele calculations of residual stresses at 2" from the rim corner: in the traed of the cast, normal wear wheel (Wheel F).

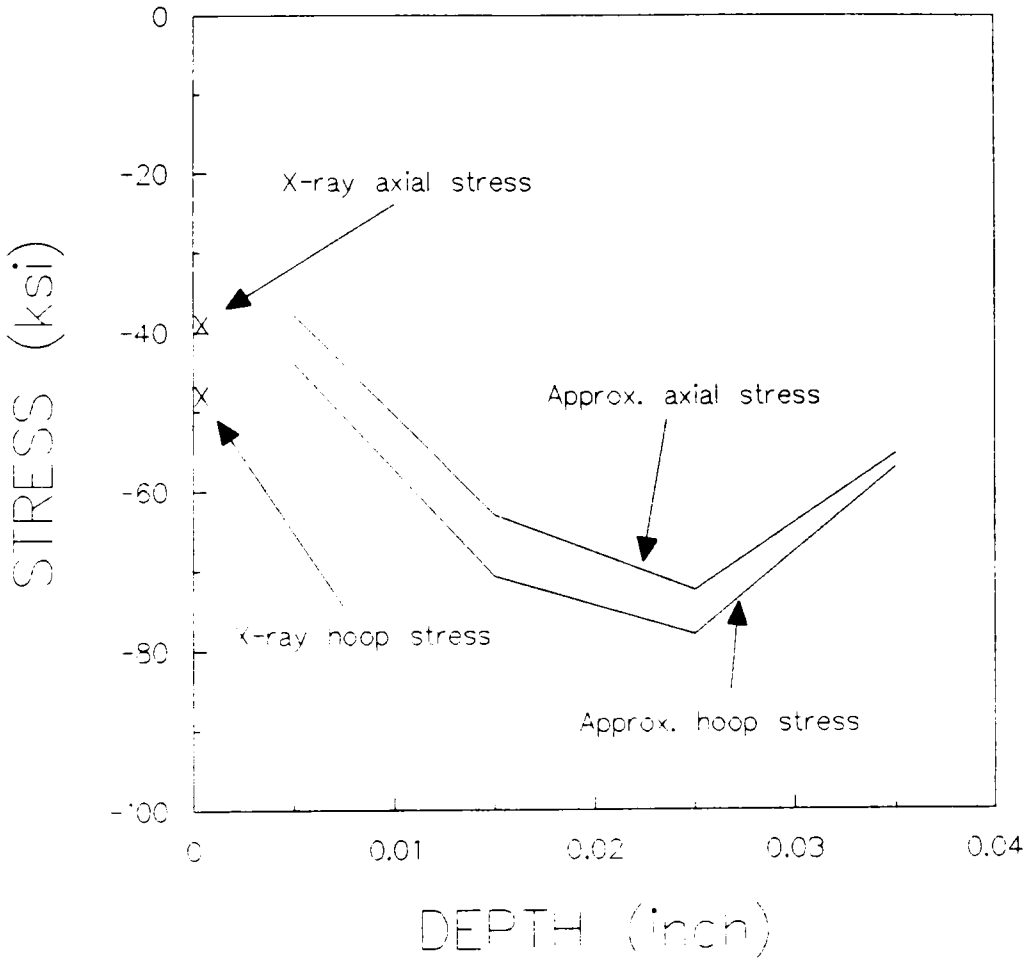

Figure 44. Approximate residual normal stresses variation with depth at 2" from the rim corner: in the tread of heat-discolored (more than 4") wheel (Wheel E).

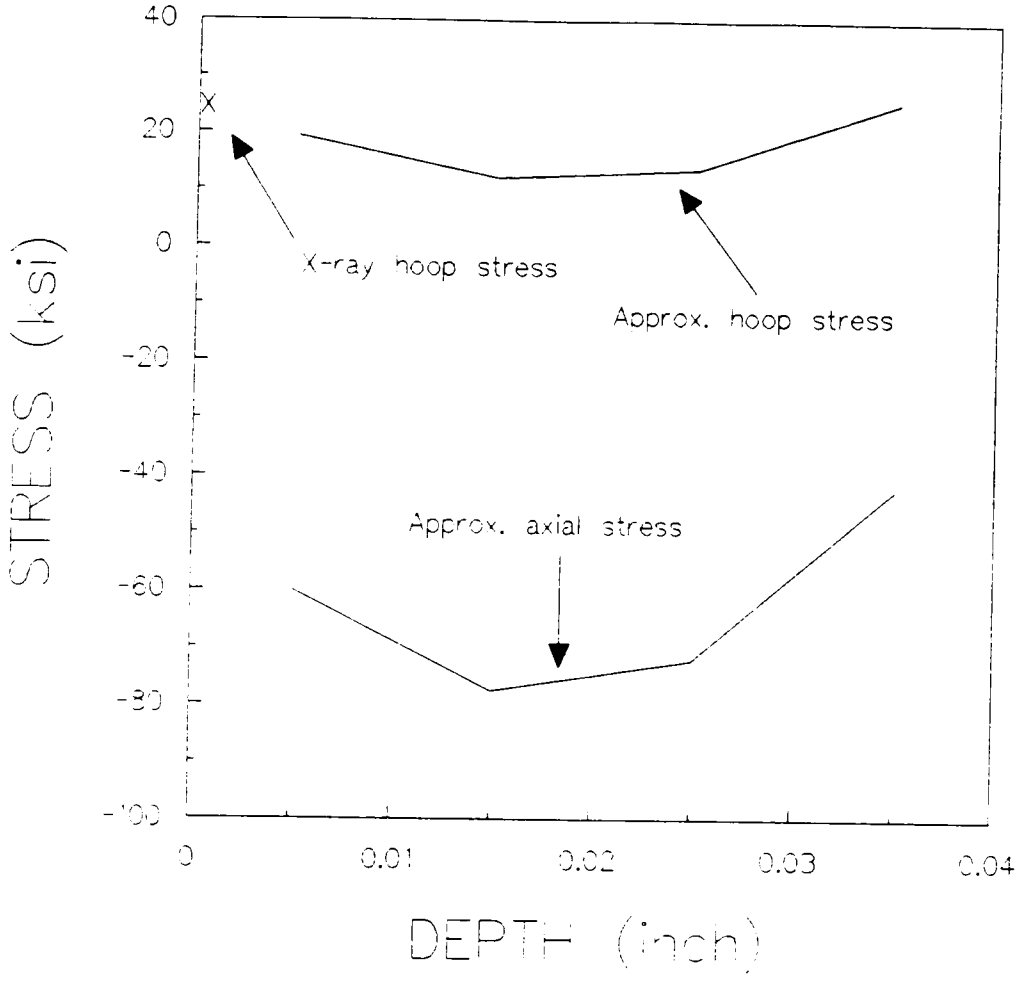

Figure 45. Approximate residual normal stresses variation with depth at 3" from the rim corner: in the tread of heat-discolored (more than 4") wheel (Wheel E).

5.0 STATISTICAL ANALYSIS

In Section 4.2.1, data were presented which permitted a likelihood ratio statistical analysis to determine if one (or more) of the sixteen axial locations might be used as an indicator for a service history sensitive location for x-ray measurements. In Section 5.1, it will be shown such a critical location at which the residual stress varies with service history in a statistically significant manner indeed can be identified.

The important problem to be addressed was the question of discriminating between good and bad wheels. Section 5.2 discusses the procedure of the discrimination using variance statistics. The variance statistical analysis utilized the x-ray residual stress data of Section 4.2.1 to relate the degree of the azimuthal stress fluctuation to the service histories. It will be shown that the overheated wheel showed significantly greater fluctuations than the other wheels.

5.1 CRITICAL MEASUREMENT POINT: Maximum Likelihood Test

The data shown in Figures 21 through 32 clearly indicate that the residual stresses (both normal and shear) vary significantly with location around the perimeter of the wheel. These variations are more clearly seen in Figures 46 and 47

The remaining questions are whether or not there is a quantitative means by which the stresses at one (or more) of these locations may be used to distinguish overheated wheels, and if so, does this stress vary monotonically with service history? With the help of the Statistical Consulting Center of the Virginia Tech Statistics Department (Prof. R. V. Foutz and graduate student B. K. Koons) we have developed a likelihood ratio test to answer the first of these questions. The second question is answered in the next section.

In the likelihood ratio test,[85] the parameter

$$\lambda_K = \frac{\sum_{i}^{6}\sum_{j}^{2,4}(X_{ijk} - \bar{X}_{..K})^2}{\sum_{i}^{16}\sum_{j}^{6}(X_{ijk} - \bar{X}_{j\,.\,k})^2} \qquad (5-1)$$

where

X_{ijk} = measurement at the particular position, k, of the particular azimuthal angle, j, of the wheel, i.

$\bar{X}_{..k}$ = average of all the measurements of the particular position, k.

$\bar{X}_{i.k}$ = average of all the measurements at the particular position, k, of the particular wheel, i.

In equation (5-1), λ_K is a parameter which measures how much the data at a given location in a given wheel vary from the mean of the data for that location for all wheels. Small values of λ_K in-

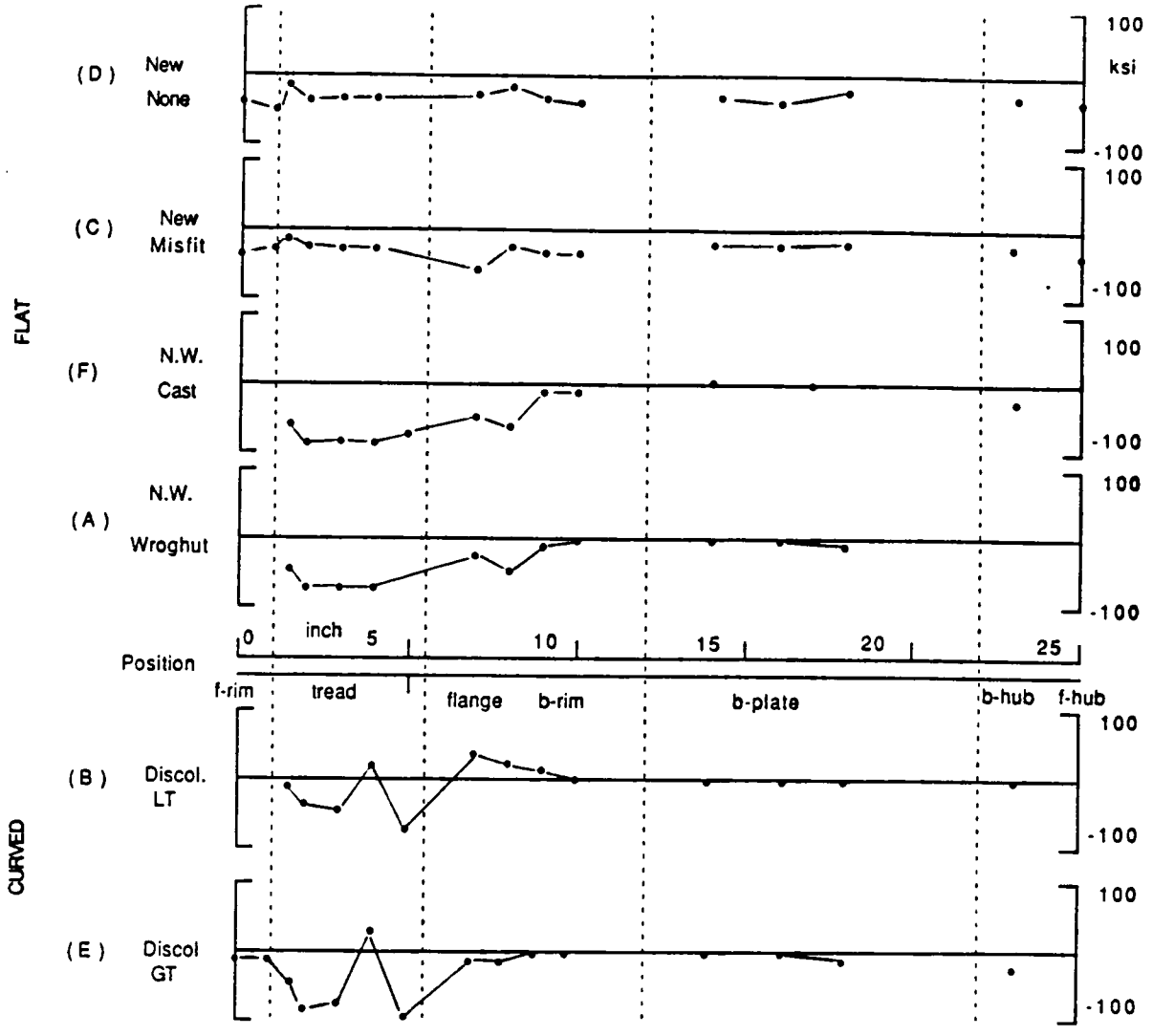

Figure 46. Intercomparison of mean normal (hoop) stresses at a various locations in six wheels of differing service histories.

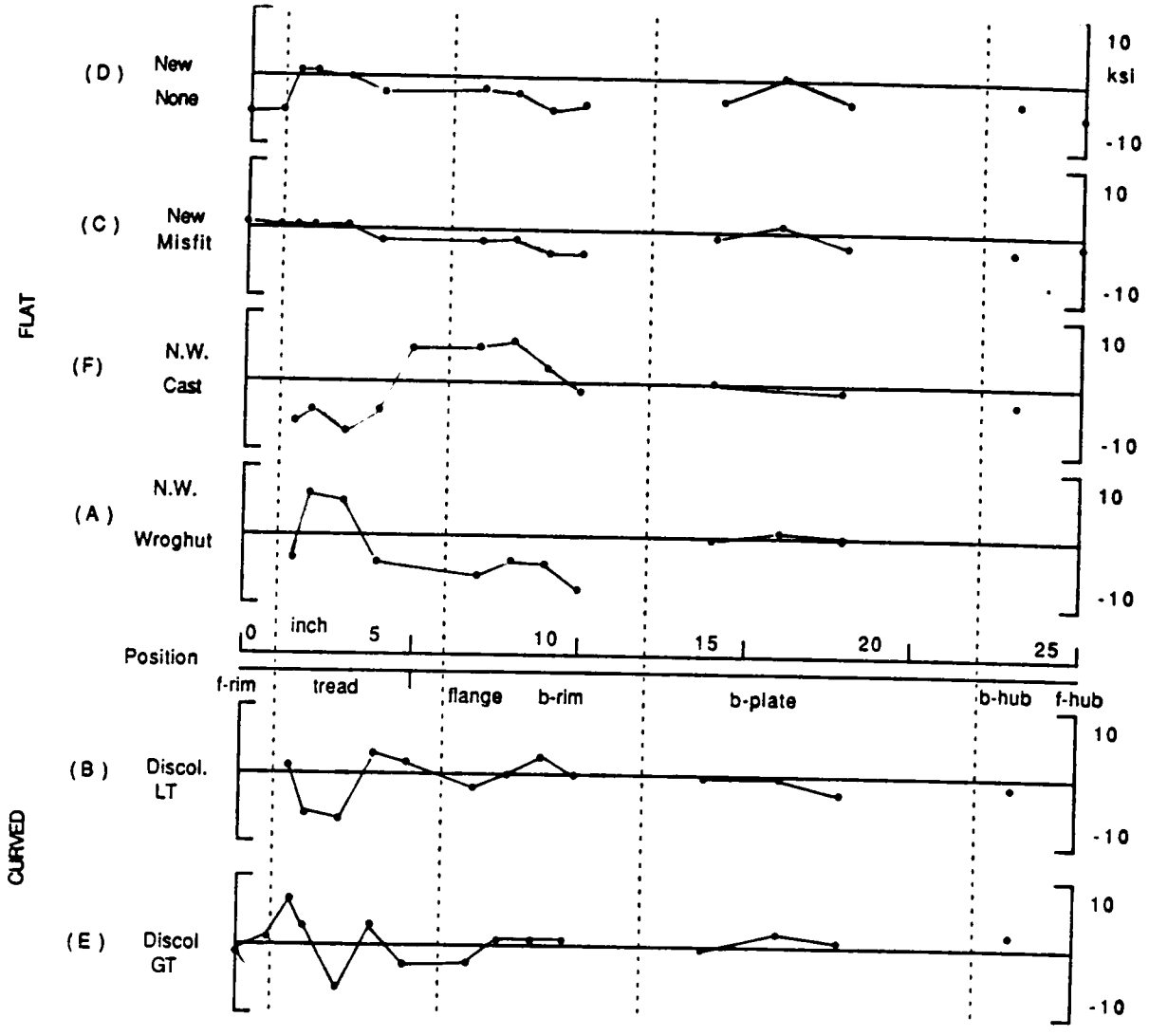

Figure 47. Intercomparison of mean shear stresses at a various locations in six wheels of differing service histories.

dicate little statistical significance to the variations, while large values indicate considerable significance. The results of this analysis, computed using all of the data in Appendix B and treating six wheels as a single indistinguishable group, are shown in Figure 48. As a statistical significance test, the λ_K values computed from Equation (5-1) may be compared with $\frac{n}{P} F_{n,P}$ where F is found in standard statistical tables, $n = i + j + k - 1$, and $P = i + j + k - m$ where m is the number of wheels and i, j, k are defined in Equation (5-1). Because different numbers of measurements were made at the various locations on each wheel, the statistical parameter $\frac{n}{P} F_{n,P}$ is different for each location. The values for 95% confidence limits are given in Table 3. Those locations for which $\lambda_K >> \frac{n}{P} F_{n,P}$ are locations at which the stress varies significantly with service history. A clearer picture of this may be gained if one plots the ratio $R = \lambda_K / \frac{n}{P} F_{n,P}$ as shown in Figure 49. Here, λ_k value for each location is normalized at the 95% confidence limit, and those locations which show $R >> 1$ are very sensitive to service history while those with $R < 1$ are insensitive. Thus, it is clearly seen that several locations show significant variations among the various service histories. However, it is those locations at center of the the tread (location 6), on the plate (locations 11-13), and possibly at the tip of the flange (location 8) which show the greatest sensitivity.

Note that location 6, which has the largest λ_K and, thus, the greatest sensitivity, is approximately 3 inches from the front rim and is in the grooves cut in the overheated wheel. The effect is also clearly seen in Figure 46. A likelihood ratio test of the shear stress data is more difficult to interpret. As may be seen in Figure 47, the shear stresses change sign with location on the wheel. After some thought, one realizes that the sign of the residual shear stress in any given wheel must depend on the "handedness" of the wheel. In other words, the sign depends on whether the wheel was on the left-hand side of the car, or the right-hand side. But, since railroad cars have no front or rear, and see service in both directions (probably randomly), examination of the data of Figure 47 suggests that the data for wheels B and F may be of opposite sign from those for the other four wheels. Because of such possible effects, the likelihood ratio test was applied to the shear stress data of Appendix B in two ways. First, the R values for the data from all six wheels was computed in normal way. The results are shown in Figure 50. From these data, it is seen that the shear stresses

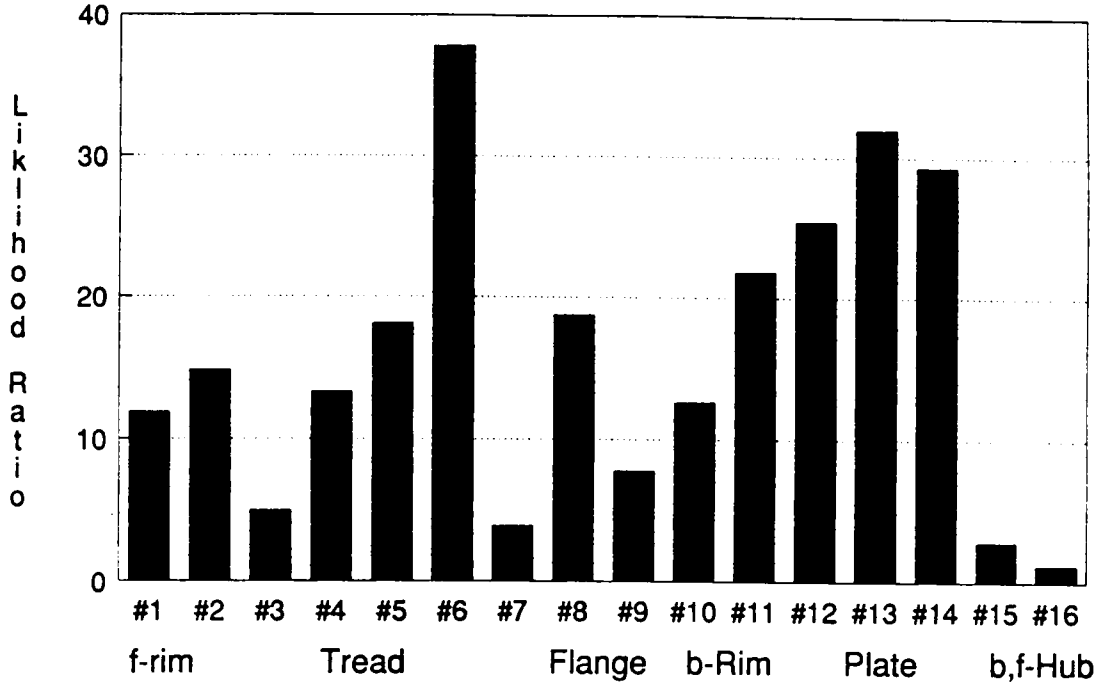

Figure 48. Likelihood ratio, λ, for normal stresses at various wheel locations.

Table 3. Statistical significance values for various locations on complete set of six wheels

Measurement Location	$n = i + j + k - 1$	$P = i + j + k - m$	$\frac{n}{P} F_{n, p, 0.95}$
1,2	5	3	15.0
3,4,9,10	14	9	4.7
5,8	15	10	4.3
6,11	13	8	5.3
7	7	5	6.8
12,13	11	7	5.7
14	8	4	12.1
15	9	5	8.6
16	3	2	28.7

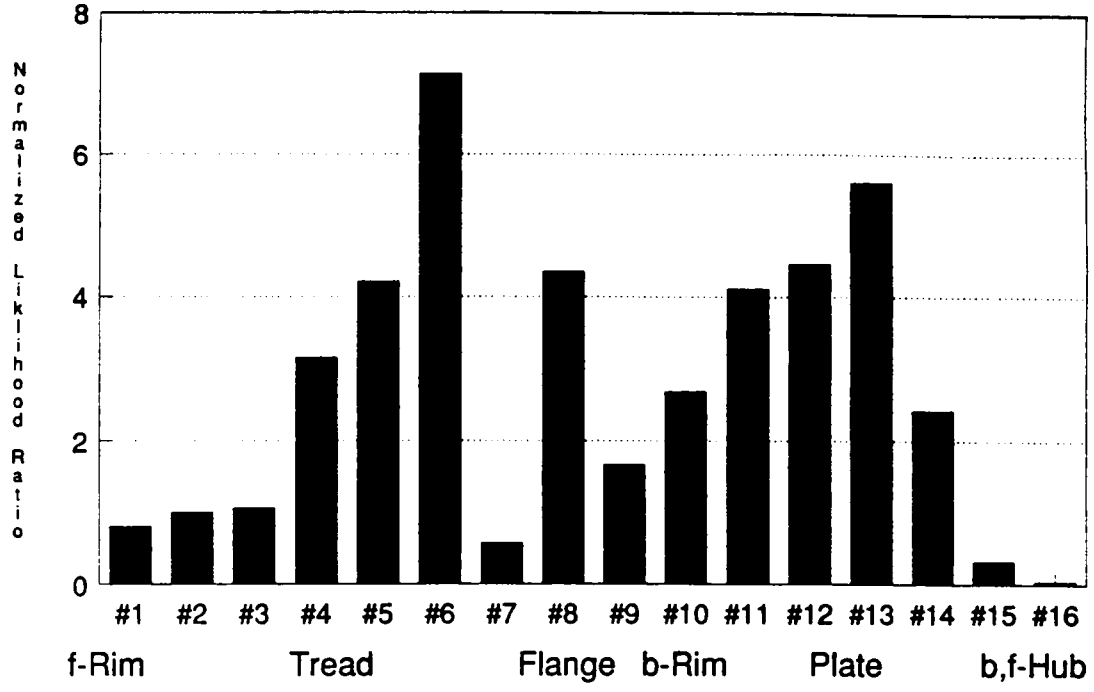

Figure 49. Normalized likelihood ratio, R, for normal stress at various wheel locations.

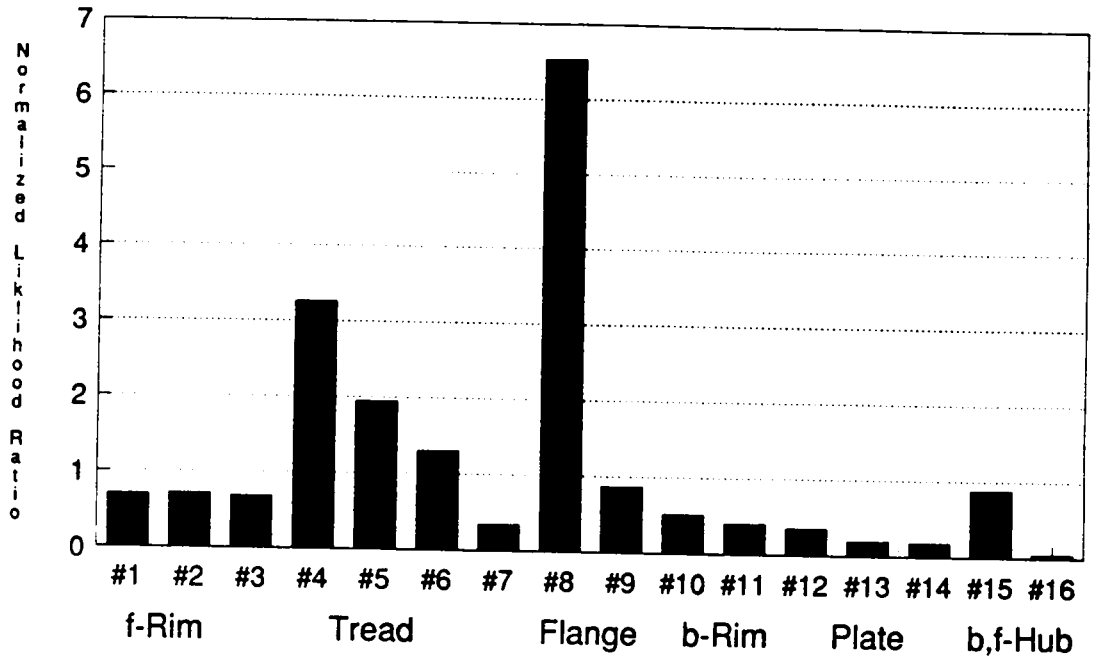

Figure 50. Normalized likelihood ratio, R, for shear stress at various wheel locations.

in the edge of the tread (location 4) and in the flange (location 8) are highly sensitive to the service history of the wheel.

In order to estimate the effect of the possibility of reversed signs of the shear stresses due to uncertainty in the "handedness" of the wheel, the sensitivity ratio, R, was recomputed after changing the signs of all the data for wheels B and F as suggested above. The results are shown in Figure 51. It is seen here that this effect makes location 4 less sensitive than the results shown in Figure 50, but has little effect on the sensitivity at location 8.

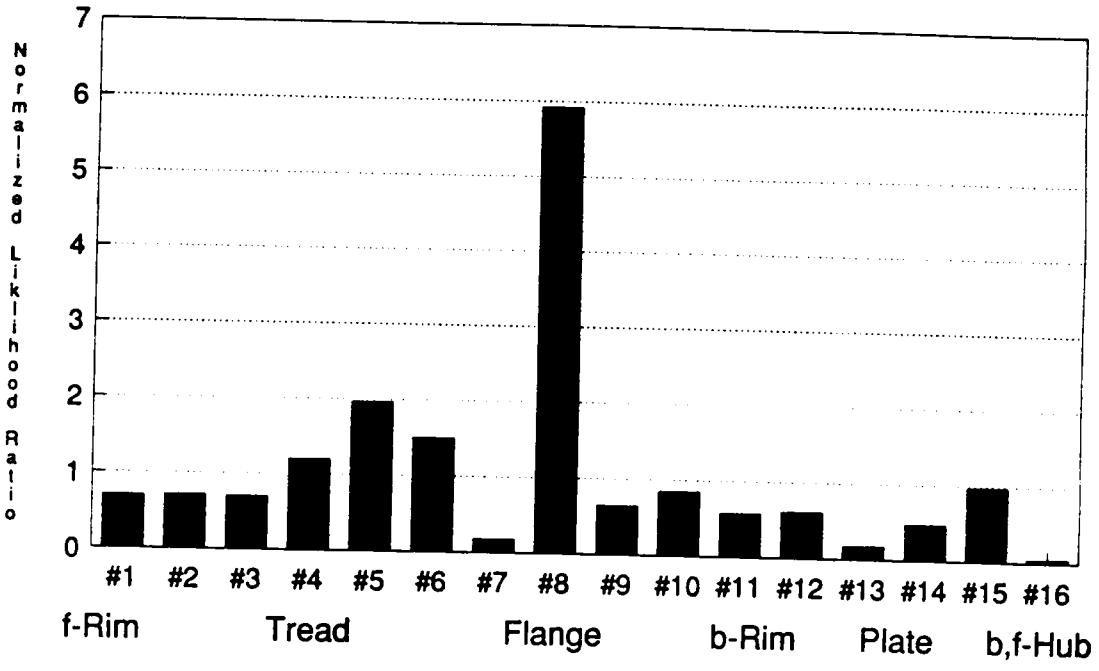

Figure 51. Normalized likelihood ratio, R, for shear stress at various wheel locations.: The signs for the data from wheels B and F have been reversed.

5.2 *DISCRIMINATION ANALYSIS: Variance Test*

The data of Figures 33 through 38 clearly indicate that the residual stresses in the greater than four inch discolored wheel vary with the azimuthal location around the wheel. The fluctuations are subtantially less in the other five wheels. In order to clearly observe the stress pattern with respect to the service history, the residual stresses of the six wheels are assembled in Figure 52. The question to be answered is whether there is any possibility of discriminating between good and bad wheels using the fluctuations of these data. This question can be easily solved by applying a quantitative approach using variance statistics which estimate the degree of stress fluctuation from the mean value. The approach developed with the help of the Statistical Consulting Center of the Virginia Tech Statistics Department (Prof. R. V. Foutz) is that of variance statistics.[56,57] In this analysis the parameter, S_k, which is given by

$$S_k = \sum_{j}^{16} \frac{(X_{ik} - \bar{X}_{i.})^2}{n} \qquad (5-2)$$

where

X_{ik} = measurement at the particular azimuthal angle, k, of the particular position, of the particular wheel, i,

$\bar{X}_{i.}$ = average of all the measurements at the particular position, of the particular wheel, i, and

n = degree of freedom,

is a measure of how much the stress varies in the circumferential direction from the mean of the stress data at the critical location for all six wheels. A small value of S_k implies little fluctuation of residual stresses with respect to the circumferential angles. The result of this analysis is shown in Figure 53. This figure clearly implies that the heat-discolored (more than 4") wheel shows the maximum variance of residual stress compared with other five wheels. The rest of wheels do not

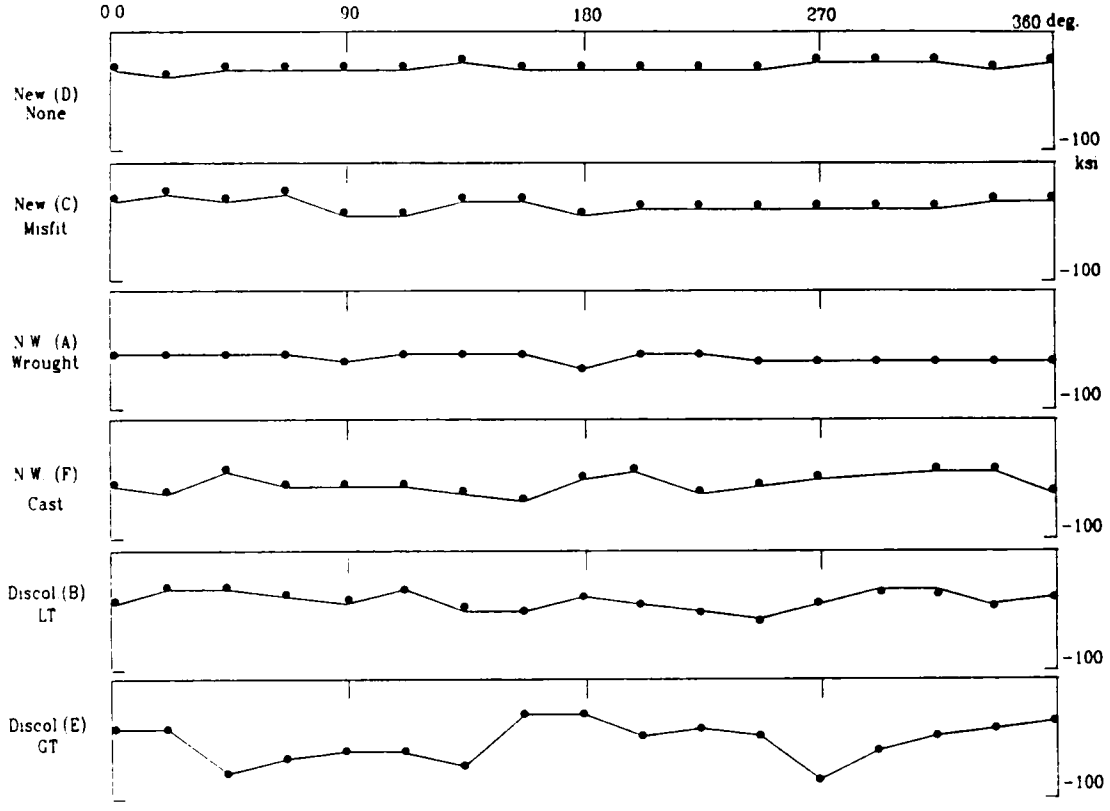

Figure 52. Intercomparison of normal stresses at various azimuthal angles in six wheels of different service histories.

Figure 53. Variance, S_k, for normal stresses with respect to service history.

show a significant statistical difference from each other. The appearance of the heat-discolored (less than 4") wheel, indicates that it is bad. However, the variance test shows it may still be good. The heat-discolored (more than 4") wheel, Wheel E, shows a severe variation of stress with the azimuthal angle in the tread. It is believed that this wheel has hot zones. Such azimuthal variations of the normal stresses are expected when variations in manufacture, metallurgy, and service history are considered. It is suggested that the hot zones come from the slipping of brake shoe contact with tread, rail contact with tread, or both when the brakes are applied.

A further statistical analysis was performed by fitting the data of Figures 52 to either a first or second order of Fourier series by a least squares technique. The results are shown in Figures 54-56. The equations for the least squares fit are given in Table 4. The magnitude of the coefficients in the Fourier series gives in Table 4 should be coupled with the values of S_k computed for each wheel. Large values of S_k are directly correlated with large Fourier coefficients. It is clear from these data that the stresses in the wheels are not random, but vary periodically with azimuthal angle around the wheel in all but one case. It is interesting to note that the most damaged wheel has a periodicity of $2\omega t$ while all the other wheels have a periodicity of $1\omega t$ (or is constant). These results will be discussed in more detail in the next chapter.

(a)

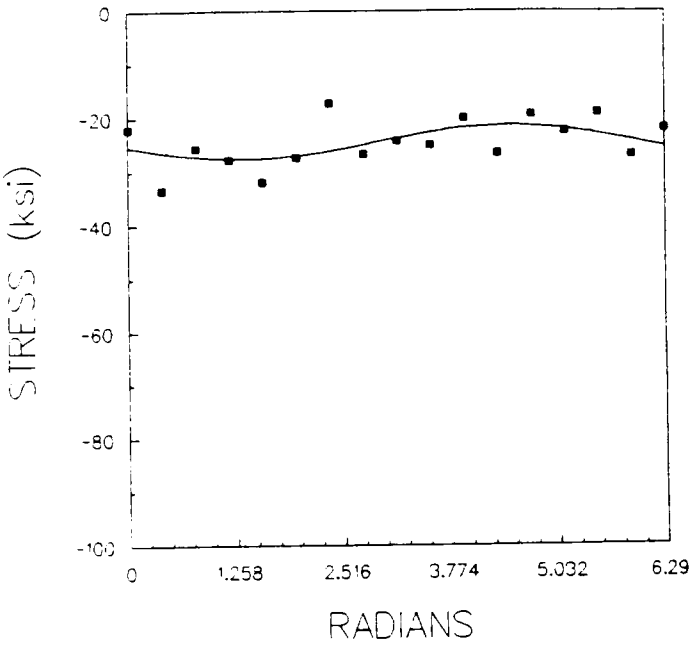

(b)

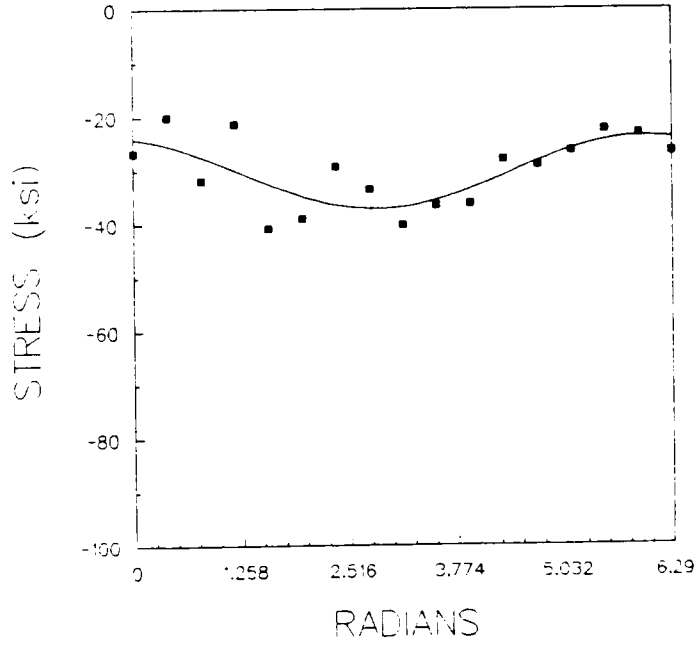

Figure 54. Least squares fit of the residual stresses in the azimuthal direction: (a) a new wheel (Wheel D) and (b) a new, misfit wheel (Wheel C).

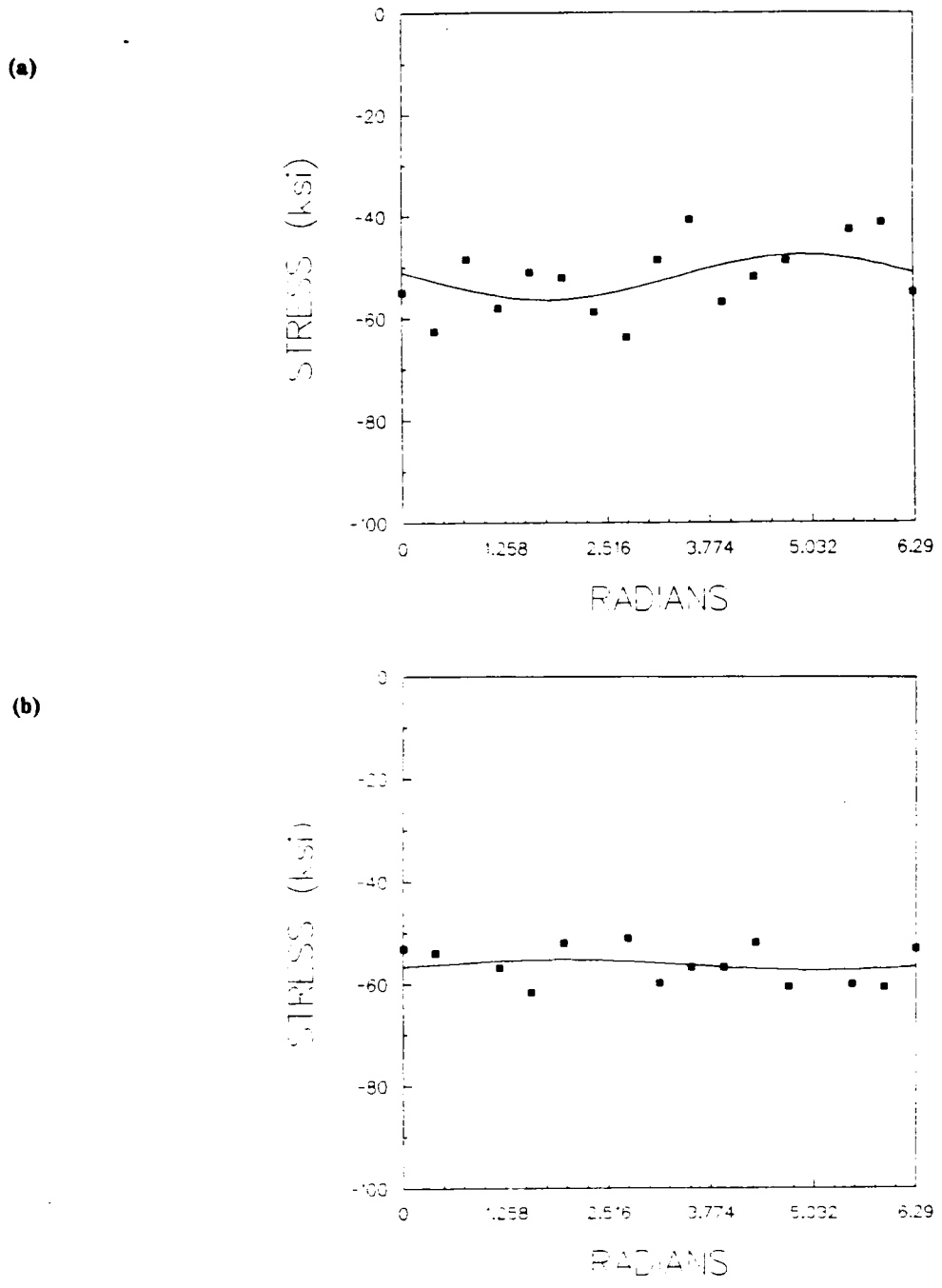

Figure 55. Least squares fit of the residual stresses in the azimuthal direction: (a) a wrought, normal wear wheel (Wheel A). and (b) a cast, normal wear wheel (Wheel F).

(a)

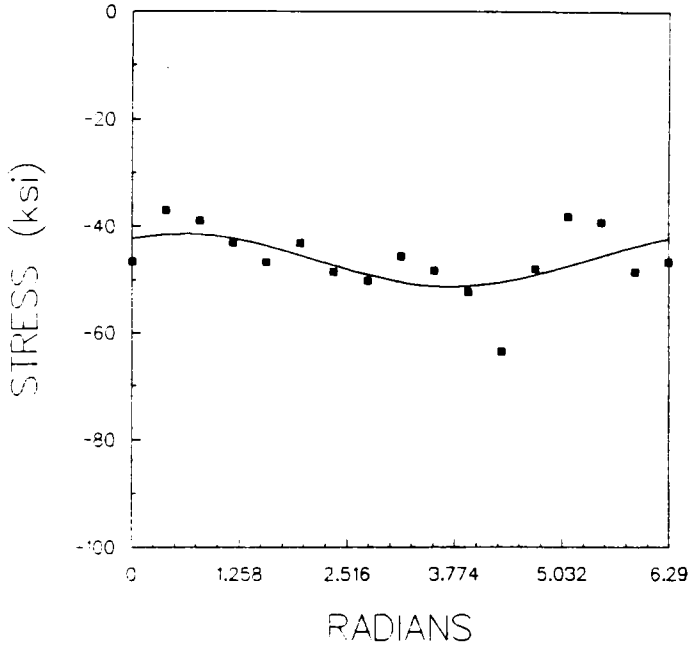

(b)

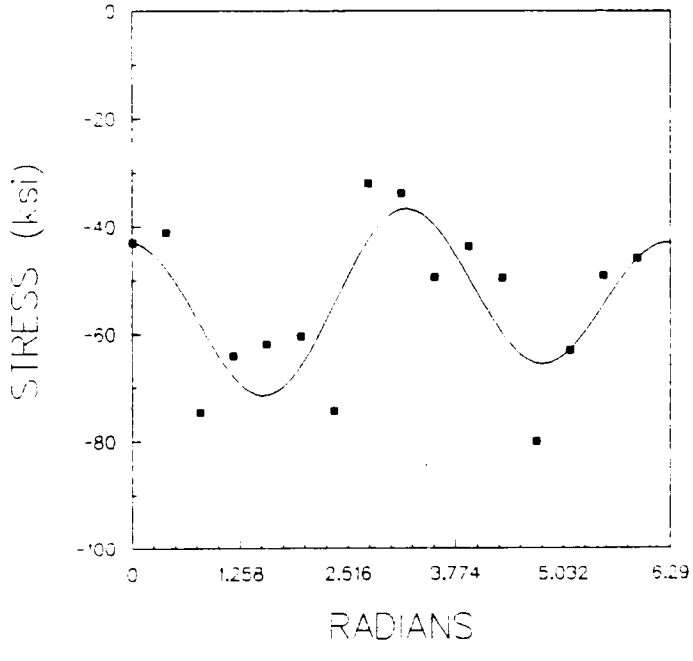

Figure 56. Least squares fit of the residual stresses in the azimuthal direction: (a) a heat-discolored (less than 4″), several grooved wheel (Wheel B). and (b) a heat-discolored (more than 4″), a grooved wheel (Wheel E).

Table 4. Equations for the least squares fitting of the residual stresses shown in Figure 52.

$\sigma = \sigma_0 + a_1\cos\omega t + a_2\sin\omega t + b_1\cos 2\omega t + b_2\sin 2\omega t$

Wheel Identification	σ_0 (ksi)	a_1 (ksi)	a_2 (ksi)	b_1 (ksi)	b_2 (ksi)	R^2
New	- 24	- 0.8	- 3.0			0.25
New Misfit	- 30	6.4	- 2.1			0.55
Normal wear wrought	- 52	0.9	- 4.3			0.03
Normal wear Cast	- 56	- 0.3	1.0			0.19
Discolored less than 4″	- 46	4.0	2.7			0.32
Discolored more than 4″	- 54	- 3.1	- 3.0	14	0.5	0.55

6.0 DISCUSSION

The data and analyses of the previous chapters raise some important and interesting questions. First among these is: Are the results reasonable and consistent with previous work? This is a difficult question to answer for several reasons. Saw cutting has been the primary tool used in the past to determine the state of stress in a used wheel. However, saw cutting measures a complex average of the stresses throughout the bulk of the wheel in the vicinity of the cut, whereas the x-ray measurements determine only the local near-surface stress at the point of observation. Since there has been, to date, no data acquired by both methods from the same set of wheels, there was no way to intercompare the data. It has been the industry experience[1,4] that in some wheels in which two radial saw cuts were made there are both tensile and compressive residual stresses. These effects were attributed to hot zones in the wheels. The present observations of large, systematic fluctuations of the residual stresses in the tread of the overheated wheel (greater than four inches, Wheel E) are consistent with such saw-cutting results.

In this research, an intermediate measure of residual stresses between those provided by saw cutting and by x-ray diffraction was possible by hole drilling at selected locations. Hole drilling provides an indicator of bulk stresses in the vicinity of the hole which would not average the data over as much material as the saw cut. The excellent agreement of the surface residual stresses estimated by hole drilling and x-ray diffraction is gratifying. Furthermore, the relatively shallow gra-

dients of the stresses with depth justify the assumptions made in Chapter 2. In the future, it is suggested that such measurements be made on all six wheels characterized in the present work prior to their destruction by saw cutting.

Opinsky et al.[12] have calculated the residual stresses expected (including those at the surface) in a severely overheated wheel by a finite element method. Their results indicate that the normal stresses should become tensile nearly everywhere on the surface of the wheel. Some of their data are replotted in the format of the data presented in Section 4.2, as shown in Figures 55-57. These results should be compared with Figures 21 through 32. The present data indicate that in areas where there was clearly a high thermal load, such as in the region where a groove was cut in the wheel, the surface residual stresses are tensile, as predicted. However, on the same wheels in regions away from the point of application of the load, the normal stresses remain compressive in disagreement with the theoretical predictions. This is not altogether surprising because it is clear that the actual changes in residual stresses in overheated wheels is more complex than the computed effects. The most likely reason for the discrepancy will be found in the underlying assumptions of the calculations.

An important unanswered question raised by these results centers around whether the bulk stresses in the wheel are more nearly represented by the calculated data or by the x-ray near surface measured data. This question was answered by an intercomparison of hole drilling and x-ray diffraction. This intercomparison indicates no steep variation in near surface stresses. This suggests that the near surface stress measured by the x-ray diffraction can represent bulk stress.

Another achievement of the intercomparison was that the residual stresses were confirmed by the hole drilling technique. The intercomparison showed that the difference of the stress measurements between two techniques is within the range of the error of stress measurements. For example, the x-ray stress is 26 ± 5 ksi at 3″ from the back rim corner on the tread of the discolored (more than 4″) wheel whereas the hole drilling stress 20 ± 5 ksi.

The analysis of Section 5.1 clearly shows that the state of residual stress varies as a function of service history at certain key locations on the perimeter of the wheels. However, several important questions remain unanswered. Among these are (1) is it important to distinguish among the various

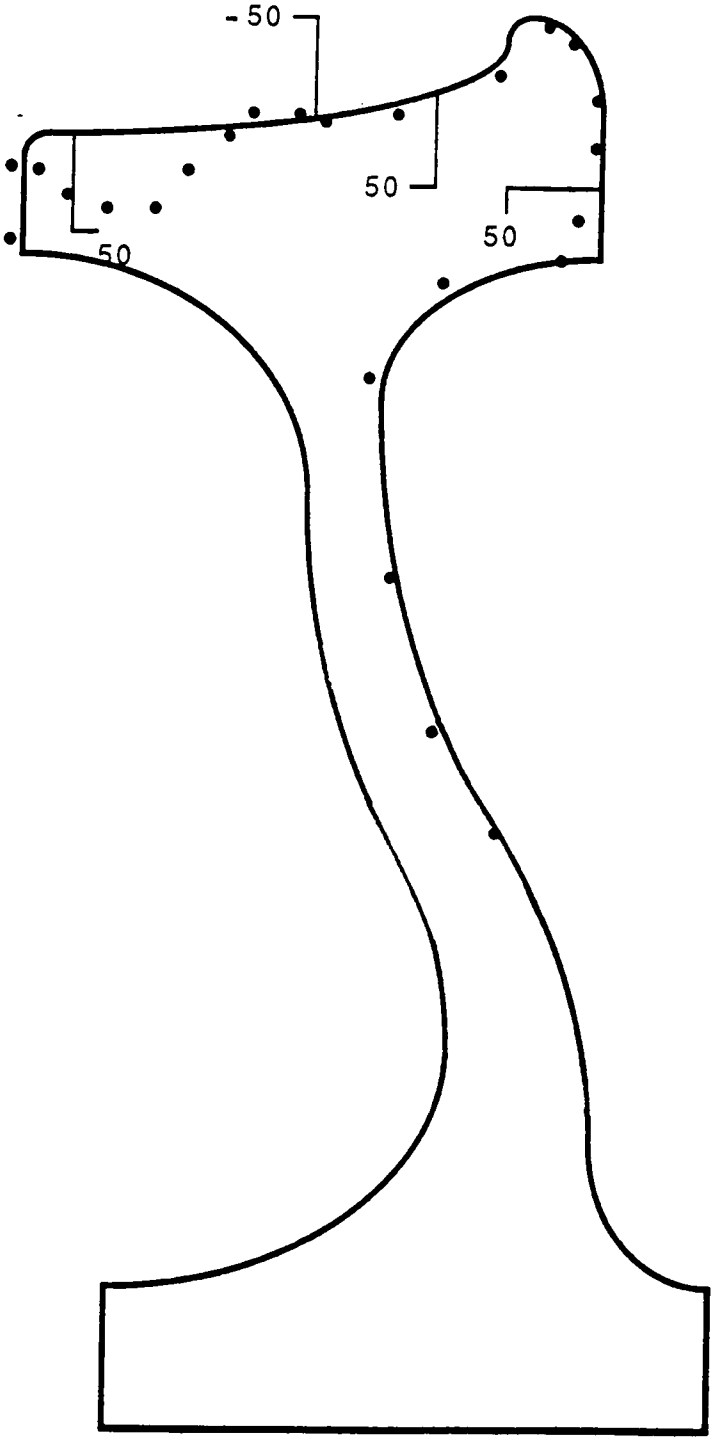

Figure 57. Circumferential residual stress for 36″ curved wheels cooled to ambient temperature: following 60 minutes of a 48 bhp (35.8 kw) thermal load to the overhanging breaking force [12].

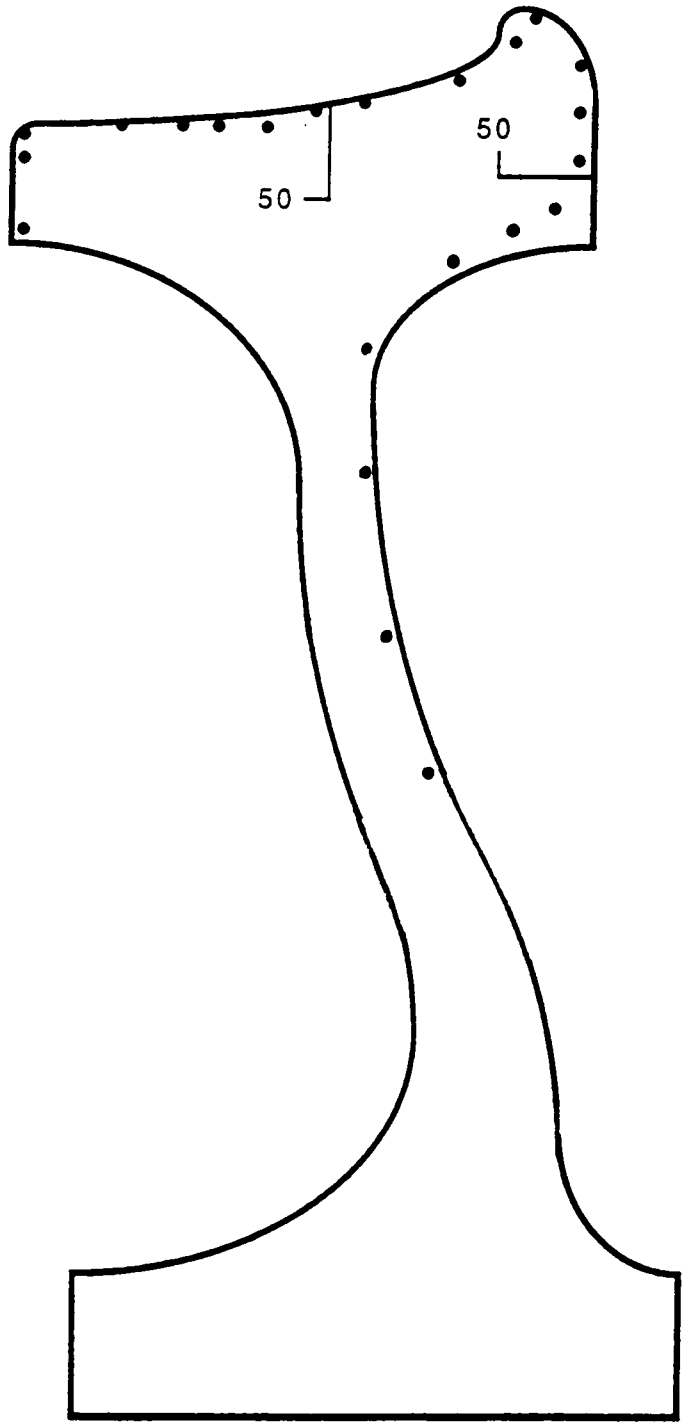

Figure 58. Circumferential residual stress for 36" curved wheels cooled to ambient temperature: following 60 minutes of a 48 bhp (35.8 kw) thermal load to the centered breaking force [12].

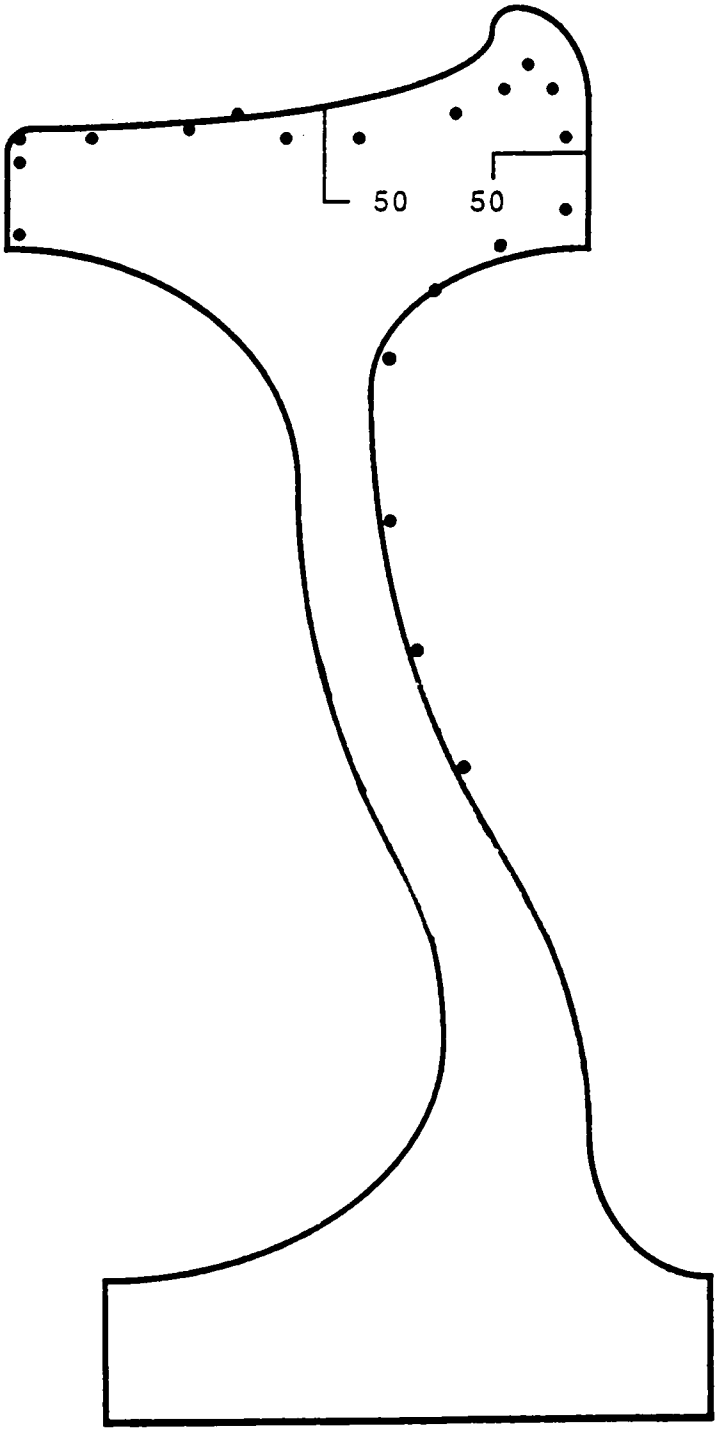

Figure 59. Circumferential residual stress for 36" curved wheels cooled to ambient temperature: following 60 minutes of a 48 bhp (35.8 kw) thermal load to the overriding breaking force[12].

types of wheel designs, (2) can a single stress measurement at a key location indicate wheel overheating, and (3) does the stress at these key locations vary monotonically with some measure of service history?

In the beginning of this research, it was decided that it was important to characterize a range of wheel designs and service histories which was representative of the wheels currently in service. Thus, as was seen in Table 1 wheels of two stress designs, two differing metallurgies, from three manufacturers, and with at least two different shape designs and two plate designs were examined. One might normally expect that the states of stress in each wheel of any given service history would vary with each of these parameters. If such variations are large from each type of wheel, the variations in residual stress with service history would be masked and the objective of this research program could not be reached. The results of Section 5.1 unambiguously show that such is not the case. Indeed, in the analysis presented in Section 5.1 because only six wheels were examined and because of the large number of wheel design parameters represented by these six, it was not possible to make any distinctions among them. In other words, from a statistical point of view, it was assumed that all the wheels came from the same population. That the effects of service history on residual stress stand out so clearly, as shown in Figure 49-51 unambiguously shows that these variations are far more significant than variations which may result from various wheel design parameters. This is a crucial observation because it indicates that it is likely that a residual stress testing procedure can be developed in which the discriminant test for "good" versus "bad" or overheated wheels is independent of the type of wheel under investigation. This hypothesis is strengthened further by our observations which imply that the stress fluctuations at the critical locations are superior indicators of severely overheated wheels than in the absolute value of the mean stress. If this proves to be the case, it will allow enormous simplification in the field test procedures proposed for future work.

The second question regarding the identification of key locations for stress measurements on the wheel, and the third question, regarding monotony of the stresses with service history are interrelated. The likelihood ratio test developed in Section 5.1 clearly identified several potential locations to be considered as key locations. These included the center of the tread, the flange, back rim, and

the plate. The likelihood ratio test does not take into consideration any information concerning service history of the wheels while the variance tests described in Section 5.2 suggest that fluctuations in the stresses at the critical locations may be the key to developing a reliable NDE technology. It only tests to see if there are significant variations of the stresses at various locations among the wheels. Similarly, the variance tests also do not take service history into consideration, but only serves to identify wheels with abnormal fluctuations. To be useful as a tool for retirement for cause in the industry, it is essential to demonstrate a monotonic relationship between residual stress at key locations and service history. Examination of Figure 49 shows that at some key locations (e.g. location 6) such monotony does not exist. Rather, the compressive residual stress increases (becomes more compressive) as the wheel sees normal wear, and only on overheating does it decrease or become tensile. This effect can cause serious problems with the interpretation of the data of Figures 46 and 49 because there are two values of service history which can result in a given observed residual stress.

To confirm that the key locations identified in Figure 49-51 are unaffected by this effect, we assume that new wheels are "broken in", or reach an equilibrium state of residual stress reasonably rapidly. If such is the case, the likelihood ratio test can be repeated using only the data for used and overheated wheels. The normalized results of such an analysis are shown in Figure 58. From these results, it is seen that the original identification of key locations was valid. However, it is seen that the location on the plate are no longer significant. A similar analysis for the shear stress produced data essentially identical to those of Figures 50 and 51.

These results show that the changes in circumferential normal stresses in the plate occurred during "break in" while those in the tread and flange occurred during overheating. On the other hand, all significant changes in shear stresses at location 8 appear to occur during overheating.

The identification of a critical, or most sensitive, points for changes in residual stresses with wheel overheating are consistent with the work of Carter et al[27] in which the fracture mode of 7 wheels was examined. On comparison of our suggested key locations with these data, it is seen that the origin of the crack leading to fracture for the majority of these wheels coincides with one of

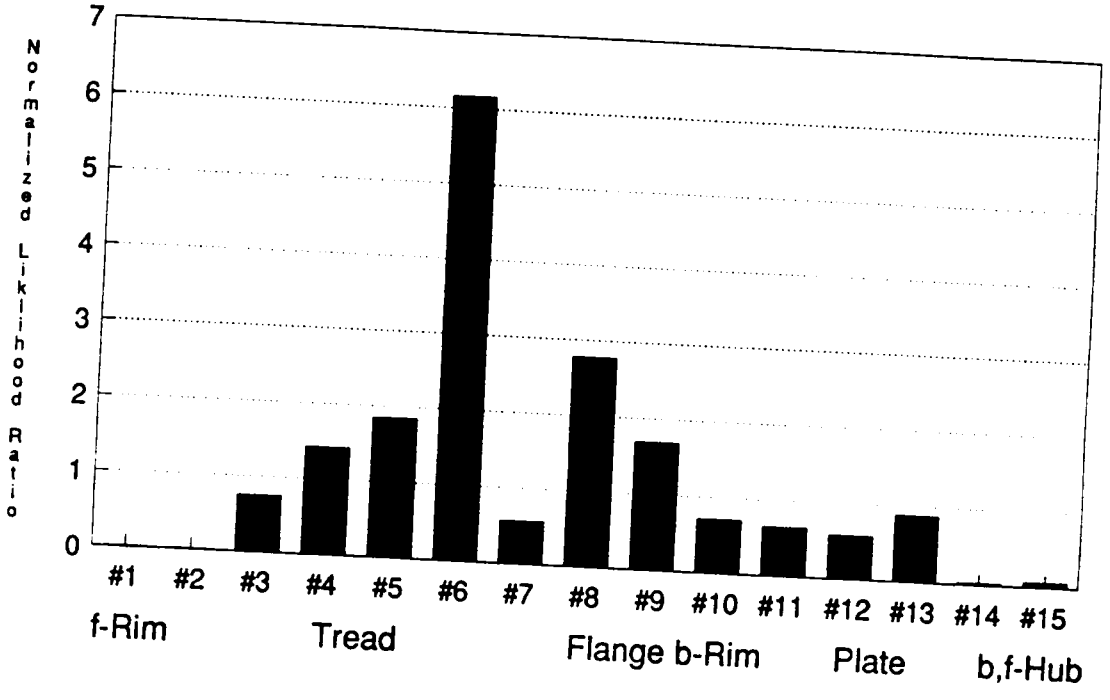

Figure 60. Normalized likelihood ratio, R, for circumferential normal stresses in normal wear and heat discolored wheels only.

these key locations. This result suggests a link between the state of surface stress in the wheel and the fracture mode.

It remains to be shown how the residual stress at these key locations varies with the service history, and whether or not a critical cut-off value of stress can be identified which differentiates "good" from "bad" wheels. The question of hot zones, a source of stress oscillation and deviations from azimuthal symmetry, is of great significance for any qualitative NDE characterization of wheels. The x-ray stress results indicate that heat-discolored (more than 4") wheels clearly show the most azimuthally asymmetry of residual stresses in the tread compared with new, normal wear, and heat-discolored (less than 4") wheels. This suggests that the heat-discolored (more than 4") wheel may posses hot zones. For the qualitative analysis of the azimuthal residual stresses, the variance test was used, which indicated that the variances of residual stress measurements on the tread of the six wheels were significantly related to the service history. Also, this may imply that hot zones are one of main causes of stress fluctuations. The variance statistic gives a possible discriminating procedure. However, we need to test a large population of wheels to obtain a reference variance as an index to discriminate wheels. In addition, more heat-discolored wheels need to be tested in order to see how strongly the residual stresses in azimuthal direction fluctuate from this measurement. This can only be accomplished through the measurements on the wheels with carefully controlled service histories such as could be accomplished on a dynamometer or perhaps on a unit train. Such tests are left to the future research program.

The least squares fitting using Fourier analysis (Figures 54-56) shows a periodicity of the residual stresses in the azimuthal direction for all of the wheels except for the cast, normal wear wheel. The new wheels (Wheels C and D), which were not machined, but in both cases as cast or wrought, shows that the mean stress is only about 50-60 % of that of used wheels and that the fluctuations are clearly manufacturing-process-related. One of the used wheels, a cast wheel (Wheels F), shows a very uniform stress distribution. On the other, the other used wheel (wrought, Wheel A) shows a $\pm$4.7 ksi oscillation with a periodicity of 1ωt (Table 4) around the mean of - 50 ksi. Considering the fact that these used wheels had seen only limited service, we would expect because of the 1ωt periodicity that the latter wheel was misaligned or unbalanced during service.

The heat-discolored (less than 4") wheel (Wheel B), which has several grooves on the tread, also shows a periodicity of $1\omega t$ around the mean of - 46 ksi with ± 4 ksi oscillation. This is not significantly different from Wheel A. We would attribute the oscillation to the same effects as for Wheel A. However, the heat-discolored (more than 4") wheel (Wheel E), which has a single groove on the tread, shows a periodicity of $2\omega t$ around the mean of - 54 ksi with ± 14 ksi oscillation. Note that not only is the periodicity of the stress in this work different from all other wheels, but the magnitude of the oscillation is approximately three times (3x) larger than those of the other wheels. Thus, the stress state of this wheel is clearly different from that of the other wheels. The periodicity of the stress in this overheat wheel cannot be accounted for by the effects suggested for the other wheels. Rather, it can be accounted for by either a non-uniform processing, off-center wheel (possibly in the curve), irregular application of the brake shoes to the wheel, uneven brake shoe contact with the wheel, or a locked wheel sliding on the rail during braking.

Because of the small statistical sample of wheels of varying service history available for this study, it is not possible to resolve many of the unanswered questions raised in the preceding analysis. However, it is unequivocal that:

- certain key locations in the wheels are more sensitive to changes in residual stress during service than are others
- we have identified at least two such key locations
- the residual stresses show an oscillatory pattern in the hoop direction around the wheels, and
- the magnitude of the oscillations is greatest for severely overheated wheels.

A detailed quantitative verification of these conclusions will require a major x-ray stress analysis effort on a much larger statistical sample of wheels of known and controlled service history.

It is recognized that the x-ray diffraction technique will cost much more than $7 per wheel to measure azimuthal fluctuation of stresses. The azimuthal fluctuation may be obtained supple-

mentally by a faster technique, such as the magnetoelastic or magnetacoustic techniques, since they take less than 1 minute at each location[38,39] compared with 5-10 minutes by x-ray diffaction.

7.0 PROPOSED NDT PROCEDURE

The results of the previous chapter indicate that key locations in the tread and on the rim of the flange are particularly sensitive to changes in residual stresses caused by overheating of railroad car wheels by dragging brakes. They also show that it is likely that fluctuations of the residual hoop stresses are excellent indicators of overheated wheels. These observations provide the basis for a potential new NDT procedure designed to discriminate overheated wheels.

Figure 61 shows a proposed flow chart for the discriminating procedure. Reference data will be collected from a large population of wheels of known service history using x-ray or some other technology. A critical variance value and the appropriate periodicity of these variations, which separate the good from bad wheels, will be obtained. Then, the circumferential residual stresses of an unknown wheel are measured at the critical location. The sample variance and periodicity is compared with the reference values. If the former is less than the latter, the wheel is expected to be good and reusable. Otherwise, it should be removed from the service.

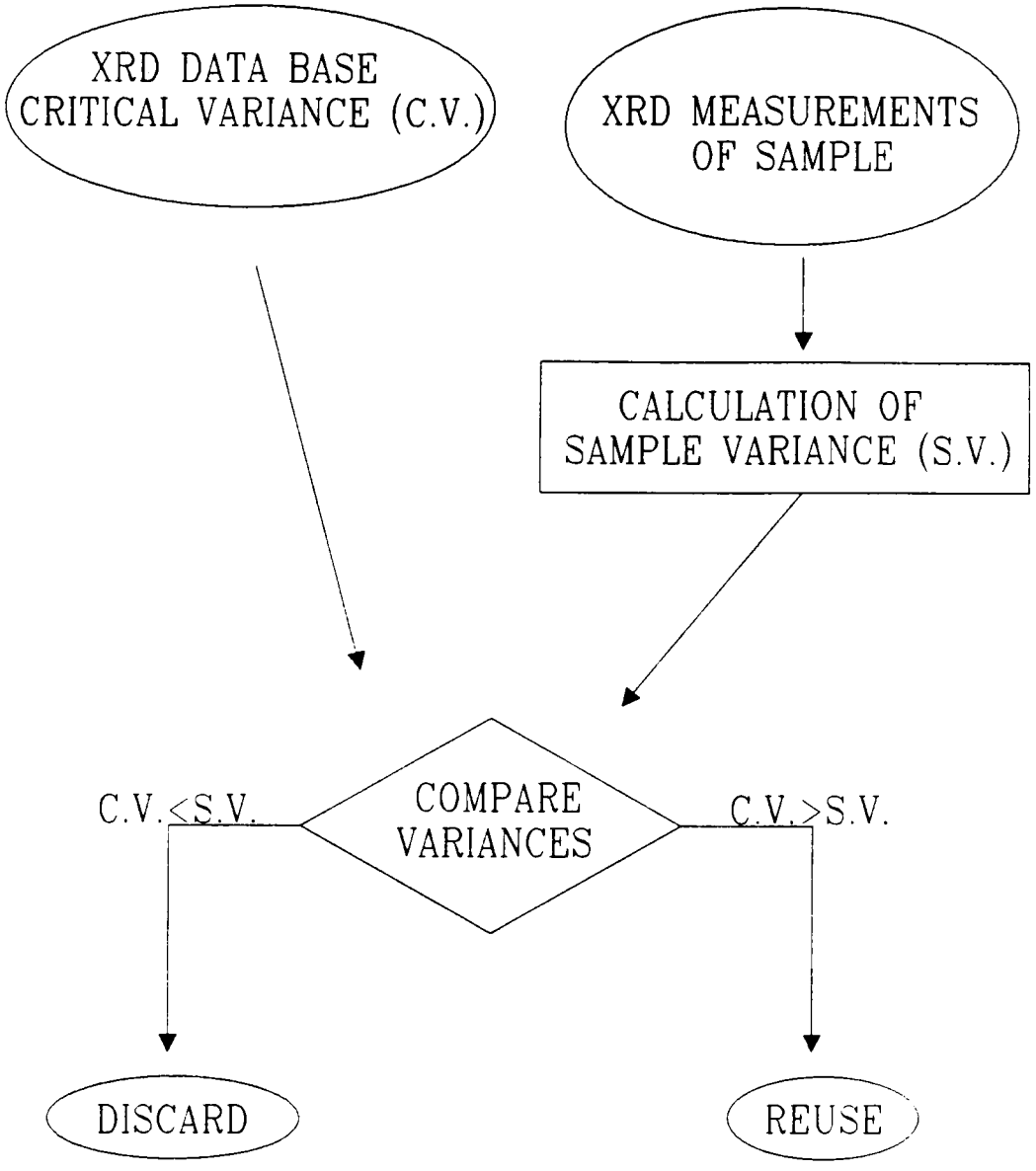

Figure 61. Proposed NDT procedure flow chart.

8.0 CONCLUSIONS

The research on railroad car wheels leads to the following important conclusions:

- This is the first time, to our knowledge, that x-ray diffraction has been successfully used to measure residual stresses in a wheel without sectioning the wheel. Normal and shear stresses can be quickly (less than 10 minutes for each measurement) and reliably ($\pm$4 ksi) obtained at most locations. The difference between the maximum and minimum normal stresses in azimuthal direction in the tread on two new wheels, two normal wear wheels, and the heat-discolored (less than 4") wheel is distributed within 25 ksi, whereas the difference in the heat-discolored (more than 4") wheel within 50 ksi. This implies the severe oscillation of normal stresses in the azimuthal direction of tread of the latter.

- Detailed measurements at a critical location on the tread of the severely overheated wheel indicates that the oscillating stresses vary sinusoidally around a mean compressive stress of - 50 ksi with an amplitude of $\pm$ 14 ksi.

- Hole drilling confirms x-ray diffraction residual stress analysis. The difference in residual stresses between two techniques is within the standard deviation, $\pm$5 ksi, for each measurement.

- Hole drilling shows a smooth stress variation with depth. This suggests that x-ray diffraction is applicable to wheels even though it measures stresses only in the near surface region(a few micrometers).

- At the 95% confidence limit, likelihood ratio tests have identified several key locations on the perimeter of a wheel at which the residual stress varies significantly with service history. The most sensitive of these locations is near the center of the tread where maximum pressure is expected to be applied by the braking mechanism. Other significant locations include the tip of the flange, the corner of the back rim, and the back plate. The key locations are consistent with those locations where crack initiation was observed in another AAR study.

- The identification of the key locations appears to be independent of the manufacture, geometry, or design of the wheel.

- The magnitude of statistical fluctuations in the circumferential residual stresses may be the key to identifying bad wheels.

- The circumferential residual stresses show an oscillatory pattern in the hoop direction around the wheels.

9.0 RECOMMENDATIONS

It is suggested that the residual stress at several of the key locations be measured by both x-ray diffraction and magnetoelastic or magnetoacoustic techniques as a function of controlled and known service history. The objective of such research would be; (i) to determine if there is a monotonic relationship between either the absolute value of the residual stress or the fluctuations and periodicities of the stresses with service history, and (ii) to determine if qualitative measurements of the stress fluctuation in the azimuthal direction in the tread of a wheel may be possible with magnetoeastic or magnetoacoustic techniques which are faster and less expensive than x-ray diffarction. In order to have maximum experimental control, it is believed that the first data should be acquired on a dynamometer, from several wheels (perhaps four) of differing designs and operated under different simulated braking thermal loads. Only after such carefully controlled experiments should more realistic, but less controlled, data be acquired from wheels in actual railroad service.

It is suggested that the six wheels characterized by x-rays in this study also be examined by saw cutting in order to develop a methodology for intercomparing the surface residual stresses sampled by x-rays and the bulk average stresses sampled by sawing.

10.0 REFERENCES

1. L. A. McClean, (personal communication, 1987), CSX Transportation Co, Baltimore, Maryland.

2. D. H. Stone, ***Wheel Failures Due To Brake Heating - Experience and Solutions***, Eighth International Wheelset Conference, Madrid, Spain (1985).

3. J. R. Barton, W. D. Perry, and R. K. Swanson, ***Heat-Discolored Wheels: Safe To Reuse?*** Progressive Railroading, (March 1985), pp.41-48.

4. D. H. Stone, (personal communication, 1987), AAR, Chicago, Illinois.

5. H. R. Wetenkamp and B. J. Eck, ***Wheel Damage Caused By Overheating***, Car Department Officers Association Annual Meeting, Chicago, (September 20, 1982).

6. B. J. Eck, ***Development of the Curved Plate Wheel Designs for More Severe Railroad Service***, ASME 85-WA/RT-5, (1985).

7. M. R. Johnson, R. E. Welch, and K. S. Yeung, ***Analysis of Thermal Stresses and Residual Changes in Railroad Wheels Caused Severe Drag Braking***, Tr. ASME, (February 1977), pp. 18 - 23.

8. H. R. Wetenkamp and R. M. Kipp, ***Thermal Damage and Rail Load Stresses in a 33-Inch Railroad Car Wheel***, ASME 77-WA/RT-2, (1977).

9. H. R. Wetenkamp and R. M. Kipp, ***Safe Thermal Loads***, Proc. Sixth International Wheelset Congress, Colorado Springs, (October 1978).

10. M. R. Johnson, R. R. Robinson, A. J. Opinsky, and D. H. Stone, ***Residual Stress Calculations on 33 Inch (838 mm) Diameter One-Wear Freight Car Wheels Under Simulated Unreleased Hand Brake Conditions***, ASME 82-WA/RT-11, (1982).

11. M. R. Johnson, R. R. Robinson, A. J. Opinsky, M. W. Joerms, and D. H. Stone, ***Calculation of Residual Stresses in Wheels From Saw Cut Displacement Data***, ASME (1985).

12. A. J. Opinsky, M. W. Joerms, D. H. Stone, and M. R. Johnson, ***Effect of Brake Shoe Position on the Development of Residual Stresses in Freight Car Wheels as a Result of Simulated Drag Braking***, ASME, 86-WA/RT-3 (1986).

13. H. R. Wetenkamp, B. J. Eck, and P. E. Rhine, ***The Influence of Brake Shoes on the Temperature of Wheels in Railroad Service***, Journal of Engineering for Industry, **102**(1), (1980) pp. 32 - 36.

14. J. D. Oliver, H. R. Wetenkamp, G. E. Dahlman, and B. J. Eck, ***Wheel and Brake Shoe Field Tests*** (1980), ASME 81-WA/RT-9, (1981).

15. J. Putukian (editor), ***Proc. Symp. on Nondestructive Measurement of Wheel/Axle Residual Stress***, Federal Railroad Administration, (June 1981).

16. D. H. Stone, (personnel communication, Nov. 14, 1988), AAR, Chicago, Illinois.

17. H. N. Jones, ***The Characterization of the Residual Stress State of Railroad Wheels by the Saw Cut Method***, ASME Rail Transp. Spring Conf. Proc., (April 1985), pp. 15 - 19.

18. B. R. Rajkumar and D. H. Stone, ***Measurement Approaches for Determining Thermally Induced Residual Stresses in Railroad Wheels***, ASME, 85-WA/RT-16 (1985).

19. R. L Pasley, ***Barkhausen Effect - An Indicator of Stress***, Materials Evaluation **28**(7), (1970), pp. 157 - 161.

20. ***Standard Method for Determining Residual Stresses by the Hole Drilling Strain-Gage Method***, Standard E 837 - 81, Annual Book of ASTM Standards, Vols. **03.01 and 12.02** (1981).

21. A. S. Babb, G. Birbeck, and B. Sweeney, ***Residual Stresses in Straight Webbed Monobloc Wheels***, Tokyo.

22. D. Utrata (personal communication, 1987).

23. M Namkung and J. S. Heyman, ***Residual Stress Characterization wutha Magetic/Ultrasonic Technique***, Proceedings of IEEE 1984 Ultrasonic Symposium, edited by B. R. McAvoy, **2**, Dallas, Texas (Nov. 1984) pp.950-954.

24. M Namkung, D. Ultrata, S. C. Allison, and and J. S. Heyman, ***Low-field Magnetoacoustic Residual Stress Measurements in Steel***, Solid Mechanics Research for QNDE, Northwestern University, Evanston, IL (Sep. 1985).

25. M Namkung, D. Ultrata, S. C. Allison, and and J. S. Heyman, ***Magnetoacoustic Stress Measurements in Steel***, Proceedings of IEEE 1985 Ultrasonic Symposium, edited by B. R. McAvoy, **2**, San Francisco, CA (Oct. 1985) pp.1022-1027.

26. D. Utrata and M. Namkung, ***Uniaxial Stress Effects on the Low-field Magnetoacoustic Interaction in Low and Medium Carbon Steels*** Review of Progress in Quantitative NDE, UCSD, LaJolla, CA (Aug. 1986).

27. M. Namkung, D. Ultrata, S. C. Allison, and and J. S. Heyman, ***Magnetoacoustic Stress Measurements in Steel***, Proceedings of IEEE 1987 Ultrasonic Symposium, edited by B. R. McAvoy, **2**, Denver, CO (Oct. 1987) pp.1061-1065.

28. M. Namkung, (personal communication, 1989).

29. P. R. Cheesewright, ***A Critical Review of Residual Stress Measurement in Rails***, Technical Note TN STM 15, British Railways Board, Research and Development Division, (September 1980).

30. M. R. James and J. B. Cohen, ***The Measurement of Residual Stresses by X-ray Diffraction Techniques***, in ***Treatise on Materials Science and Technology***; Vol. **19** (H. Herman, ed.), Academic Press: New York, (1980), pp.1 - 62.

31. I. C. Noyan and J. B. Cohen, ***Residual Stress: Measurement by Diffraction and Interpretation***, New York: Springer-Verlag, (1987).

32. M. R. James and J. B. Cohen, J. Testing Eval. **6**, (1978), pp. 91-97.

33. H. Dolle, J. of Appl. Cryst. Vol. **12**, (1979) pp.489-501.

34. C. S. Carter, R. G. Caton, and J. L. Guthrie, ***Fracture Resistance and Fatigue Crack Growth Characteristics of Railroad Wheels and Axles***, Department of Transportation Contract DOT-TSC 7, Final Report (April 1976).

35. A. J. Opinsky, ***Railroad Wheel Back Rim Face Failures II. Fracture Mechanics Calculations Based on Measured Crack Sizes***, Association of American Railroads Report R-507, AAR Technical Center, Chicago, Illinois (1982).

36. G. T. Gray III, A. W. Thompson and J. C. Williams, ***Influence of Microstructure on Fatigue Crack Initiation in Fully Pearlitic Steels***, Metall. Trans. A, **16A**, (1985) pp.753 - 760.

37. G. T. Gray III, A. W. Thompson, J. C. Williams, and D. H. Stone, ***The Effect of Microstructure on Fatigue Crack Propagation in Pearlitic Eutectoid Steels***, Can. Met. Quart., **21**, (1982) pp.73 - 78.

38. G. T. Gray III, J. C. Williams and A. W. Thompson, ***Toughness-Induced Crack Closure: An Explanation for Microstructurally Sensitive Fatigue Crack Growth***, Metall. Trans. A., **14A**, (1983) pp.421 - 433.

39. K, Titto and R. Fix, ***Evaluation of Residual Stresses, Grinding Burns and Heat Treat Defects Through Chrome Plating***, SAE Technical Paper Series 880877, (1988).

40. American Stress Technologies, ***Magnetoelastic Instrumentation for Testing of Residual Stresses: STRESSCAN 500C***, Information Bulletin S 500C-B.

41. N. J. Rendler and I. Vigness, ***On Hole-Drilling Strain-gage Method of Measuring Residual Stresses*** , Experimental Mechanics, **6**, (Dec. 1966), pp.577 - 586.

42. J. P. Sandifer and G. E. Bowie, ***Residual Stress by Blind-hole Method with Off-center Hole*** , Experimental Mechanics, **18** (May 1966), pp. 173 - 179.

43. M. T. Flaman, ***Brief Investigation of Induced Drilling Stress in the Center Hole Method of Residual Stress Measurements***, Experimental Mechanics, **22**, (1982) p.22-30.

44. ***Measurement of Residual Stresses by the Hole Drilling Strain-Gage Method: Measurement Group Tech Note TN503-3***, Measurement Group Inc. Raleigh, NC (1988).

45. IBM, trademark of International Business Machines Corporation.

46. ABSTAT, product of Anderson-Bell Corp. Parker, Colorado 80314.

47. SAS, product of SAS Institute Inc. Cary, North Carolinar 27511-8000.

48. R. W. Hendricks, private communication, (1989).

49. H. Zantopulos and C. F. Jatczak, Adv. X-ray Analysis, **14**, (1970) pp.360-376.

50. C. F. Jatczak and H. H. Boehm, Adv. X-ray Analysis, **17**, (1973) pp.354-370.

51. M. R. James, ***An Examination of Experimental Techniques in X-Ray Residual Stress Analysis.*** Ph.D. Thesis, Northwestern Univ., Evanston, Illinois, (1977).

52. M. R. James and J. B. Cohen, ***J. Appl. Cryst.*** **12**,(1979) pp.339-345.

53. E. B. S. Pardue and M. R. James, ***Second International Conference on Residual Stress (ICRS-2)***. Nancy, France. Plenum, (1988).

54. E. B. S. Pardue, R. W. Hendricks, and M. R. James, Adv. X-Ray Analysis, **31**, (1988) pp.205-212.

55. Hendricks, R.W. and Jo, J. ***Second International Conference on Residual Stress (ICRS-2)***. Nancy, France. Plenum, (1989).

56. C, F, Dehan, ***An Intelligent Workstation For Reliable Residual Stress Determination Using X-ray Diffraction***, M.S. Thesis, Virginia Polytechnic Institute and State University, Blacksburg, Virginia, (July 1989) page 82.

57. Original photos courtesy to Tchnology for Energy Corporation, One Energy Center, Lexington Drive, Knoxville, Tennessee, 37933-0996.

58. R. W. Hendricks, ***One-and Two-Dimensional Position-Sensitive X-Ray and Neutron Detectors***, Tr. Am. Crystallogr. Assoc. **12**, (1976) pp.103-146.

59. B. N. Ranganathan, J. J. Wert, and W. N. Clotfelter, ***Reference of X-Ray Elastic Content*** J. Test. Evaluation **4**, (1976) pp.218-219.

60. ***TEC Model 1600 X-ray Stress Analysis System Operation and Maintenance Manual***, Technology for Energy Corp., Knoxville, TN, (1985).

61. I. S. Sokolonikoff, ***Mathematical Theory of Elasticity***, 2nd ed., McGraw Hill, New York, (1956).

62. S. P. Timoshenco and J. N. Goodier, ***Theory of Elasticity***, 3rd ed., New York; McGraw Hill, (1970)

63. D. Frederick and T. Chang, ***Continuum Mechanics***. Cambridge, Scientific Publishers, (1972).

64. G. S. Schjar, ***Application of Finite Element Calculations to Residual Stress Measurements*** J. of Engr. Mat. and Tech., **103**, (1981) pp.157-163.

65. W. E. Nicola, ***Practical Subsurface Residual Stress Evaluation by the Hole Drilling Method***, Proc. 5th International Congress on Experimental Mechanics, Brookfield Center, Connecticut: Society for Experimental Mechanics (1984).

66. ***Lotus 1-2-3, product of Lotus Development Corp.***, (1985).

67. J. W. Dally and W. F. Rily, ***Experimental Stress Analysis***, 2nd ed., McGraw Hill, New York, (1978).

68. ***Instruction Bulletin B-127-9: Surface Preparation for strain gage bonding***, Measurement Group, Inc., Raleigh, NC. (1976).

69. ***Instruction Manual: P-3500 Digital Strain Indicator***, Measurement Group, Inc., Raleigh, NC.

70. ***Instruction Manual: B-10 Switch and Balance Unit***, Measurement Group, Inc., Raleigh, NC. (1983).

71. ***Instruction Manual of Model RS-200 Milling Guide***, Measurement Group, Inc., Raleigh, NC.

72. C. L. Chow, and C. H. Cundiff, ***On Residual stress Measurements in Light Truck Wheels Using the Hole-Drilling Method*** , Experimental Mechanics, (March 1985), pp. 54 - 59.

73. J. Lu and J. F. Flavenot, ***Trials in Increasing the Precision of the Incremental Hole Drilling Method Residual Stress Distribution Determination***, Residual Stresses in Science and Technology, edited by E. Macherauch and V. Hauk, Vol. 2, DGM Informationsgesellschaft. Verlag, (1987), pp.215 - 222.

74. H. Hausler, G. Konig, and H. Kockelmann, ***On the Accuracy of Determining the Variation with Depth of Residual Stresses by Means of the Hole Drilling Method***, Residual Stresses in

Science and Technology, edited by E. Macherauch and V. Hauk, Vol. 2, DGM Informationsgesellschaft. Verlag, (1987), pp.257 - 265.

75. Supplied by CSX Transportation Co. Baltimore, Maryland.

76. J. M. Wandrisco and F. J. Dewez, ***Service Defects in Tread of Railroad Wheels*** ASME Paper 60-RR-1, (1960).

77. ASTM, ***Standard Test Methods for determining Average Grain Sizes***, ASTM Designation E 112-88, Annual Book of ASTM Standards, Vol. 03.01 (1989), pp284-309.

78. G. F. Vander Voort, ***Metallograpghy : Principles and Practice***, 2nd ed. New York, MacGraw Hill, (1984).

79. N. Ridley, ***A Review of the Data on the Interlamella Spacing of Pearlite***, Met. Trans. A., 15A, (June 1984), pp1019-1036.

80. L. Dillinger, ***Met-Tips : Hardness Testing***, LECO Corp. (1984).

81. M. Wheeler, personal communication, Norfolk Southern Corp. Roanoke, Virginia, (1989).

82. H. J. Schrader, ***The Friction of Railway Brake Shoes at High Speeds and High Pressure*** University of Illinois Engineering Station Bulletin No. 301, (May 1938).

83. ***The Making, Shaping, and Treating of Steel***, 9th Ed. edited by H. E. McGannon, United States Steel, Pittsburg, Herbick & Held, (1971).

84. Supplied by B. Mills and M. Flaman, Ontario Hydro Research Division, Toronto, Ontario, Canada.

85. P. J. Bickel and K. A. Doksum, ***Mathematic Statistics: Basic Ideas and Selected Topics***, Oakland: Holden-Day (1977).

86. Y. J. Jung, ***Statistics: Theory and Application***, Seoul: Bojin, (1963).

87. C. T. Clark and L. L. Schkade, ***Statistical Analysis for Administrative Decisions***, 3rd Ed. Cincinnati, South-Western Publ. (1979).

11.0 APPENDEX A

11.1 DIFFRACTOMETER MISALIGNMENT ERRORS IN X-RAY RESIDUAL STRESS MEASUREMENTS

This section describes the derivation of Equations (3-7) to (3-10) in Section 3.1.3, Effect of Sample Misalignment, and also discusses other special cases of misalignmnet. It is a preprint of a paper submitted to the Journal of Applied Crystallography for publication.

DIFFRACTOMETER MISALIGNMENT ERRORS IN X-RAY RESIDUAL STRESS MEASUREMENTS

Abstract

Misalignment of the the x-ray diffractometer can lead to significant errors in the stress measured by x-ray diffactometry. A generalized equation is derived for the relationship between the crystal lattice d-spacing and the stress tensor which involves the $\Delta\psi$ and $\Delta\chi$ misalignments of the diffractometer as well as large χ-angle tilts and ϕ-angle rotations. Inclusion of the ϕ and χ rotations allows for measurements with complicated sample geometries as well as for a direct comparison of the χ and ψ geometry diffractometers in common use. In the case of no misalignment errors ($\Delta\chi$, $\Delta\psi = 0$), the symmetries between the classical ψ-tilt and χ-tilt diffractometers are clearly shown. The generalized equation is reduced to more manageable forms for several approximations in which the misalignments are small. How these errors affect the computation of shear and normal stresses is also discussed. Finally, determination of residual stresses in more complicated sample geometries is discussed.

Introduction

Errors in the determination of residual stresses as determined by x-ray diffractometry may result from many sources and may be broadly classified into three groups : instrumental, geometrical, and material [Jatczak & Boehm, 1973; James, 1977; Noyan & Cohen, 1987]. Diffractomer misalignments, an instrumental source of error, may be induced by sample displacement, ψ axis missetting in the plane of the incident and diffracted x-ray beams, specimen curvature, and the deviation of the true zero position of ψ [Zantopulos & Jatczak, 1970; Jatczak & Boehm, 1973; James, 1977; James & Cohen, 1979; Noyan & Cohen, 1987; Pardue, Hendricks & James, 1988; Hendricks & Jo, 1988; Pardue & James, 1988]. In addition, it is possible that misalignment errors may result from a rotation of the diffractometer in the plane perpendicular to the ψ axis either by the misalignment of the specimen and/or instrument by an amount $\Delta\chi$ or because of a deliberate tilt of the diffractometer by an angle χ. In this paper, the general equation of the stress measurement for a specimen which is rotated through angles ψ, $\Delta\psi$, χ, $\Delta\chi$ and ϕ with respect to the x-ray diffractometer is derived. To our knowledge, this is the first complete presentation of a generalized relationship which involves all possible tilts and misalignments of the diffractometer. Unfortunately, the final result is very long and tedious. In the following sections of the paper, several special cases are considered in which the complexity of the general result can be substantially reduced. Finally, the effects of misalignment $\Delta\psi$ and $\Delta\chi$ on the evaluation of stresses are considered. The importance of these errors is illustrated with a numerical example.

Generalized Equation for Stress Determination in a Specimen Which is Rotated through ψ, $\Delta\psi$, χ, $\Delta\chi$, and ϕ Angles

1. *Assumptions*

In order to derive the equations for stress determination, the following assumptions and conditions are employed [Zantopulos & Jatczak, 1970; Frederick & Chang, 1972; Noyan & Cohen, 1987]:

1. the specimen is isotropic, homogeneous, and elastic,
2. the specimen has a statistically random orientation of numerous fine grains,

3. the shear strains and stresses are symmetric so that $\sigma_{12} = \sigma_{21}$, $\sigma_{13} = \sigma_{31}$, and $\sigma_{23} = \sigma_{32}$,
4. no x-ray focusing aberrations are involved, and
5. there are no deviations in the 2θ diffraction angle caused by microstrain or faulted structures.

In this paper we consider only diffractometer angular misalignment errors. The problems associated with preferred orientation and/or inhomogeneous distribution of elastic strain (failure of assumptions 1 and 2) are extremely complex. They have been treated under a variety of assumptions by Marion and Cohen (1975), Dölle and Hauk (1978), Lode and Pieter (1977;1981), and Barral et al (1987). A review of the work prior to 1987 is found in Appendix B of Noyan and Cohen (1987). The role of errors introduced by the failure of assumptions 4 and 5 have been thoroughly treated by James (1977) and James & Cohen (1979) and reviewed by Noyan and Cohen (1988).

2. *Derivation of the Strain Equations*

The generalized equation for x-ray stress determination for the rotations of ψ, $\Delta\psi$, χ, $\Delta\chi$, and ϕ is derived through three basic equations of material science and the mechanics of materials : a Cartesian coordinate system transformation law, Hooke's law, and the strain-deformation relationship. In this derivation, ψ is the tilt of the diffractometer in the plane of the incident and diffracted x-ray beams, χ is the tilt of the diffractometer perpendicular to the incident and diffracted beam, and ϕ is the rotation of the diffractometer about the normal to the sample surface and an arbitrary definition of the coordinate system.[1] The transformation law is used to express the strain tensor in the laboratory coordinate system, ($\mathbf{x}^v$ in Figure 1), in terms of the strain tensor in the specimen coordinate system, ($\mathbf{x}^i$ in Figure 1). As will be seen shortly, because there are five distinct rotations of the diffractometer with respect to the sample which must be accounted for, we will use a lower case Roman numeral primed notation to denote each successive tilt. The transformation of the strain tensor from one coordinate system (unprimed) to another system (primed) is defined by [Frederick and Chang, 1972] as

---

[1] This notation follows that of Noyan and Cohen (1987). Other notations are in use elsewhere in the literature. The reader is cautioned that in some cases symbols used by us are used by others to denote different angles [e.g. Macherauch and Wolfstieg (1977) and Wagner et al (1982).]

$$\varepsilon'_{ij} = a_{lm}a_{jn}\varepsilon_{mn} \tag{1}$$

where

ε'_{ij} = the strain tensor in the primed coordinate system,

ε_{ij} = the strain tensor in the unprimed coordinate system, and

a_{lm}, a_{jn} = the direction cosines between two coordinate systems.

The components of the strain tensor can be obtained by expanding Equation (1) as follows :

$$\begin{aligned}
\varepsilon'_{11} &= a_{1m}a_{1n}\varepsilon_{mn} \\
&= a_{11}a_{1n}\varepsilon_{1n} + a_{12}a_{1n}\varepsilon_{2n} + a_{13}a_{1n}\varepsilon_{3n} \\
&= a_{11}a_{11}\varepsilon_{11} + a_{12}a_{11}\varepsilon_{21} + a_{13}a_{11}\varepsilon_{31} \\
&\quad + a_{11}a_{12}\varepsilon_{12} + a_{12}a_{12}\varepsilon_{22} + a_{13}a_{12}\varepsilon_{32} \\
&\quad + a_{11}a_{13}\varepsilon_{13} + a_{12}a_{13}\varepsilon_{23} + a_{13}a_{13}\varepsilon_{33} \\
\varepsilon'_{12} &= a_{11}a_{21}\varepsilon_{11} + \quad . \quad . \quad . \\
. \; . &= \quad . \quad . \quad . \quad . \quad . \quad . \\
. \; . &= \quad . \quad . \quad . \quad . \quad . \quad .
\end{aligned}$$

All of the tensor components can be grouped and rearranged in a matrix form as

$$\begin{bmatrix} \varepsilon'_{11} & \varepsilon'_{12} & \varepsilon'_{13} \\ \varepsilon'_{21} & \varepsilon'_{22} & \varepsilon'_{23} \\ \varepsilon'_{31} & \varepsilon'_{32} & \varepsilon'_{33} \end{bmatrix} = \begin{bmatrix} a_{11} & a_{12} & a_{13} \\ a_{21} & a_{22} & a_{23} \\ a_{31} & a_{32} & a_{33} \end{bmatrix} \begin{bmatrix} \varepsilon_{11} & \varepsilon_{12} & \varepsilon_{13} \\ \varepsilon_{21} & \varepsilon_{22} & \varepsilon_{23} \\ \varepsilon_{31} & \varepsilon_{32} & \varepsilon_{33} \end{bmatrix} \begin{bmatrix} a_{11} & a_{21} & a_{31} \\ a_{12} & a_{22} & a_{32} \\ a_{13} & a_{23} & a_{33} \end{bmatrix}$$

or

$$\varepsilon' = \mathbf{A}_x \varepsilon \mathbf{A}_x^T \tag{2}$$

where $\mathbf{A}_x^T$ is the transpose of $\mathbf{A}_x$.

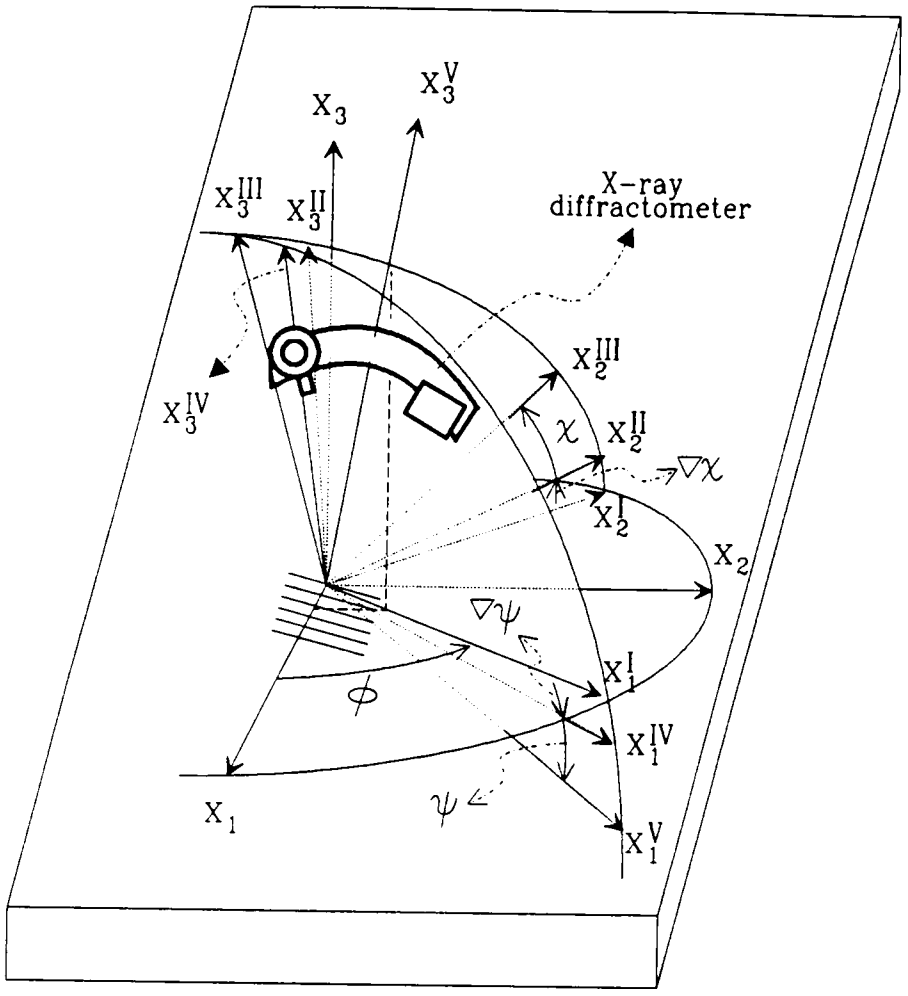

Figure 1. Transformation of the coordinate system from sample coordinates (x_1, x_2, x_3) to diffractometer coordinates (x_1^V, x_2^V, x_3^V). The diffractometer moves in the plane defined by (x_1^V, x_3^V) and rotates about the x_2^V axis. The diffraction vector lies along x_3^V. If a coordinate vector is not shown, it is colinear with the previous vector of next lower Roman superscript and has been left out for clarity. The sequence of rotations are as follows: $\mathbf{x} \rightarrow \mathbf{x}^I$ by a rotation ϕ about x_3; $\mathbf{x}^I \rightarrow \mathbf{x}^{II}$ by a misalignment rotation $\Delta\chi$ about x_1^I; $\mathbf{x}^{II} \rightarrow \mathbf{x}^{III}$ by a tilt of the diffractometer, χ, about $x_1^I (= x_1^{II})$; $\mathbf{x}^{III} \rightarrow \mathbf{x}^{IV}$ by a misalignment rotation $\Delta\psi$ about x_2^{III}; and $\mathbf{x}^{IV} \rightarrow \mathbf{x}^V$ by a tilt of the diffractometer, ψ, about $x_2^{IV} (= x_2^{III})$.

With the same idea as above, the strain tensor for each coordinate transformation can be written in the following simplified matrix form. First, the rotation of the coordinate system by ϕ around x_3 (See Figure 1) gives

$$\varepsilon_\phi = A_\phi \varepsilon_s A_\phi^T \tag{3}$$

where ε_ϕ is the strain tensor in the x^I coordinate system, ε_s is the strain tensor in the x (sample) coordinate system, and

$$A_\phi = \begin{bmatrix} C\phi & S\phi & 0 \\ -S\phi & C\phi & 0 \\ 0 & 0 & 1 \end{bmatrix} . \tag{4}$$

In Equation (4) and in all following equations, C and S are a shorthand representation for the cosine and sine functions, respectively. ($C\phi = \cos\phi$; $S\phi = \sin\phi$) The rotation of the x^I coordinate system by $\Delta\chi$ around x_1^I gives

$$\varepsilon_{\Delta\chi} = A_{\Delta\chi} \varepsilon_\phi A_{\Delta\chi}^T \tag{5}$$

where $\varepsilon_{\Delta\chi}$ is the strain tensor in the x^{II} coordinate system and

$$A_{\Delta\chi} = \begin{bmatrix} 1 & 0 & 0 \\ 0 & C\Delta\chi & S\Delta\chi \\ 0 & -S\Delta\chi & C\Delta\chi \end{bmatrix} . \tag{6}$$

The rotation of the x^{II} coordinate system by χ around x_1^I gives

$$\varepsilon_\chi = A_\chi \varepsilon_{\Delta\chi} A_\chi^T \tag{7}$$

where ε_χ is the strain tensor in the x^{III} coordinate system and

$$A_\chi = \begin{bmatrix} 1 & 0 & 0 \\ 0 & C\chi & S\chi \\ 0 & -S\chi & C\chi \end{bmatrix} . \tag{8}$$

At this point, it is important to note that we have separated a misalignment error ($\Delta\chi$) from a deliberate tilt (χ) to allow us to examine these effects separately. We will similarly separate the $\Delta\psi$ error and deliberate ψ tilts in the following two rotations. The rotation of the x^{III} coordinate system by $\Delta\psi$ around x_2^{III} gives

$$\varepsilon_{\Delta\psi} = \mathbf{A}_{\Delta\psi}\varepsilon_{\chi}\mathbf{A}_{\Delta\psi}^{T} \tag{9}$$

where $\varepsilon_{\Delta\psi}$ is the strain tensor in the $\mathbf{x}^{IV}$ coordinate system and

$$\mathbf{A}_{\Delta\psi} = \begin{bmatrix} C\Delta\psi & 0 & -S\Delta\psi \\ 0 & 1 & 0 \\ S\Delta\psi & 0 & C\Delta\psi \end{bmatrix} . \tag{10}$$

Finally, the rotation of the x^{IV} coordinate system by ψ around x_1^{III} gives

$$\varepsilon_{\psi} = \mathbf{A}_{\psi}\varepsilon_{\Delta\psi}\mathbf{A}_{\psi}^{T} \tag{11}$$

where ε_{ψ} is the strain tensor in the $\mathbf{x}^{V}$ (laboratory) coordinate system and

$$\mathbf{A}_{\psi} = \begin{bmatrix} C\psi & 0 & -S\psi \\ 0 & 1 & 0 \\ S\psi & 0 & C\psi \end{bmatrix} . \tag{12}$$

Inserting Equations (3), (5), (7) and (9) into Equation (11) yields

$$\varepsilon_{\psi} = \mathbf{A}_{\psi}\mathbf{A}_{\Delta\psi}\mathbf{A}_{\chi}\mathbf{A}_{\Delta\chi}\mathbf{A}_{\phi}\varepsilon_{s}\mathbf{A}_{\phi}^{T}\mathbf{A}_{\Delta\chi}^{T}\mathbf{A}_{\chi}^{T}\mathbf{A}_{\Delta\psi}^{T}\mathbf{A}_{\psi}^{T} . \tag{13}$$

With the transpose property and associative law of matrix multiplication [Wylie & Barrett, 1982], Equation (13) can be converted to

$$\varepsilon_{\psi} = \mathbf{A}_{\psi}\mathbf{A}_{\Delta\psi}\mathbf{A}_{\chi}\mathbf{A}_{\Delta\chi}\mathbf{A}_{\phi}\varepsilon_{s}[\mathbf{A}_{\psi}\mathbf{A}_{\Delta\psi}\mathbf{A}_{\chi}\mathbf{A}_{\Delta\chi}\mathbf{A}_{\phi}]^{T} \tag{14}$$

or

$$\varepsilon_{\psi} = \mathbf{A}\varepsilon_{s}\mathbf{A}^{T} \tag{15}$$

where

$$\mathbf{A} = \mathbf{A}_{\psi}\mathbf{A}_{\Delta\psi}\mathbf{A}_{\chi}\mathbf{A}_{\Delta\chi}\mathbf{A}_{\phi} = \begin{bmatrix} A_{11} & A_{12} & A_{13} \\ A_{21} & A_{22} & A_{23} \\ A_{31} & A_{32} & A_{33} \end{bmatrix} .$$

Since the x-ray diffractometer measures only shifts in d-spacings in the planes perpendicular to the diffraction vector and since the coordinate systems have been defined such that the diffraction vector lies along x_3^{V}, we need only ε_{33} from Equation (15)

for the x-ray stress measurement. Expanding Equation (15), the strain along x_3^V is

$$\varepsilon_{33,\psi\,\Delta\psi\,\chi\,\Delta\chi\,\phi} = A_{31}^2\varepsilon_{11} + A_{32}^2\varepsilon_{22} + A_{33}^2\varepsilon_{33} + 2A_{32}A_{31}\varepsilon_{21} + 2A_{33}A_{31}\varepsilon_{31} + 2A_{33}A_{32}\varepsilon_{32} \quad . \tag{16}$$

Using Equations (5) through (15), Equation (16) can be expanded to

$$\begin{aligned}
\varepsilon_{33,\psi\,\Delta\psi\,\chi\,\Delta\chi\,\phi} = \varepsilon_{11}(& \sin^2\psi\cos^2\Delta\psi\cos^2\phi + \cos^2\psi\sin^2\Delta\psi\cos^2\phi \\
& + \sin^2\psi\sin^2\Delta\psi\sin^2\chi\cos^2\Delta\chi\sin^2\phi + \cos^2\psi\cos^2\Delta\psi\sin^2\chi\cos^2\Delta\chi\sin^2\phi \\
& + \sin^2\psi\sin^2\Delta\psi\cos^2\chi\sin^2\Delta\chi\sin^2\phi + \cos^2\psi\cos^2\Delta\psi\cos^2\chi\sin^2\Delta\chi\sin^2\phi \\
& - 2\sin^2\psi\,C\Delta\psi\,S\Delta\psi\,S\chi\,C\Delta\chi\,S\phi\,C\phi - 2\sin^2\psi\,C\Delta\psi\,S\Delta\psi\,C\chi\,S\Delta\chi\,S\phi\,C\phi \\
& + 2\cos^2\psi\,S\Delta\psi\,C\Delta\psi\,S\chi\,C\Delta\chi\,C\phi\,S\phi + 2\cos^2\psi\,S\Delta\psi\,C\Delta\psi\,C\chi\,S\Delta\chi\,C\phi\,S\phi \\
& + 2\sin^2\psi\sin^2\Delta\psi\,S\chi\,C\chi\,C\Delta\chi\,S\Delta\chi\sin^2\phi + 2\cos^2\psi\cos^2\Delta\psi S\chi C\chi C\Delta\chi\,S\Delta\chi\sin^2\phi \\
& + 2\,S\psi\,C\psi\,C\Delta\psi\,S\Delta\psi\cos^2\phi + 2\,S\psi\,C\psi\cos^2\Delta\psi\,S\chi\,C\Delta\chi\,C\phi\,S\phi \\
& + 2\,S\psi\,C\psi\cos^2\Delta\psi\,C\chi\,S\Delta\chi\,C\phi\,S\phi - 2\,C\psi\,S\psi\sin^2\Delta\psi\,S\chi\,C\Delta\chi\,C\phi\,S\phi \\
& - 2\,C\psi\,S\psi\sin^2\Delta\psi\,C\chi\,S\Delta\chi\,C\phi\,S\phi - 2\,S\psi\,C\psi\,S\Delta\psi\,C\Delta\psi\sin^2\chi\cos^2\Delta\chi\sin^2\phi \\
& - 4\,C\psi\,S\psi\,C\Delta\psi\,S\Delta\psi\,S\chi\,C\chi\,C\Delta\chi\,S\Delta\chi\sin^2\phi \\
& - 2\,S\psi\,C\psi\,S\Delta\psi\,C\Delta\psi\,\cos^2\chi\sin^2\Delta\chi\sin^2\phi) \\
+ \varepsilon_{22}(& \sin^2\psi\cos^2\Delta\psi\sin^2\phi + \cos^2\psi\sin^2\Delta\psi\sin^2\phi \\
& + \sin^2\psi\sin^2\Delta\psi\sin^2\chi\cos^2\Delta\chi\cos^2\phi + \cos^2\psi\cos^2\Delta\psi\sin^2\chi\cos^2\Delta\chi\cos^2\phi \\
& + \sin^2\psi\sin^2\Delta\psi\cos^2\chi\sin^2\Delta\chi\cos^2\phi + \cos^2\psi\cos^2\Delta\psi\cos^2\chi\sin^2\Delta\chi\cos^2\phi \\
& + 2\sin^2\psi C\Delta\psi S\Delta\psi\,S\chi C\Delta\chi\,S\phi\,C\phi + 2\sin^2\psi C\Delta\psi S\Delta\psi C\chi S\Delta\chi S\phi\,C\phi \\
& - 2\cos^2\psi S\Delta\psi\,C\Delta\psi\,S\chi\,C\Delta\chi S\phi C\phi - 2\cos^2\psi S\Delta\psi\,C\Delta\psi\,C\chi\,S\Delta\chi S\phi C\phi \\
& + 2\sin^2\psi\sin^2\Delta\psi\,S\chi\,C\chi C\Delta\chi S\Delta\chi\cos^2\phi + 2\cos^2\psi\cos^2\Delta\psi S\chi C\chi C\Delta\chi S\Delta\chi\cos^2\phi \\
& + 2\,S\psi\,C\psi C\Delta\psi S\Delta\psi\sin^2\phi - 2\,S\psi\,C\psi\cos^2\Delta\psi S\chi C\Delta\chi\,S\phi\,C\phi \\
& - 2\,S\psi C\psi\cos^2\Delta\psi\,C\chi\,S\Delta\chi\,S\phi C\phi + 2\,C\psi\,S\psi\sin^2\Delta\psi S\chi C\Delta\chi\,S\phi\,C\phi
\end{aligned}$$

$$+ 2\,C\psi S\psi \sin^2\Delta\psi C\chi S\Delta\chi\, S\phi\, C\phi - 2\,S\psi\, C\psi S\Delta\psi C\Delta\psi \sin^2\chi \cos^2\Delta\chi \cos^2\phi$$

$$- 4\,S\psi\, C\psi S\Delta\psi C\Delta\psi\, S\chi\, C\chi C\Delta\chi S\Delta\chi \cos^2\phi - 2S\psi C\psi\, S\Delta\psi C\Delta\psi \cos^2\chi \sin^2\Delta\chi \cos^2\phi)$$

$$+ \varepsilon_{33}(\sin^2\psi \sin^2\Delta\psi \sin^2\chi \sin^2\Delta\chi + \cos^2\psi \cos^2\Delta\psi \sin^2\chi \sin^2\Delta\chi$$

$$+ \sin^2\psi \sin^2\Delta\psi \cos^2\chi \cos^2\Delta\chi + \cos^2\psi \cos^2\Delta\psi \cos^2\Delta\psi \cos^2\chi \cos^2\Delta\chi$$

$$- 2 \sin^2\psi \sin^2\Delta\psi\, S\chi\, C\chi S\Delta\chi C\Delta\chi - 2 \cos^2\psi \cos^2\Delta\psi S\chi C\chi S\Delta\chi C\Delta\chi$$

$$- 2\,S\psi C\psi S\Delta\psi C\Delta\psi \sin^2\chi \sin^2\Delta\chi + 4\,S\psi C\psi S\Delta\psi C\Delta\psi S\chi C\chi\, S\Delta\chi C\Delta\chi$$

$$- 2\,S\psi C\psi S\Delta\psi C\Delta\psi \cos^2\chi \cos^2\Delta\chi)$$

$$+ 2\varepsilon_{12} (\sin^2\psi \cos^2\Delta\psi\, S\phi\, C\phi - \sin^2\psi C\Delta\psi S\Delta\psi\, S\chi C\Delta\chi \sin^2\phi$$

$$- \sin^2\psi C\Delta\psi S\Delta\psi C\chi S\Delta\chi \sin^2\phi + \cos^2\psi \sin^2\Delta\psi S\phi C\phi$$

$$+ \cos^2\psi S\Delta\psi C\Delta\psi S\chi C\Delta\chi \sin^2\phi + \cos^2\psi S\Delta\psi C\Delta\psi C\chi S\Delta\chi \sin^2\phi$$

$$+ \sin^2\psi S\Delta\psi C\Delta\psi S\chi C\Delta\chi \cos^2\phi - \sin^2\psi \sin^2\Delta\psi \sin^2\chi \cos^2\Delta\chi C\phi\, S\phi$$

$$- 2 \sin^2\psi \sin^2\Delta\psi S\chi C\chi C\Delta\chi S\Delta\chi C\phi\, S\phi - \cos^2\psi C\Delta\psi S\Delta\psi S\chi C\Delta\chi \cos^2\phi$$

$$- \cos^2\psi \cos^2\Delta\psi \sin^2\chi \cos^2\Delta\chi C\phi S\phi - 2 \cos^2\psi \cos^2\Delta\psi S\chi C\chi C\Delta\chi S\Delta\chi C\phi S\phi$$

$$+ \sin^2\psi S\Delta\psi C\Delta\psi C\chi S\Delta\chi \cos^2\phi - \sin^2\psi \sin^2\Delta\psi \cos^2\chi \sin^2\Delta\chi C\phi S\phi$$

$$- \cos^2\psi C\Delta\psi S\Delta\psi C\chi S\Delta\chi \cos^2\phi - \cos^2\psi \cos^2\Delta\psi \cos^2\chi \sin^2\Delta\chi C\phi S\phi$$

$$+ 2\,S\psi C\psi C\Delta\psi S\Delta\psi S\phi C\phi + S\psi C\psi \cos^2\Delta\psi S\chi C\Delta\chi \sin^2\phi$$

$$+ S\psi C\psi \cos^2\Delta\psi C\chi S\Delta\chi \sin^2\phi - C\psi S\psi \sin^2\Delta\psi S\chi C\Delta\chi \sin^2\phi$$

$$- C\psi S\psi \sin^2\Delta\psi C\chi S\Delta\chi \sin^2\phi + S\psi C\psi \sin^2\Delta\psi S\chi C\Delta\chi \cos^2\phi$$

$$+ S\psi C\psi S\Delta\psi C\Delta\psi \sin^2\chi \cos^2\Delta\chi C\phi S\phi + 4\,S\psi C\psi S\Delta\psi C\Delta\psi S\chi C\chi C\Delta\chi S\Delta\chi C\phi S\phi$$

$$- C\psi S\psi \cos^2\Delta\psi S\chi C\Delta\chi \cos^2\phi + C\psi S\psi C\Delta\psi S\Delta\psi \sin^2\chi \cos^2\Delta\chi C\phi S\phi$$

$$+ S\psi C\psi \sin^2\Delta\psi C\chi S\Delta\chi \cos^2\phi$$

$$+ 2\,S\psi C\psi S\Delta\psi C\Delta\psi \cos^2\chi \sin^2\Delta\chi C\phi S\phi - C\psi S\psi \cos^2\Delta\psi C\chi S\Delta\chi \cos^2\phi)$$

$$+ 2\varepsilon_{23}\,(\ \sin^2\psi C\Delta\psi S\Delta\psi S\chi S\Delta\chi S\phi + \sin^2\psi \sin^2\Delta\psi \sin^2\chi S\Delta\chi C\Delta\chi C\phi$$

$$+ \sin^2\psi \sin^2\Delta\psi S\chi C\chi \sin^2\Delta\chi C\phi - \cos^2\psi C\Delta\psi S\Delta\psi S\chi S\Delta\chi S\phi$$

$$+ \cos^2\psi \cos^2\Delta\psi \sin^2\chi S\Delta\chi C\Delta\chi C\phi + \cos^2\psi \cos^2\Delta\psi C\chi S\chi \sin^2\Delta\chi C\phi$$

$$- \sin^2\psi C\Delta\psi S\Delta\psi C\chi C\Delta\chi S\phi - \sin^2\psi \sin^2\Delta\psi C\chi S\chi \cos^2\Delta\chi C\phi$$

$$- \sin^2\psi \sin^2\Delta\psi \cos^2\chi C\Delta\chi S\Delta\chi C\phi + \cos^2\psi S\Delta\psi C\Delta\psi C\chi C\Delta\chi S\phi$$

$$- \cos^2\psi \cos^2\Delta\psi C\chi S\chi \cos^2\Delta\chi C\phi - \cos^2\psi \cos^2\Delta\psi \cos^2\chi C\Delta\chi S\Delta\chi C\phi$$

$$+ S\psi C\psi \sin^2\Delta\psi S\chi S\Delta\chi S\phi - 2\,S\psi C\psi S\Delta\psi C\Delta\psi \sin^2\chi S\Delta\chi C\Delta\chi C\phi$$

$$- 2\,S\psi C\psi S\Delta\psi C\Delta\psi C\chi S\chi \sin^2\Delta\chi C\phi - C\psi S\psi \cos^2\Delta\psi S\chi S\Delta\chi S\phi$$

$$- S\psi C\psi \sin^2\Delta\psi C\chi S\Delta\chi S\phi + 2\,S\psi S\psi S\Delta\psi C\Delta\psi S\chi C\chi \cos^2\Delta\chi C\phi$$

$$+ 2\,S\psi C\psi S\Delta\psi C\Delta\psi \cos^2\chi C\Delta\chi S\delta\chi C\phi + C\psi S\psi \cos^2\Delta\psi C\chi C\Delta\chi S\phi)$$

$$+ 2\varepsilon_{13}\,(\ \sin^2\psi S\Delta\psi C\Delta\psi S\chi S\Delta\chi C\phi - \sin^2\psi \sin^2\Delta\psi \sin^2\chi S\Delta\chi C\Delta\chi S\phi$$

$$- \sin^2\psi \sin^2\Delta\psi S\chi S\chi \sin^2\Delta\chi S\phi - \cos^2\psi C\Delta\psi S\Delta\psi S\chi S\Delta\chi C\phi$$

$$- \cos^2\psi \cos^2\Delta\psi \sin^2\chi S\Delta\chi C\Delta\chi S\phi - \cos^2\psi \cos^2\Delta\psi S\chi C\chi \sin^2\Delta\chi S\phi$$

$$- \sin^2\psi S\Delta\psi C\Delta\psi C\chi C\Delta\chi C\phi + \sin^2\psi \sin^2\Delta\psi C\chi S\chi \cos^2\Delta\chi S\phi$$

$$+ \sin^2\psi \sin^2\Delta\psi \cos^2\chi C\Delta\chi S\Delta\chi S\phi + \cos^2\psi C\Delta\psi S\Delta\psi C\chi C\Delta\chi C\phi$$

$$+ \cos^2\psi \cos^2\Delta\psi C\chi S\chi \cos^2\Delta\chi S\phi + \cos^2\psi \cos^2\Delta\psi \cos^2\chi C\Delta\chi S\Delta\chi S\phi$$

$$+ S\psi C\psi \sin^2\Delta\psi S\chi S\Delta\chi C\phi + 2\,S\psi C\psi S\Delta\psi C\Delta\psi \sin^2\chi S\Delta\chi C\Delta\chi S\phi$$

$$+ 2\,S\psi C\psi C\Delta\psi S\Delta\psi S\chi C\chi \sin^2\Delta\chi S\phi - C\psi S\psi \cos^2\Delta\psi S\chi S\Delta\chi C\phi$$

$$-S\psi C\psi \sin^2\Delta\psi C\chi C\Delta\chi C\phi - 2\,S\psi C\psi S\Delta\psi C\Delta\psi C\chi S\chi \cos^2\Delta\chi S\phi$$

$$- 2\,S\psi C\psi S\Delta\psi C\Delta\psi \cos^2\chi C\Delta\chi S\Delta\chi S\phi + C\psi S\psi \cos^2\Delta\psi C\chi C\Delta\chi C\phi)\,. \qquad (17)$$

To verify that Equation (17) is indeed correct, we note that, if $\Delta\psi = \chi = \Delta\chi = 0$, the following equation is obtained,

$$\varepsilon_{33,\psi} = (\cos^2\phi\ \varepsilon_{11} + \sin 2\phi\ \varepsilon_{12} + \sin^2\phi\ \varepsilon_{22} - \varepsilon_{33})\ \sin^2\psi + (\cos\phi\ \varepsilon_{13} + \sin\phi\ \varepsilon_{23})\sin 2\psi + \varepsilon_{33}$$

which is equivalent to Equation (22) in Dölle's paper [1979] or to Equation (5.4) in Noyan and Cohen [1987].

3. *Derivation of the Stress Equations*

Hooke's law is defined for an isotropic elastic material as [Frederick & Chang, 1972]:

$$\varepsilon_{ij} = \frac{1+\nu}{E}\sigma_{ij} - \frac{\nu}{E}\sigma_{kk}\delta_{ij} \tag{18}$$

where σ_{ij} are the components of the stress tensor, ν is the Poisson's ratio, E is Young's modulus, $\sigma_{kk} \equiv \sigma_{11} + \sigma_{22} + \sigma_{33}$, and δ_{ij} is the Kronecker delta function.

The strain-deformation relationship is defined by

$$\varepsilon_{33,\psi\,\Delta\psi\,\chi\,\Delta\chi\,\phi} = \frac{d_{\psi\,\Delta\psi\,\chi\,\Delta\chi\,\phi} - d_0}{d_0} \tag{19}$$

where $d_{\psi\,\Delta\psi\,\chi\,\Delta\chi\,\phi}$ is the lattice spacing of an (hkl) plane represented in the x^{ν} coordinate system, and d_0 is the lattice spacing of the stress-free material. These planes are perpendicular to x_3^{ν} in our notation. Of course, it is $d_{\psi\,\Delta\psi\,\chi\,\Delta\chi\,\phi}$ which is measured by means of x-ray diffraction using Bragg's law. Finally, for clarity, we shall adopt a three subscript notation, $d_{\psi,\chi,\phi}$, in which the $\Delta\psi$ and $\Delta\chi$ subscript are dropped. However, the explicit dependencies on $\Delta\psi$ and $\Delta\chi$ will be shown. The reader should note that in this notation, the order of the subscripts is not the same as the order of rotations of the coordinate systems. The notation adopted here has been chosen because it is closest to that commonly used in the literature with which we wish to compare our results.

Substitution of Equations (18) and (19) into the right hand side of Equation (17) produces, after much algebra,

$$\frac{d_{\psi,\chi,\phi} - d_0}{d_0} = \frac{1+\nu}{E}\sin^2\psi\,\{\sigma_{11}(\cos^2\Delta\psi\cos^2\phi + \sin^2\Delta\psi\sin^2\chi\cos^2\Delta\chi\sin^2\phi$$

$$+ \sin^2\Delta\psi\cos^2\chi\sin^2\Delta\chi\sin^2\phi - 2\,C\Delta\psi\,S\Delta\psi\,S\chi\,C\Delta\chi\,S\phi\,C\phi$$

$$- 2\,C\Delta\psi\,S\Delta\psi\,C\chi\,S\Delta\chi\,S\phi\,C\phi + 2\sin^2\Delta\psi\,S\chi\,C\chi\,C\Delta\chi\,S\Delta\chi\sin^2\phi$$

$$- \sin^2\Delta\psi\cos^2\phi - \cos^2\Delta\psi\sin^2\chi\cos^2\Delta\chi\sin^2\phi$$

$$- \cos^2\Delta\psi\cos^2\chi\sin^2\Delta\chi\sin^2\phi - 2\,S\Delta\psi\,C\Delta\psi\,S\chi\,C\Delta\chi C\phi\,S\phi$$

$$- 2\,S\Delta\psi\,C\Delta\psi\,C\chi\,S\Delta\chi C\phi\,S\phi - 2\cos^2\Delta\psi S\chi C\chi C\Delta\chi S\Delta\chi\sin^2\phi)$$

$$+ \sigma_{22}(\cos^2\Delta\psi\sin^2\phi + \sin^2\Delta\psi\sin^2\chi\cos^2\Delta\chi\cos^2\phi$$

$$+ \sin^2\Delta\psi\cos^2\chi\sin^2\Delta\chi\cos^2\phi + 2C\Delta\psi S\Delta\psi\,S\chi C\Delta\chi\,S\phi\,C\phi$$

$$+ 2C\Delta\psi S\Delta\psi C\chi S\Delta\chi S\phi\,C\phi + 2\sin^2\Delta\psi\,S\chi\,C\chi C\Delta\chi S\Delta\chi\cos^2\phi$$

$$- \sin^2\Delta\psi\sin^2\phi - \cos^2\Delta\psi\sin^2\chi\cos^2\Delta\chi\cos^2\phi$$

$$- \cos^2\Delta\psi\cos^2\chi\sin^2\Delta\chi\cos^2\phi + 2\,S\Delta\psi\,C\Delta\psi\,S\chi\,C\Delta\chi S\phi C\phi$$

$$+ 2\,S\Delta\psi\,C\Delta\psi\,C\chi\,S\Delta\chi S\phi C\phi - 2\cos^2\Delta\psi S\chi C\chi C\Delta\chi S\Delta\chi\cos^2\phi)$$

$$+ \sigma_{33}(\sin^2\Delta\psi\sin^2\chi\sin^2\Delta\chi + \sin^2\Delta\psi\cos^2\chi\cos^2\Delta\chi$$

$$- 2\sin^2\Delta\psi\,S\chi\,C\chi S\Delta\chi C\Delta\chi - \cos^2\Delta\psi\sin^2\chi\sin^2\Delta\chi$$

$$- \cos^2\Delta\psi\cos^2\Delta\psi\cos^2\chi\cos^2\Delta\chi + 2\cos^2\Delta\psi S\chi C\chi S\Delta\chi C\Delta\chi)$$

$$+ 2\sigma_{12}(\cos^2\Delta\psi\,S\phi\,C\phi - C\Delta\psi S\Delta\psi\,S\chi C\Delta\chi\sin^2\phi$$

$$- C\Delta\psi S\Delta\psi C\chi S\Delta\chi\sin^2\phi + S\Delta\psi C\Delta\psi S\chi C\Delta\chi\cos^2\phi$$

$$- \sin^2\Delta\psi\sin^2\chi\cos^2\Delta\chi C\phi\,S\phi - 2\sin^2\Delta\psi S\chi C\chi C\Delta\chi S\Delta\chi C\phi\,S\phi$$

$$+ S\Delta\psi C\Delta\psi C\chi S\Delta\chi \cos^2\phi - \sin^2\Delta\psi \cos^2\chi \sin^2\Delta\chi C\phi S\phi$$

$$- \sin^2\Delta\psi S\phi C\phi - S\Delta\psi C\Delta\psi S\chi C\Delta\chi \sin^2\phi$$

$$- S\Delta\psi C\Delta\psi C\chi S\Delta\chi \sin^2\phi + \cos^2\Delta\psi \sin^2\chi \cos^2\Delta\chi C\phi S\phi$$

$$+ C\Delta\psi S\Delta\psi S\chi C\Delta\chi \cos^2\phi + 2\cos^2\Delta\psi S\chi C\chi C\Delta\chi S\Delta\chi C\phi S\phi$$

$$+ C\Delta\psi S\Delta\psi C\chi S\Delta\chi \cos^2\phi + \cos^2\Delta\psi \cos^2\chi \sin^2\Delta\chi C\phi S\phi)$$

$$+ 2\sigma_{23} (C\Delta\psi S\Delta\psi S\chi S\Delta\chi S\phi + \sin^2\Delta\psi \sin^2\chi S\Delta\chi C\Delta\chi C\phi$$

$$+ \sin^2\Delta\psi S\chi C\chi \sin^2\Delta\chi C\phi - C\Delta\psi S\Delta\psi C\chi C\Delta\chi S\phi$$

$$- \sin^2\Delta\psi C\chi S\chi \cos^2\Delta\chi C\phi - \sin^2\Delta\psi \cos^2\chi C\Delta\chi S\Delta\chi C\phi$$

$$+ C\Delta\psi S\Delta\psi S\chi S\Delta\chi S\phi - \cos^2\Delta\psi \sin^2\chi S\Delta\chi C\Delta\chi C\phi$$

$$- \cos^2\Delta\psi C\chi S\chi \sin^2\Delta\chi C\phi - S\Delta\psi C\Delta\psi C\chi C\Delta\chi S\phi$$

$$+ 2\cos^2\Delta\psi C\chi S\chi \cos^2\Delta\chi C\phi + \cos^2\Delta\psi \cos^2\chi C\Delta\chi S\Delta\chi C\phi)$$

$$+ 2\sigma_{13}(S\Delta\psi C\Delta\psi S\chi S\Delta\chi C\phi - \sin^2\Delta\psi \sin^2\chi S\Delta\chi C\Delta\chi S\phi$$

$$- \sin^2\Delta\psi S\chi S\chi \sin^2\Delta\chi S\phi - S\Delta\psi C\Delta\psi C\chi C\Delta\chi C\phi$$

$$+ \sin^2\Delta\psi C\chi S\chi \cos^2\Delta\chi S\phi + \sin^2\Delta\psi \cos^2\chi C\Delta\chi S\Delta\chi S\phi$$

$$+ C\Delta\psi S\Delta\psi S\chi S\Delta\chi C\phi + \cos^2\Delta\psi \sin^2\chi S\Delta\chi C\Delta\chi S\phi$$

$$+ \cos^2\Delta\psi S\chi C\chi \sin^2\Delta\chi S\phi - C\Delta\psi S\Delta\psi C\chi C\Delta\chi C\phi$$

$$- \cos^2\Delta\psi C\chi S\chi \cos^2\Delta\chi S\phi - \cos^2\Delta\psi \cos^2\chi C\Delta\chi S\Delta\chi S\phi)\}$$

$$+ \frac{1+\nu}{E} \sin 2\psi \{\sigma_{11}(C\Delta\psi\ S\Delta\psi \cos^2\phi + \cos^2\Delta\psi\ S\chi\ C\Delta\chi\ C\phi\ S\phi$$

$$+ \cos^2\Delta\psi\ C\chi\ S\Delta\chi\ C\phi\ S\phi - \sin^2\Delta\psi\ S\chi\ C\Delta\chi\ C\phi\ S\phi$$

$$- \sin^2\Delta\psi\ C\chi\ S\Delta\chi\ C\phi\ S\phi - S\Delta\psi\ C\Delta\psi \sin^2\chi \cos^2\Delta\chi \sin^2\phi$$

$$- 2\ C\Delta\psi\ S\Delta\psi\ S\chi\ C\chi\ C\Delta\chi\ S\Delta\chi \sin^2\phi - S\Delta\psi\ C\Delta\psi\ \cos^2\chi \sin^2\Delta\chi \sin^2\phi)$$

$$
\begin{aligned}
&+ \sigma_{22}(C\Delta\psi S\Delta\psi \sin^2\phi - \cos^2\Delta\psi\ C\Delta\psi S\chi C\Delta\chi\ S\phi\ C\phi \\
&\quad - \cos^2\Delta\psi\ C\chi\ S\Delta\chi\ S\phi C\phi + \sin^2\Delta\psi S\chi C\Delta\chi\ S\phi\ C\phi \\
&\quad + \sin^2\Delta\psi C\chi S\Delta\chi\ S\phi\ C\phi - S\Delta\psi C\Delta\psi \sin^2\chi \cos^2\Delta\chi \cos^2\phi \\
&\quad - 2\ S\Delta\psi C\Delta\psi\ S\chi\ C\chi C\Delta\chi S\Delta\chi \cos^2\phi - S\Delta\psi C\Delta\psi \cos^2\chi \sin^2\Delta\chi \cos^2\phi) \\
&+ \sigma_{33}(- S\Delta\psi C\Delta\psi \sin^2\chi \sin^2\Delta\chi + 2\ S\Delta\psi C\Delta\psi S\chi C\chi\ S\Delta\chi C\Delta\chi \\
&\quad - S\Delta\psi C\Delta\psi \cos^2\chi \cos^2\Delta\chi) \\
&+ \sigma_{12}(2\ C\Delta\psi S\Delta\psi S\phi C\phi + \cos^2\Delta\psi S\chi C\Delta\chi \sin^2\phi \\
&\quad + \cos^2\Delta\psi C\chi S\Delta\chi \sin^2\phi - \sin^2\Delta\psi S\chi C\Delta\chi \sin^2\phi \\
&\quad - \sin^2\Delta\psi C\chi S\Delta\chi \sin^2\phi + \sin^2\Delta\psi S\chi C\Delta\chi \cos^2\phi \\
&\quad + S\Delta\psi C\Delta\psi \sin^2\chi \cos^2\Delta\chi C\phi S\phi + 4\ S\Delta\psi C\Delta\psi S\chi C\chi C\Delta\chi S\Delta\chi C\phi S\phi \\
&\quad - \cos^2\Delta\psi S\chi C\Delta\chi \cos^2\phi + C\Delta\psi S\Delta\psi \sin^2\chi \cos^2\Delta\chi C\phi S\phi \\
&\quad + \sin^2\Delta\psi C\chi S\Delta\chi \cos^2\phi \\
&\quad + 2\ S\Delta\psi C\Delta\psi \cos^2\chi \sin^2\Delta\chi C\phi S\phi - \cos^2\Delta\psi C\chi S\Delta\chi \cos^2\phi) \\
&+ \sigma_{23}(\sin^2\Delta\psi S\chi S\Delta\chi S\phi - 2\ S\Delta\psi C\Delta\psi \sin^2\chi S\Delta\chi C\Delta\chi C\phi \\
&\quad - 2\ S\Delta\psi C\Delta\psi C\chi S\chi \sin^2\Delta\chi C\phi - \cos^2\Delta\psi S\chi S\Delta\chi S\phi \\
&\quad - \sin^2\Delta\psi C\chi S\Delta\chi S\phi + 2\ S\Delta\psi C\Delta\psi S\chi C\chi \cos^2\Delta\chi C\phi \\
&\quad + 2\ S\Delta\psi C\Delta\psi \cos^2\chi C\Delta\chi S\Delta\chi C\phi + \cos^2\Delta\psi C\chi C\Delta\chi S\phi) \\
&+ \sigma_{13}(\sin^2\Delta\psi S\chi S\Delta\chi C\phi + 2\ S\Delta\psi C\Delta\psi \sin^2\chi S\Delta\chi C\Delta\chi S\phi \\
&\quad + 2\ C\Delta\psi S\Delta\psi S\chi C\chi \sin^2\Delta\chi S\phi - \cos^2\Delta\psi S\chi S\Delta\chi C\phi \\
&\quad - \sin^2\Delta\psi C\chi C\Delta\chi C\phi - 2\ S\Delta\psi C\Delta\psi C\chi S\chi \cos^2\Delta\chi S\phi \\
&\quad - 2\ S\Delta\psi C\Delta\psi \cos^2\chi C\Delta\chi S\Delta\chi S\phi + \cos^2\Delta\psi C\chi C\Delta\chi C\phi)\}
\end{aligned}
$$

$$+\frac{1+\nu}{E}\{\sin^2\chi[\sigma_{11}(\cos^2\Delta\psi\cos^2\Delta\chi\sin^2\phi-\cos^2\Delta\psi\sin^2\Delta\chi\sin^2\phi)$$

$$+\sigma_{22}(\cos^2\Delta\psi\cos^2\Delta\chi\cos^2\phi-\cos^2\Delta\psi\sin^2\Delta\chi\cos^2\phi)$$

$$+\sigma_{33}(\cos^2\Delta\psi\sin^2\Delta\chi-\cos^2\Delta\psi\cos^2\Delta\psi\cos^2\Delta\chi)$$

$$+2\sigma_{12}(-\cos^2\Delta\psi\cos^2\Delta\chi C\phi S\phi+\cos^2\Delta\psi\sin^2\Delta\chi C\phi S\phi)$$

$$+4\sigma_{23}\cos^2\Delta\psi C\Delta\chi S\Delta\chi C\phi-4\sigma_{13}\cos^2\Delta\psi S\Delta\chi C\Delta\chi S\phi]$$

$$+\sin 2\chi[2\sigma_{11}\cos^2\Delta\psi S\chi C\chi C\Delta\chi S\Delta\chi\sin^2\phi+2\sigma_{22}\cos^2\Delta\psi S\chi C\chi C\Delta\chi S\Delta\chi\cos^2\phi$$

$$-2\sigma_{33}\cos^2\Delta\psi S\chi C\chi S\Delta\chi C\Delta\chi$$

$$+\sigma_{12}(-\cos^2\Delta\psi S\chi C\chi C\Delta\chi S\Delta\chi C\phi S\phi-\cos^2\Delta\psi C\chi S\chi S\Delta\chi C\Delta\chi C\phi S\phi)$$

$$+\sigma_{23}(\cos^2\Delta\psi C\chi S\chi\sin^2\Delta\chi C\phi-\cos^2\Delta\psi C\chi S\chi\cos^2\Delta\chi C\phi)$$

$$+\sigma_{13}(-\cos^2\Delta\psi S\chi C\chi\sin^2\Delta\chi S\phi+\cos^2\Delta\psi C\chi S\chi\cos^2\Delta\chi S\phi)]$$

$$+[\sigma_{11}(2S\Delta\psi C\Delta\psi S\chi C\Delta\chi C\phi S\phi+2S\Delta\psi C\Delta\psi C\chi S\Delta\chi C\phi S\phi)$$

$$+\sigma_{22}(-2\Delta\psi C\Delta\psi S\chi C\Delta\chi S\phi C\phi-2\Delta\psi C\Delta\psi C\chi S\Delta\chi S\phi C\phi)$$

$$+2\sigma_{12}(S\Delta\psi C\Delta\psi S\chi C\Delta\chi\sin^2\phi+S\Delta\psi C\Delta\psi C\chi S\Delta\chi\sin^2\phi$$

$$-C\Delta\psi S\Delta\psi S\chi C\Delta\chi\cos^2\phi-C\Delta\psi S\Delta\psi C\chi S\Delta\chi\cos^2\phi)$$

$$+2\sigma_{23}(-C\Delta\psi S\Delta\psi S\chi S\Delta\chi S\phi+S\Delta\psi C\Delta\psi C\chi C\Delta\chi S\phi)$$

$$+2\sigma_{13}(-C\Delta\psi S\Delta\psi S\chi S\Delta\chi C\phi+C\Delta\psi S\Delta\psi C\chi C\Delta\chi C\phi)$$

$$+\sigma_{11}(\sin^2\Delta\psi\cos^2\phi+\cos^2\Delta\psi\sin^2\Delta\chi\sin^2\phi)$$

$$+\sigma_{22}(\sin^2\Delta\psi\sin^2\phi+\cos^2\Delta\psi\sin^2\Delta\chi\cos^2\phi)+\sigma_{33}\cos^2\Delta\psi\cos^2\Delta\chi$$

$$+\sigma_{12}(\sin^2\Delta\psi S\phi C\phi+\cos^2\Delta\psi\sin^2\Delta\chi C\phi S\phi)+\sigma_{23}\cos^2\Delta\psi C\Delta\chi S\Delta\chi C\phi$$

$$-\sigma_{13}\cos^2\Delta\psi C\Delta\chi S\Delta\chi S\phi]-\frac{\nu}{1+\nu}\sigma_{kk}\} \tag{20}$$

Equation (20) is the generalized equation for x-ray stress determination with a diffractometer which is rotated through ψ, $\Delta\psi$, χ, $\Delta\chi$, and ϕ with respect to the sample coordinate system.

Although it is an incomplete proof of the correctness of Equation (20), we note that if $\chi = 0$ and $\sigma_{13} = \sigma_{23} = 0$ Equation (20) becomes

$$\frac{d_{\psi,0,\phi} - d_0}{d_0} = \frac{1+\nu}{E}\{\sigma_{11}\cos^2\phi + \sin 2\phi\sigma_{12} + \sigma_{22}\sin^2\phi - \sigma_{33}\}x$$

$$\{(\cos^2\Delta\psi - \sin^2\Delta\psi)\sin^2\psi + \frac{1}{2}\sin 2\Delta\psi \sin 2\psi + \sin^2\Delta\psi\}$$

$$+\frac{1+\nu}{E}\sigma_{33} - \frac{\nu}{E}\sigma_{kk} \quad . \tag{21}$$

Equation (21) is identical to Equation (6.101) presented in Noyan and Cohen (1987).

The key observation which may be made concerning Equation (20) is that it is of the form

$$\frac{d_{\psi,\chi,\phi} - d_0}{d_0} = (\frac{1+\nu}{E})A\sin^2\psi + (\frac{1+\nu}{E})B\sin 2\psi + C \tag{22}$$

where A, B, and C are terms involving the various components of the stress tensor and trigonometric functions of the various angles relating the sample and diffractometer coordinate systems. The coefficients A, B, and C may be obtained from Equation (20) in the most general case, or from the more specialized cases to be discussed in the next section. As will be seen, these coefficents can be simplified even further under other special conditions and/or geometries. Thus, regardless of the misalignments of the diffractometer with respect to the sample, a two parameter multiple regression of d_{obs} versus $\sin^2\psi$ and $\sin 2\psi$ is the correct procedure for analyzing the data. However, the misalignments $\Delta\chi$, $\Delta\psi$ introduce corrections to the interpretation of the coefficients A and B which, unless accounted for, will lead to errors in the evaluation of the components of the stress tensor. These errors are discussed in detail in the next section.

We note that regardless of the values of χ, $\Delta\chi$, ϕ, and $\Delta\psi$, for $\psi = 0$

$$\frac{d_{0,\chi,\phi} - d_0}{d_0} = C.$$

Thus, by subtracting this term from Equation (20) we can express the general result in the form

$$\frac{d_{\psi,\chi,\phi} - d_{0,\chi,\psi}}{d_0} = (\frac{1+\nu}{E})A\sin^2\psi + (\frac{1+\nu}{E})B\sin 2\psi \tag{23}$$

Equation (23) is a rigorous result. Because $d_{0,\chi,\phi}$ does not deviate from d_o by more than one percent, in practice the d_o in the denominator of the left hand side of Equation (23) can be replaced

by $d_{0,\chi,\phi}$, the $\psi = 0$ intercept of the d versus $\sin^2\psi$ plot. Thus, even in the most general case, and as has long been known from the less general derivations, the need for knowledge of d_o, the stress-free lattice spacing, is eliminated.

SPECIAL CASES

1. *Comparison χ- and ψ-Diffractometers*

The first result which can be obtained from Equation (20) is a direct comparison of the two major diffractometer geometries in current use, the χ and the ψ geometries. Careful examination of the coordinate system transformations in Figure 1 shows that a diffractometer which is tilted through an angle ψ while holding $\phi = 0°$ and $\chi = 0°$ measures the same d-spacings as a diffractometer tilted through χ degrees while holding $\psi = 0°$ and $\phi = 90°$.[2] If we ignore misalignment errors and apply a similar procedure as for the derivation of Equation (23), we find

$$\frac{d_{\psi,0,0} - d_{0,0,0}}{d_o} = \left(\frac{1+\nu}{E}\right)(\sigma_{11} - \sigma_{33})\sin^2\psi + \left(\frac{1+\nu}{E}\right)\sigma_{13}\sin 2\psi \qquad (24a)$$

while

$$\frac{d_{0,\chi,90} - d_{0,0,90}}{d_o} = \left(\frac{1+\nu}{E}\right)(\sigma_{11} - \sigma_{33})\sin^2\chi + \left(\frac{1+\nu}{E}\right)\sigma_{13}\sin 2\chi \quad . \qquad (24b)$$

The symmetry of Equations (24a) and (24b) is to be noted. The particular advantage of Equation (24b), long used in European diffractometer geometries [Macherauch and Wolfstieg, 1977], is that the sample absorption factor, although dependent on ψ, is independent of χ.[3] Thus, χ diffarctometers require no absorption correction. It is also usually possible to make measurements to larger χ tilts than in the equivalent ψ geometry. The general result presented in Equation (20) thus may be used for an equivalent error analysis of the χ-diffractometer. For brevity, we pursue here only the results for the ψ-diffractometer.

---

[2] There is an infinite manifold of such transformations. We illustrate the relations with only one case.

[3] Note that there is a divergence of opinion on angular notation for the various diffractometers as a χ-diffractometer is called a ψ-diffractometer by Macherauch and Wolfsteig (1977) and Wagner et al (1982), while our ψ diffractometer is called an ω-diffractometer by them.

2. ***Deliberate χ-tilt in a ψ-Diffractometer***

Due to complicated geometries of the sample, sometimes the diffractometer must be tilted through large χ angles (Refer to Figure 1). The result for this case, by applying $\Delta\psi = \Delta\chi = 0$ to Equation (20) and similar procedures as for the derivation of Equation (24a), becomes

$$\frac{d_{\psi,\chi,\phi} - d_{0,\chi,\phi}}{d_0} = \frac{1+\nu}{E}\sin^2\psi\,\{(\cos^2\phi - \sin^2\chi\sin^2\phi)\,\sigma_{11} + (\sin^2\phi - \sin^2\chi\cos^2\phi)\,\sigma_{22}$$

$$- \cos^2\chi\,\sigma_{33} + \sin 2\phi(1+\sin^2\chi)\,\sigma_{12}$$

$$+ \sin 2\chi(\cos\phi\,\sigma_{23} - \sin\phi\,\sigma_{13})\}$$

$$+ \frac{1+\nu}{E}\sin 2\psi\{\sin\chi[(\frac{\sin 2\phi}{2}(\sigma_{11} - \sigma_{22}) + (\sin^2\phi - \cos^2\phi)\,\sigma_{12}]$$

$$+ [\cos\chi(\sin\phi\,\sigma_{23} + \cos\phi\,\sigma_{13})]\} \quad . \tag{25}$$

In the typical case where $\phi = 0$, Equation (25) becomes

$$\frac{d_{\psi,\chi,0} - d_{0,\chi,0}}{d_0} = \frac{1+\nu}{E}\sin^2\psi\{\sigma_{11} - \sin^2\chi\sigma_{22} - \cos^2\chi\sigma_{33} + \sin 2\chi\sigma_{23}\}$$

$$+ \frac{1+\nu}{E}\sin 2\psi\{\cos\chi\sigma_{13} - \sin\chi\sigma_{12}\} \quad . \tag{26}$$

Thus it is seen that, depending on the specific values of the components of the tensor, the interpretation of the coefficients of the multiple regression of $d_{\psi,\chi,\phi}$ versus $\sin^2\psi$ and $\sin 2\psi$ as $\sigma_{11} - \sigma_{33}$ and σ_{13} respectively can lead to potentially significant errors. The importance of these corrections explains some of the difficulty one of us (RWH) has had in interpreting data from flat sheets of nickel-plated steel which were tilted through large χ-angles in an attempt to avoid serious preferred orientation problems. Equation (26) should be compared with the classical result show Equation (24a).

It is important to note from Equations (25) and (26) that it is possible to obtain all six elements of the stress tensor by making ψ scans at three different χ tilts at the same rotation angle ϕ. This is to be compared with the more traditional way of making ψ scans at three different ϕ rotations with $\chi = 0$. In many practical examples, the χ-tilt procedure may offer the possibility for such measurements when the ϕ-tilt is precluded by the large and complicated sample geometries or vice versa.

3. ***Errors in the Small-Angle Approximation***

Since the experimental misalignment errors, $\Delta\psi$ and $\Delta\chi$, are small the sine and cosine terms may be expanded in a power series. Then, if only the linear terms are retained, Equation (20) can be reduced to

$$\frac{d_{\psi,\chi,\phi} - d_0}{d_0} = \frac{1+\nu}{E}\sin^2\psi\,\{[\,(\cos^2\phi - \sin^2\chi\sin^2\phi)\,\sigma_{11} + (\sin^2\phi - \sin^2\chi\cos^2\phi)\,\sigma_{22}$$

$$- \cos^2\chi\,\sigma_{33} + \sin 2\phi(1+\sin^2\chi)\,\sigma_{12}$$

$$+ \sin 2\chi(C\phi\,\sigma_{23} - S\phi\,\sigma_{13})] + [\,2\,S\chi(\sin 2\phi(\sigma_{22} - \sigma_{11})$$

$$+ (\cos^2\phi - \sin^2\phi))\,\sigma_{12} - 4C\chi(S\phi\sigma_{23} + C\phi\sigma_{13})]\,\Delta\psi$$

$$+ [\,\sin 2\chi(-\sin^2\phi\,\sigma_{11} - \cos^2\phi\,\sigma_{22} + \sigma_{33} + \sin 2\phi\,\sigma_{12})$$

$$+ 2C\phi\,(-\sin^2\chi + \cos^2\chi)\,\sigma_{23} + 2\,S\phi(\sin^2\chi - \cos^2\chi)\,\sigma_{13}\,]\,\Delta\chi\,\}$$

$$+ \frac{1+\nu}{E}\sin 2\psi\{[\,S\chi\,\frac{\sin 2\phi}{2}(\sigma_{11} - \sigma_{22}) + S\chi(\sin^2\phi - \cos^2\phi)\,\sigma_{12}$$

$$+ C\chi(S\phi\,\sigma_{23} + C\phi\,\sigma_{13})\,] + [\,(\cos^2\phi - \sin^2\chi\sin^2\phi)\,\sigma_{11}$$

$$+ (\sin^2\phi - \sin^2\chi\cos^2\phi)\,\sigma_{22} - \cos^2\chi\,\sigma_{33}$$

$$+ \sin 2\phi(1+\sin^2\chi)\,\sigma_{12} + \sin 2\chi(C\phi\,\sigma_{23} - S\phi\,\sigma_{13})\,]\,\Delta\psi$$

$$+ [\,C\chi\,\frac{\sin 2\phi}{2}(\sigma_{11} - \sigma_{22}) + C\chi(\sin^2\phi - \cos^2\phi)\,\sigma_{12}$$

$$- S\chi(S\phi\,\sigma_{23} + C\phi\,\sigma_{13})\,\Delta\chi\,]\,\}$$

$$+ \frac{1+\nu}{E}\{\sin^2\chi[(\sin^2\phi\sigma_{11} + \cos^2\phi\sigma_{22} - \sigma_{33} - \sin 2\phi\,\sigma_{12})$$

$$+ 4(C\phi\,\sigma_{23} - S\phi\,\sigma_{13})\,\Delta\chi\,] + \sin 2\chi[(-C\phi\,\sigma_{23} + S\phi\,\sigma_{13})$$

$$+ (\sin^2\phi\,\sigma_{11} + \cos^2\phi\,\sigma_{22} - \sigma_{33} - \sin 2\phi\,\sigma_{12})]\,\Delta\chi\,\}$$

$$+ [S\chi \sin 2\phi(\sigma_{11} - \sigma_{22}) - 2\, S\chi \cos^2\phi\, \sigma_{12}$$

$$+ 2\, C\chi(S\phi\sigma_{23} + C\phi\, \sigma_{13})\, \Delta\psi + (-C\phi\, \sigma_{23} + S\phi\, \sigma_{13})\, \Delta\chi\,]$$

$$+ \sigma_{33} - \frac{\nu}{1+\nu}\sigma_{kk}\} \qquad (27)$$

If $\chi = 0$ (no deliberate tilt of specimen and /or instrument), Equation (27) becomes

$$\frac{d_{\psi,0,\phi} - d_0}{d_0} = \frac{1+\nu}{E}\ \sin^2\psi\{[\ \cos^2\phi\sigma_{11} + \sin^2\phi\sigma_{22} - \sigma_{33} + \sin 2\phi\sigma_{12}]$$

$$- 4\,[S\phi\ \sigma_{23} + C\phi\ \sigma_{13}\,]\,\Delta\psi + 2\,[C\phi\ \sigma_{23} - S\phi\ \sigma_{13}]\,\Delta\chi\,\}$$

$$+ \frac{1+\nu}{E}\sin 2\psi\{[S\phi\ \sigma_{23} + C\phi\ \sigma_{13}\,] + [\ \cos^2\phi\ \sigma_{11} + \sin^2\phi\sigma_{22} - \sigma_{33} + \sin 2\phi\ \sigma_{12}\,]\,\Delta\psi$$

$$+ [\ \frac{\sin 2\phi}{2}(\sigma_{11} - \sigma_{22}) + (\sin^2\phi - \cos^2\phi)\,\sigma_{12}\,]\,\Delta\chi\}$$

$$+ \frac{1+\nu}{E}\{2\,[\,S\phi\ \sigma_{23} + C\phi\ \sigma_{23}\,]\,\Delta\psi + [S\phi\ \sigma_{23} - C\phi\ \sigma_{13}\,]\,\Delta\chi$$

$$+ \sigma_{33} - \frac{\nu}{1+\nu}\sigma_{kk}\} \qquad (28)$$

These results show that the angular error terms $\Delta\chi$ and $\Delta\psi$ introduce errors into the interpretation of both the slope of the d_{obs} versus $\sin^2\psi$ plot and the $\sin^2\psi$ split as well. Since some of these terms involve the product of the misalignment error with one of the normal stresses, these errors may be quite large. They are the subject of the last section of this paper.

4. *Misalignment Errors in a ψ-Diffractometer*

Consider the case of small misalignment errors $\Delta\psi$ and $\Delta\chi$ in a diffractometer where there is no deliberate χ-tilt. If $\phi = 0$ and a similar procedure as for the derivation of of Equation (24a) is applied, Equation (28) becomes

$$\frac{d_{\psi,0,0} - d_{0,0,0}}{d_o} = \frac{1+\nu}{E}\sin^2\psi\ \{[\ \sigma_{11} - \sigma_{33}] - 4\,\sigma_{13}\,\Delta\psi + 2\,\sigma_{23}\,\Delta\chi\,\}$$

$$+\frac{1+\nu}{E}\sin 2\psi\ \{\sigma_{13}+[\sigma_{11}-\sigma_{33}]\,\Delta\psi-\sigma_{12}\,\Delta\chi\}\ . \tag{29}$$

A similar equation is easily derived for $\phi = 90°$. Equation (29) shows that the physical interpretation of the slope and the $\sin^2\psi$ split of the d versus $\sin^2\psi$ plot may be significantly changed as a result of the diffractometer misalignment errors $\Delta\psi$ and $\Delta\chi$. However, the magnitude of such errors depends on the actual values of the components of the stress tensor. In general, it is seen that an error in the zero of the ψ-tilt ($\Delta\psi$) induces a $\sin^2\psi$ split even if the shear stress components are zero. If one is not aware of effects such as these, the $\sin^2\psi$ split could be interpreted as a fictitious shear stress. The magnitude of these effects will be discussed in the next section.

NUMERICAL EXAMPLES

Examination of Equation (29) shows that, unlike the classical results presented heretofore, the coefficient of sin 2ψ (B in Equation (23)) is not zero even in the absence of shear stresses if there is an angular misalignment. Thus, if the diffractometer is inadvertently tilted (χ) or misaligned ($\Delta\psi$,$\Delta\chi$) there may be a $\sin^2\psi$ split which could be misinterpreted as a shear stress. To investigate the magnitude of such errors, we have performed several numerical tests using a stress tensor representative of the stresses found in cast steel railroad wheels. In these examples we have used σ_{11} = -500 Mpa, σ_{22} = -300 Mpa, σ_{12} = 300 Mpa, $\sigma_{33} = \sigma_{13} = \sigma_{23} = 0$, and $\frac{1+\nu}{E} = 5.88x10^{-9}$ Mpa^{-1}.

Figures 2 and 3, generated from Equation (29), show the resultant error for several typical values of $\Delta\chi$ and $\Delta\psi$ misalignments. The effects of $\Delta\chi$ and $\Delta\psi$ are additive (Refer to Equation (29)). Figure 3 shows the effect of each misalignment, $\Delta\chi$ or $\Delta\psi$, separately on the shift of the d-spacings. An important conclusion may be drawn from these data. Since typical d-spacing shifts which result from residual stress are of the order of several hundred ppm, the errors introduced by

the misalignment errors are significant. For example, in plane stress the d-spacing at $\psi = 45°$ shifts by -0.00041Å from the true d-spacing.

To further investigate these effects, an equation of the form of Equation (24) was regressed against the data of Figure 2 and 3 to determine the values of the ficticious shear stresses. Table 1 shows the values of both the individual and the combined effects of $\Delta\chi$ and $\Delta\psi$ misalignments on the ficticious shear and normal stresses under the assumed conditions. In this example, the fiticious shear stress is shown to increase considerably with the misalignments. Comparison of Figures 3 (A) and (B) shows that the $\Delta\psi$ error is larger than the $\Delta\chi$ error under these specific stress assumptions. However, it should be noted that the magnitude of the fictitious stresses depends on not only magnitude of misalignment errors but also magnitude of the corresponding normal and shear stresses.

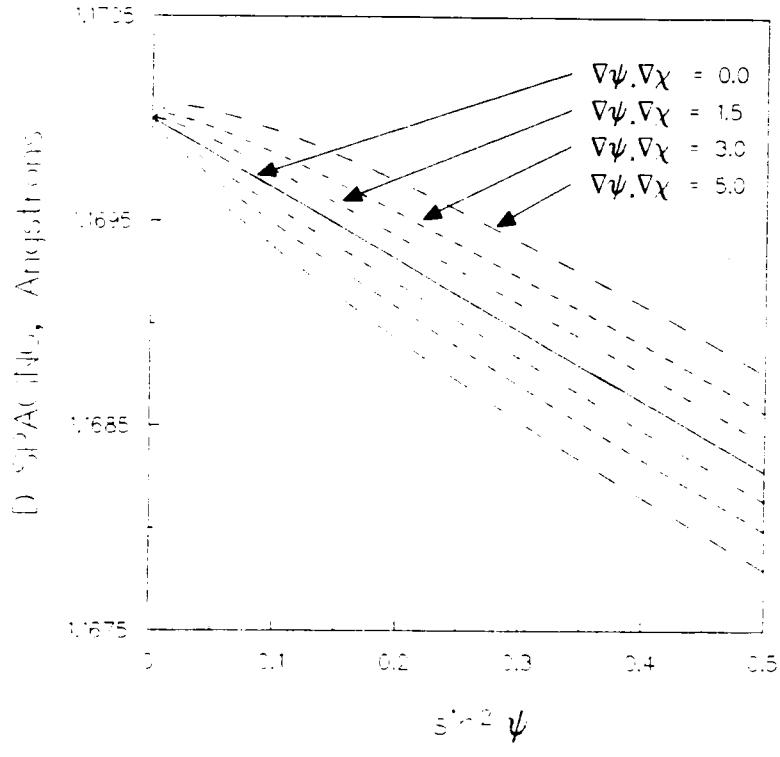

Figure 2. The combined effect of $\Delta\psi$ and $\Delta\chi$ misalignments on the d-spacing versus $\sin^2\psi$ plots for a material in plane stress with σ_{11} = -500 Mpa, σ_{22} = -300 Mpa, and σ_{12} = 300 Mpa .

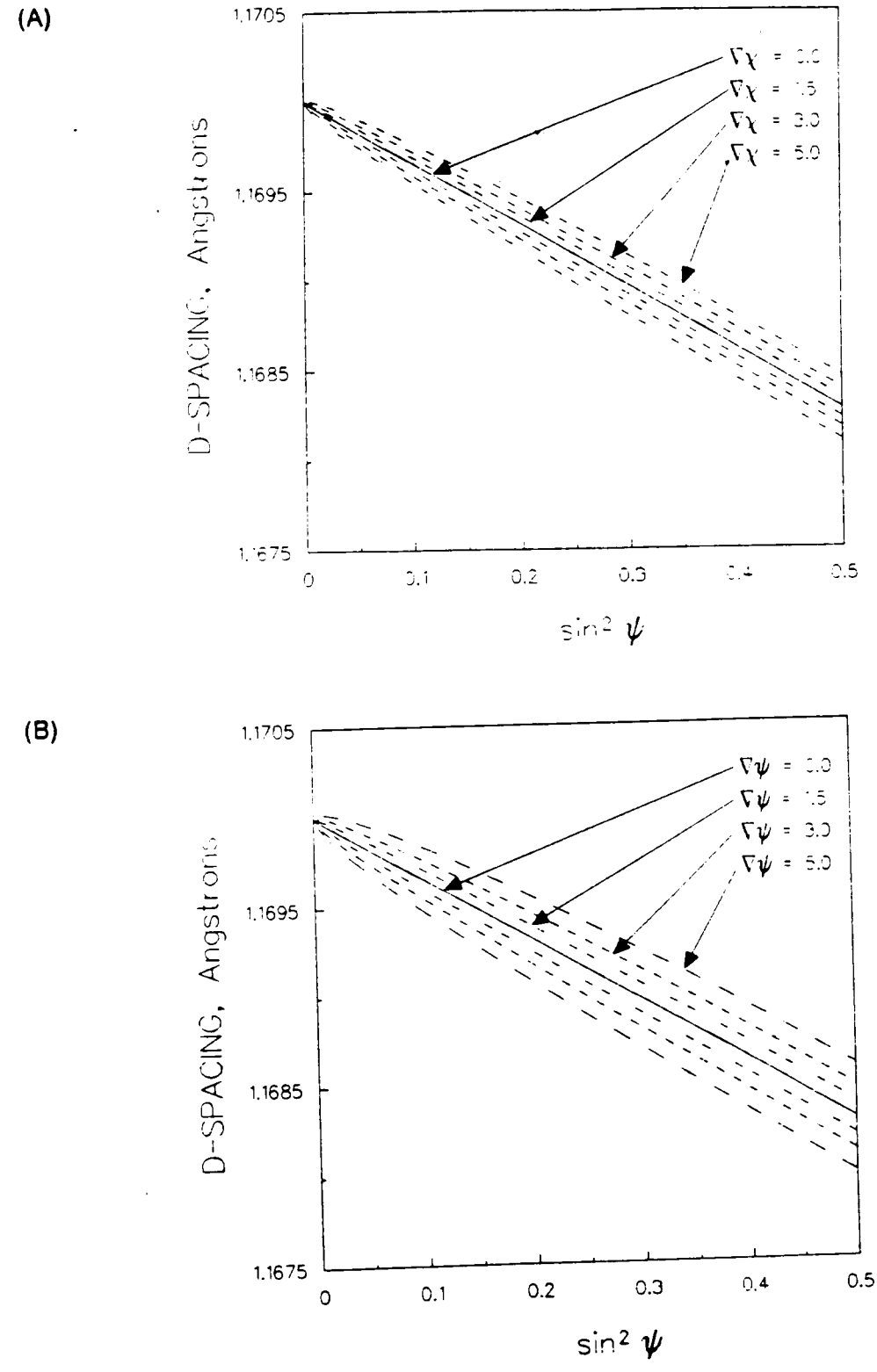

Figure 3. (A) The effect of $\Delta\chi$ misalignment and (B) The effect of $\Delta\psi$ misalignment on the d-spacing versus $\sin^2\psi$ plots for a material in plane stress with σ_{11} = -500 Mpa, σ_{22} = -300 Mpa, and σ_{12} = 300 Mpa .

If σ_{13} and σ_{23} exist, $\Delta\chi$ and $\Delta\psi$ misalignments also affect the determination of the normal stresses (Refer to Equation (24)). However, the effects are small, or even sometimes negligible, because of the multiplication of normally small shear stress and small misalignment angles.

Table 1

"Fictitious Shear Stresses" introduced by misalignments

$\sigma_{11} = -500;$ $\sigma_{22} = -300;$ $\sigma_{12} = 300;$ $\sigma_{33} = \sigma_{13} = \sigma_{23} = 0$ *(Mpa)*			
Error(deg)	$-\sigma_{12}\Delta\chi$(MPa)	$\sigma_{11}\Delta\psi$(MPa)	Total(MPa)
0	0.0	0.0	0.0
1	-8.7	-5.2	-13.9
2	-17.5	-10.5	-28.0
3	-26.2	-15.7	-41.9
4	-34.9	-20.9	-55.8
5	-43.6	-26.2	-69.8

DISCUSSION

The results of our derivation and of our numerical calcuations for a specific example clearly show that inadvertent $\Delta\chi$ and $\Delta\psi$ misalignments of a x-ray residual stress diffractometer can have a significant effect on the interpretation of the residual stresses in a sample. However, although the final results are complex, it is shown that the general form of the d_{obs} versus $\sin^2\psi$ plot is unchanged from the traditional result; only the numerical values of the coefficients change. If a deliberate sample tilt (χ) is required because of the sample geometry, it is still possible to recover the entire stress tensor provided that the value of χ is known. In fact, if $\psi = 0$ and only χ is varied, our results reduce to that standard equations for a χ diffractometer.

REFERENCES

Barrel, M., LeBrun, J. L., Sprauel, J. M., and Maeder, G. (1987). ***Met. Trans. A.***, **18A**, 1229-1238.

Dölle, H. and Hauck, V. (1978). ***Z. Metallkde.***, **69**, 410-.

Dölle, H. (1979). ***J. Appl. Cryst.*** **12**, 489-501.

Frederick, D. and Chang, T. S. (1972). ***Continuum Mechanics.*** Cambridge : Scientific Publishers.

Hendricks, R. W. and Jo, J. (1988). ***Proceedings of the Second International Conference on Residual Stress (ICRS-2).*** Nancy, France (Nov. 1988), London : Plenum, In Press.

James, M. R. (1977). ***An Examination of Experimental Techniques in X-Ray Residual Stress Analysis.*** Ph.D. Thesis, Northwestern Univ., Evanston, Illinois.

James, M. R. and Cohen, J. B. (1979). ***J. Appl. Cryst.*** **12**, 339-345.

Jatczak, C. F. and Boehm, H. H. (1973). ***Adv. X-ray Analysis***, **17**, 354-370.

Lode, W. and Peiter, A. (1977). ***Harterei-Tech. Mitt.***, **32**, 235.

Lode, W. and Peiter, A. (1981). ***Metall.***, **35**, 578.

Macherahch, E. and Wolfstieg, U. (1977). ***Adv. X-Ray Analysis***, **20**, 369-377.

Marion, R. H. and Cohen, J. B. (1975). ***Adv. X-Ray Analysis***, **18**, 466-501.

Noyan, I. C., and Cohen, J. B. (1987). ***Residual Stress Measurement by Diffraction and Interpretation.*** New York : Springer - Verlag.

Pardue, E. B. S. and James, M. R. (1988). ***Proceedings of the Second International Conference on Residual Stress (ICRS-2).*** Nancy, France (Nov. 1988), London : Plenum, In Press.

Pardue, E. B. S., Hendricks, R. W. and James, M. R. (1988). ***Adv. X-Ray Analysis***, **31**, 205-212.

Wylie, C. R. and Barrett, L. C. (1982). ***Advanced Engineering Mathematics***, 5th Ed.. New York : McGraw-Hill.

Wagner, C. N. J., Boldrick, M. S., and Perez Mendez, V. (1982). ***Adv. X-Ray Analysis***, **26**, 275-282.

Zantopulos, H. and Jatczak, C. F. (1970). ***Adv. X-ray Analysis***, **14**, 360-376.

12.0 APPENDIX B : RESIDUAL STRESS DATA FOR WHEELS

This chapter consists of four sections, containing x-ray residual stress data, hole drilling strain data, and residual stress data. Sections 12.1.1 and 12.1.2 introduce x-ray residual stress data which are graphically shown in Figures 21-32. Section 12.2.1 shows hole drilling strains, approximate residual stresses (Equation 3-14), more accurate residual stresses (finite element calculation) at the two inches from the front rim corner on the tread of the wrought, normal wear wheel. Sections 12.2.2 and 12.2.3 show hole drilling strains and approximate residual stresses at two inches and three inches, respectively, from the front rim corner on the tread of the heat-discolored (more than four inches) wheel.

12.1 X-RAY RESIDUAL STRESSES

12.1.1 Circumferential Normal Stresses in Six Wheels at Sixteen Location

Location (Figure 16)	Wheel D #1	Wheel D #2	Wheel C #1	Wheel C #2	Wheel A #1	Wheel A #2	Wheel A #3	(ksi) #4
(1)	-55.7	-66.5	-33.6	-19.6				
(2)	-53	-49.7	-30.8	-39.9				
(3)	-22.5	-23.1	-26.2	-55.8	-55.8	-45.0	-60.0	-48.0
(4)	-42.4	-36.9	-19.7	-30.6	-77.2	-97.9	-75.8	-65.3
(5)	-22.1	-32.1	-26.7	-40.9	-55.0	-51.0	-48.9	-48.7
(6)	-48.4	-50.1	-35.0	-28.3	-67.2	-92.6		-75.1
(7)								
(8)	-38.9	-60.7	-72.7	-79.7	-25.2	-25.4	-18.3	-26.0
(9)		-23.4	-26.2	-25.5	-27.5	-44.0	-69.0	-52.0
(10)	-47.1	-42.5	-33.6	-30.7	-14.7	-18.6	-8.7	-9.7
(11)	-51.4	-41.4	-40.3	-49.3	-12.3		1.2	- 8.9
(12)	-35.1	-35.9	-28.4	-18.4			- 8.1	-13.8
(13)	-50.0	-57.0	-22.5	-31.3	-10.9		-17.8	-12.0
(14)	-39.3	-38.1	-20.3	-17.9				
(15)	-51.4	-48.4	-27.0	-46.25				
(16)	-45.0	-45.6	-42.9	-59.0				

Location	Wheel F		Wheel B			Wheel E		(ksi)
(Figure 16)	#1	#2	#1	#2	#3	#4	#1	#2
(1)							- 9.2	-17.6
(2)							+ 1.5	-13.2
(3)	-47.7	-83.9	-24.5	-24.8		- 7.1	-40.6	-54.3
(4)	-101.7	-101.3	-54.8	-46.9		-43.9	-51.6	-95.2
(5)	-98.9	-90.2	-53.0	-57.0	-58.4	-48.0	-61.5	-82.5
(6)	-106	-92.6		28.9	13.2	5.4	29.3	16.7
(7)	-83.3	-80.6	-73.7	-66.5	-80.1	-89.0	-104.9	-145.7
(8)	-59.3	-24.5	29.2	37.5	32.0	20.3	-26.9	-22.5
(9)	-98.3	-54.1	17.6	14.3	11.2	24.4	-32.6	-15.1
(10)	-26.7	-16.3		- 4.6	11.7	- 0.9	- 5.1	10.1
(11)	- 9.4	-19.5	5.4		1.0	5.7	- 8.4	-10.4
(12)	- 0.3	4.6	- 1.5		- 2.0		- 6.4	-2.7
(13)			- 1.8	1.5	- 4.7	-14.6	-11.2	
(14)	- 2.9	2.8	- 6.9				-17.6	-26.4
(15)	-54.9	-20.0	-15.3	- 7.0			-31.0	-38.6
(16)								

12.1.2 Circumferential Shear Stresses in Six Wheels at Sixteen Location

Location	Wheel D		Wheel C			Wheel A		(ksi)
(Figure 16)	#1	#2	#1	#2	#1	#2	#3	#4
(1)	-5.5	-0.6	2.0	0.0				
(2)	-4.2	-7.2	0.0	0.0				
(3)	0.0	0.0	0.0	0.0	-8.7	0.5	-4.4	-4.3
(4)	0.0	0.0	0.0	0.0	3.7	5.1	7.2	6.7
(5)	-1.2	0.0	0.0	.0	2.3	0.3	5.9	8.6
(6)	-1.7	-0.9	-3.3	-2.3	-6.4	-3.5		-3.1
(7)								
(8)	-2.2	-0.6	-2.8	-2.8	-7.9	-6.0	-8.5	-7.5
(9)		2.2	-1.8	0.0	-1.8	-3.2	-4.8	-3.9
(10)	-5.9	-5.6	-4.3	-2.1	-4.9	-4.6	-4.0	-3.2
(11)	-4.4	-5.5	-4.5	-3.6	0.0		-12.7	-9.8
(12)	-2.3	-2.3	-2.2-	-1.5			0.0	0.0
(13)	0.0	0.0	-3.3	3.9	0.0		0.0	0.0
(14)	-3.7	-4.4	-3.9	-2.0				
(15)	-3.0	-3.6	-3.2	-4.4				
(16)	-7.3	-5.6	-5.3	0.0				

Location	Wheel F		Wheel B				Wheel E	
(Figure 16)	#1	#2	#1	#2	#3	#4	#1	#2
(1)							- 0.4	-2.4
(2)							0.0	0.0
(3)	-6.9	-2.7	0.0	-2.9		3.5	3.8	10.2
(4)	-7.4	-1.6	-7.5	-6.2	-8.4	-8.4		2.5
(5)	6.5	9.7	-5.0	-8.7	-6.9	-7.8	-11.8	-5.6
(6)	-5.5	-3.9		0.0	2.6	2.8	2.5	0.0
(7)	0.0	8.0	1.7	0.0	0.3	4.2	-2.5	-4.5
(8)	4.0	4.0	-2.5	-1.3	-1.0	-1.6	-4.5	-3.0
(9)	10.6	2.8	-3.4	0.0	0.0	0.0	0.0	0.0
(10)	2.3	0.0	0.0	-1.0	-8.8	-1.0	0.0	0.0
(11)	-1.1	-3.8	-1.1	0.0	0.0	-2.9	0.0	0.0
(12)	0.0	0.0	-2.6		0.0		-2.0	0.0
(13)			0.0	-0.4	0.2	0.0	1.8	
(14)	-7.4	-1.4	-2.8				0.0	0.0
(15)	-2.8	-2.9	0.0	-3.3			1.4	1.4
(16)								

12.2 HOLE DRILLING RESIDUAL STRESSES

12.2.1 Strains, Approximate and More Accurate Residual Stresses at 2" from Rim Corner on the Tread of the Cast, Normal Wear Wheel

Hole depth (inch)	Strain 1	2	3	Approximate residual stress aixal	hoop	More accurate residul stress (ksi) axial	hoop
0.000 - 0.005	37	40	31				
0.000 - 0.100	85	97	87	-56.8	-57.7	-58.0	-59.0
0.010 - 0.020	166	203	204	-56.7	-65.7	-45.8	-62.8
0.020 - 0.030	214	272	290	-45.6	-59.4	-31.5	-48.6
0.030 - 0.040	235	309	334	-36.9	-49.4	-16.1	-27.0

12.2.2 Strains and Approximate Residual Stresses at 2″ from Rim Corner on the Tread of the Heat-discolored (More Than 4″) Wheel

Hole depth (inch)	Strain 1	2	3	Approximate residual stress (ksi) aixal	hoop
0.000 - 0.005	17	23	21		
0.000 - 0.100	55	66	68	-37.2	-44.7
0.010 - 0.020	151	170	186	-63.0	-70.7
0.020 - 0.030	247	267	293	-72.5	-78.0
0.030 - 0.040	292	311	342	-55.4	-57.1

12.2.3 Strains and Approximate Residual Stresses at 3″ from Rim Corner on the Tread of the Heat-discolored (More Than 4″) Wheel

Hole depth (inch)	Strain 1	2	3	Approximate residual stress (ksi) aixal	hoop
0.000 - 0.005	-22	0.0	33		
0.000 - 0.100	-52	27	113	19.2	-60.0
0.010 - 0.020	-110	106	276	12.0	-77.6
0.020 - 0.030	-161	177	405	13.75	-72.2
0.030 - 0.040	-216	200	458	25.6	-42.2

The vita has been removed from the scanned document